Femtosecond Electron diffraction Studies of Photoinduced Spin Crossover in Single Crystal $[Fe(PM\text{-}AzA)_2](NCS)_2$

Dissertation

Zur Erlangung des Doktorgrades

Fachbereich Chemie

der Universität Hamburg

Vorgelegt von

Yifeng Jiang

Hamburg, 2016

Gutachter der Dissertation: Prof. Dwayne Miller

Prof. Horst Weller

Datum der Disputation: 11.11.2016

Vorsitzender des Prüfungsausschusses: Prof. Dr. Alf Mews

Mitglieder der Prüfungskommission: Prof. Dr. Henning Tidow
Prof. Dr. Dwayne Miller
Prof. Dr. Michael Fröba
PD Dr. Christian Klinke

Datum der Druckfreigabe: 11.11.2016

Abstract

Spin crossover (SCO) is a phenomenon whereby a molecular transition is induced by photoexcitation or a change in temperature and pressure. SCO complexes have been studied for their potential applications in photoswitchable devices and magnetic data storages.

Photoinduced SCO dynamics undergo ultrafast photoswitching of spin states involving both changes in electronic and nuclear structures. The electronic changes associated with SCO have been identified as a two-step intersystem crossing with an extremely fast relaxation of a short-lived intermediate state followed by vibrational cooling of the photoinduced high-spin state by multiple methods, including transient absorption and reflection spectroscopies, X-ray near edge absorption (XANES) and emission spectroscopies, and Raman spectroscopy.

For the structural changes in SCO, the metal-ligand bond (Fe-N bond in $[Fe(PM\text{-}AzA)_2](NCS)_2$) is generally considered as one of the most important consequences of SCO, and it is taken as the primary reaction coordinate along which SCO transition occurs. The metal-ligand bond elongation is reported to be directly correlated in time to the electronic state dynamics observed by changes in the spectral features of the complex, following with the other ligand motions. However, optical spectroscopies are more sensitive to the electronic state changes, while the XANES studies rely on modelling to deduce the metal-ligand bond elongation.

In this thesis, we employ femtosecond electron diffraction (FED), a direct measurement of the nuclear coordinates which has been uniquely calibrated by exploiting the thermal cycling of the high spin and low spin states of spin crossover systems. A photo-triggered streak camera is used to characterize the temporal resolution of our DC-RF hybrid electron source. The time stamping technique is used to correct arrival timing jitter of the electron

pulses. We measure the short-term timing jitter to be 200 fs root-mean-square (RMS) and the pulse duration of a single electron pulse to be 178 fs RMS with an areal density of 0.92 electron per μm^2.

The results of the FED experiment show that the structural changes of the metal and ligand and the electronic state changes in the metal atom are concomitant but not simultaneous. The metal-ligand bond elongation, compared to other nuclear motions in the photoinduced SCO, is not a conclusive signature of the photoinduced SCO, and it is coupled to other nuclear motions in the phase transition. Furthermore, these motions are significantly delayed with respect to the electronic SCO transitions.

Zusammenfassung

Spin-Crossover (SCO) ist ein Phänomen, bei dem ein molekularer Übergang von Photoexcitaion oder eine Änderung der Temperatur und des Drucks induziert wird. SCO-Komplexe wurden wegen ihrer möglichen Anwendungen in photoschaltbaren Vorrichtungen und magnetischen Datenspeichern untersucht.

Photoinduzierte SCO-Dynamiken unterziehen sich ultraschneller Photoschaltung der Spinzustand, in der sowohl elektronische als auch nukleare Veränderungen beinhaltet werden. Die elektronischen Änderungen im Zusammenhang mit SCO wurden als zweistufiges „intersystem crossing“ von mehreren Methoden identifiziert, einschließlich der transienten Absorption-Spektroskopie, Reflexion-Spektroskopie, Röntgen-Nahkanten-Absorptions-Spektroskopie (XANES), Röntgenemissionsspektroskopie und Raman-Spektroskopie. Das zweistufige „intersystem crossing“ ist eine extrem schnelle Entspannung der kurzlebigen Zwischenzustand, gefolgt von schwingender Kühlung des photoinduzierten hohen Spinzustand,

Strukturell wird die Metall-Ligand-Bindung (Fe-N-Bindung in $[Fe(PM\text{-}AzA)_2](NCS)_2$) im Allgemeinen als eine der wichtigsten Folgen der SCO betrachtet. Sie wird als die primäre Reaktionskoordinate in SCO-Dynamiken angenommen. Es wurde berichtet, dass die Dehnung einer Metall-Ligand-Bindung mit der elektronischen Zustandsdynamik zeitlich korreliert ist, was durch Veränderungen der komplexen spektralen Merkmale beobachtet wurde. Allerdings ist optische Spektroskopie empfindlicher auf die elektronischen Zustandsänderungen, während die XANES-Untersuchungen sich auf Modellierung verlassen, um die Dehnung einer Metall-Ligand-Bindung zu spekulieren.

In dieser Arbeit verwenden wir die Elektronenbeugung mit Femtosekunden (FED), eine direkte Messung der Kernkoordinaten, die durch Ausnutzung der thermischen Zyklen der High-Spin- und Low-Spin-Zuständen von SCO-System kalibriert wurde. Eine Streak-Kamera wird verwendet, um die zeitliche Auflösung unserer DC-RF Hybrid-Elektronenquelle zu charakterisieren und das Jitter der Ankunftszeit von Elektronenpulse

zu korrigieren. Wir maßen die kurzfristigen Zeitjitter (200 fs RMS) und die Impulsdauer des Impuls von einzelnen Elektrons (178 fs RMS) mit einer Flächendichte von 0,92 Elektronen pro μm^2.

Die Ergebnisse des FED-Experiments zeigen, dass die Strukturänderungen des Metalls und Ligands und die elektronische Zustandsänderungen in dem Metallatom sind begleitend, aber nicht gleichzeitig. Die Dehnung einer Metall-Ligand-Bindung, im Vergleich zu anderen Kernbewegungen in der photoinduzierten SCO, ist kein ausschlaggebender Faktor des photoinduziertes SCO. Sie wird mit den anderen Kernbewegungen in Phasenübergang kombiniert. Die Dehnung einer Metall-Ligand-Bindung (und andere Kernbewegungen) ist, im Vergleich zu SCO-Dynamiken, signifikant verzögert.

Acknowledgements

First of all, I must thank my research supervisors Prof. R. J. Dwayne Miller and Prof. Horst Weller. Dwayne gave me this opportunity to work in both his groups at the University of Toronto and the University of Hamburg. In the past four years, he gave me a very free and enjoyable research environment, and encouraged me by his enthusiasm and optimism.

I also thank all my colleagues from the Dwayne Miller group. Raymond Gao and Hubert Jean-Ruel built one of the best femtosecond electron diffraction (FED) setups in the world, and they taught me all the details of FED. Therefore, I could use our fantastic FED setups to start my PhD work research directly with their helps. Or I would have to spend many years building FED setup before FED studies. I would like to thank my close friend and teammate Lai Chung Liu. We worked together closely both on FED experiments and further FED data analysis. Moriena Gustavo always tried his best to help me in our lab with his knowledge. Ryan Field played a very important role in our photoinduced spin crossover study. Cheng Lu, Guenther Kassier, and Henrike Mueller-Werkmeister contributed a lot to the work reported in this thesis as well. I also want to thank other colleagues Antoine Sarracini, Kit Fai Feng, Saeed Oghbaey, Kyle Machee, Hazem Daoud, and Olivier Pare-Labrosse. I thank Dongfang Zhang, who helped me a lot in the life and the research when I worked in Germany. I want to thank our collaborators Prof. Eric Collet for giving us important $Fe[(PM\text{-}AzA)_2](NCS)_2$ samples and helping us to understand the spin crossover dynamics from our FED results.

Finally, I want to thank to my wife and parents. My wife has been a great source of inspiration and support. My parents have encouraged me through my entire education.

Contents

Chapter 1

Introduction

The time constant of basic physical, chemical, and biological dynamics is on the order of picoseconds and femtoseconds [1-4]. For example, transition states and reaction intermediates are on the picosecond time scale and molecular vibrational motion is on the femtosecond time scale. To study these ultrafast dynamics, the structural information at different time delays is necessary to understand the dynamics of chemical reactions and other molecular transitions. Techniques with faster time resolution than those dynamics are necessary to directly probe ultrafast dynamics in the nuclear and electronic properties of sample molecules. If the time resolution of probe technique is longer than ultrafast dynamics, the structural change obtained is only the average change in the time resolution instead of real time structural change of the ultrafast dynamics. Therefore, a probe with enough time resolution to track the ultrafast dynamics and a pump with enough peak power to trigger the dynamics in ultrafast time are necessary to study time resolved dynamics. The developments of laser technology make the study of ultrafast dynamics possible.

1.1 Spin crossover

The most important part of my doctoral research is a study of a photoinduced molecular phase transition, which is known as a phenomenon of spin crossover (SCO). The SCO is a conversion from the low spin (LS) ground state to the high spin (HS) excited state (or visa versa) because of the changes of temperature or pressure, light absorptions, and influences of a magnetic field [5,6]. L. Cambi and L. Szegö first discovered the phenomenon of thermal SCO dynamics by observing the anomalous magnetic behavior in the iron(III) dithiocarbamate complexes [7]. In femtochemistry and chemical engineering, directing the macroscopic functionalities by controlling the molecular switching would enable tremendous developments in technological applications [8,9]. SCO materials have multiple stable or metastable states depending on the environment. This inherent bistability of the SCO dynamics can change the color and the magnetic of the SCO materials by switching the states between the LS state and the HS state [10]. For example, one of most important applications of the SCO dynamics is photo-switchable devices. These devices require materials to achieve fast spin transitions between the LS state and the HS state as turning ON and OFF [10]. Furthermore, the SCO materials can reduce the size of data storages and increase the capacity of photo-switchable devices, because their size is as small as molecules and they exhibit both the bistablilty and the thermal hysteresis [10]. Therefore, the SCO materials have become perfect candidates to develop the photo-switchable devices, data storages and optical memories.

1.2 Time-resolved studies of photoinduced SCO

Photoinduced spin transition in a Fe(II) compounds has an enormous impact on the research of the SCO dynamics. It offers a good sample system to study the dynamics of the intersystem crossing process between the HS state and the LS state, while its interesting photo physical phenomenon allows the SCO compounds to be a good candidate of the photo-switchable devices. Direct SCO from the LS ground state to the HS excited state (or vice-versa) is impossible duo to dipole-forbidden. Therefore, photoinduced SCO dynamics must occur through relaxation from higher excited states. The term “light-induced excited state spin trapping (LIESST)” is used to describe this phenomenon [10].

Photoinduced SCO dynamics undergo ultrafast photoswitching of spin state involving both electronic changes and atomic motions. After photoexcitation of the LS ground state, an electron is first excited from the *d* orbitals from metal center to so called metal ligand charge transfer state (MLCT). Then, the excited molecule relaxes through intersystem crossing (ISC) to the HS excited state. Multiple methods, including transient absorption and reflection spectroscopies [11-19], X-ray absorption near edge (XANES) [20-26], and Raman spectroscopy [27], have been used to study the mechanisms of LIESST (or vice-versa reverse-LIESST). The electronic transitions associated with SCO have been identified as a two-step intersystem crossing. It is an extremely fast relaxation of short-lived intermediate state in sub-150 fs, followed by vibrational cooling of the photoinduced high spin state in ~1.5 ps [11,19-21].

For the atomic motions in SCO, the metal-ligand bond elongation (Fe-N bond in Fe(II) SCO compounds) is generally considered as one of the most important consequences of SCO [6]. The metal-ligand bond elongation is explained by the changes in occupancies of the orbitals. Two of the six *d* electrons occupy the anti-bonding orbitals in the HS state, while all six *d* electrons are in the non-bonding orbitals in the LS state. Furthermore, the largest geometrical changes induced by the SCO occur for the metal-ligand distance, and it is taken as the primary reaction coordinate along which the LS-HS transition occurs [28]. The metal-ligand bond elongation has been reported to be directly correlated in time to the electronic state dynamics observed by changes in the spectral features of complex, following with other ligand motions [20,21,25]. However, optical spectroscopies are more sensitive to the electronic state changes instead of atomic motions. For the XANES studies, XANES as every spectroscopy measures energy levels and relies on further modelling to speculate the metal-ligand bond elongation. Therefore, it is also not a direct probe of the atomic motions.

1.3 Time-resolved electron diffraction

In ultrafast physics and chemistry, pump-probe spectroscopy (time-resolved spectroscopy) is generally used to study the dynamic processes. In a typical pump-probe experiment, the dynamics of samples are tracked by the probe after the illumination of the samples by the pump. By changing the time delay between the pump and the probe, the ultrafast dynamics can be monitored.

1.3.1 Femtosecond laser

In 1960, T. Maiman [29] operated the first laser based on the theory of spontaneous emission established by A. Einstein. In 1962, the first Q-switching laser was developed by R. W. Hellwarth and F. J. Mcclung [30,31]. The principle of Q-switching is to obtain short pulses at high peak power by storing laser energy in the medium, and the peak power of such a laser can be 600 kW with a pulse duration of down to few nanoseconds. Later, mode-locking techniques, including active mode-locking and passive mode-locking, are introduced to further reduce the pulse duration and increase the peak power [32]. With the development of CPA (Chirped Pulse Amplification) technique, it is now possible to generate ultrashort laser pulses with very high peak power [33].

Femtosecond laser pulses have ultrashort pulse duration in the time domain and wide bandwidth in the frequency domain. Even though the average power of the femtosecond laser is low, the peak power of the femtosecond laser can be ultrahigh. These kind of femtosecond laser pulses make possible the study of ultrafast dynamics. Many ultrafast physical, chemical and biological dynamics which cannot studied by traditional experimental methods have been observed by the use of femtosecond laser [34,35].

1.3.2 Atomic spatial resolution of electron pulses

In order to study ultrafast dynamics, the probe needs to have not only ultrafast temporal resolution but also enough spatial resolution. The human eye has a spatial resolution of 0.1 mm. Optical microscopes invented in the 17th century have 200 nm spatial resolution, so R. Hooke was able to observe biological cells with ~1 μm size by optical microscopes.

However, the size of molecules is only 1 Å (0.1 nm), so they have to be studied by electron diffraction, which has better spatial resolution. This section contains many references from Zhou [36].

In 1927, C. J. Davisson and L. H. Germer demonstrated interference patterns by passing 100 eV electron beams through single crystal Ni films. Around the same time, G. P. Thomson also observed the interference patterns by passing 20 keV electron beams through polycrystalline films. G. P. Thomson and C. J. Davisson shared the Nobel Prize in 1937 for the discovery of the electron diffraction.

According to Abbe's equation, the spatial resolution R in a perfect optical system is given by:

$$R = \frac{0.612\lambda}{\mu sin\beta} \tag{1.1}$$

where λ is the wavelength of the radiation, μ is the refractive index of the view medium, β is half aperture angle in radians.

The wavelength of visible light ranges from 390 to 700 nm, so visible light can theoretically resolve up to 200 nm. The wavelength of electron is ~0.0037 nm at 100 kV accelerating voltage, so electrons can theoretically resolve down to 0.012 nm, based on Abbe's equation.

1.3.3 Femtosecond electron pulses

The biggest challenge in femtosecond electron diffraction (FED) is producing femtosecond electron pulses containing large numbers of electrons [37]. The pulse duration of electron pulses increases rapidly after the photocathode because of the space charge effect and the initial kinetic energy distribution of the electrons.

In order to overcome the space charge effect to generate femtosecond electron pulses, research groups around the world introduced several different methods.

The Zewail group [38,39] and others groups [40,41] reduced the electron number to several thousands to avoid the space charge effect, and increased the repetition rate to collect electron diffraction patterns with enough signal-to-noise ratio. This kind of approach restricts the type of samples that can be studied to those that present reversibility after photoexcitation and high thermal conductivity to speed the cooling down up. In recent developments, the Zewail group [39] also demonstrated an electron source with almost single electron per pulse, but its repetition rate is set to be on the order of MHz which is even harder for most samples. The Musumecci group [42] and others [43-45] increased the speed of the electrons using a MV high voltage to reduce the propagation time of the electron pulses. Shorter propagation time decreases the duration of the space charge effect. However, MeV electron beams have electrons scatter at smaller angles, so small electron diffraction patterns generated by MeV electron pulses cannot be easily analyzed. On the other hand, MeV electron pulses can damage samples in short time. Siwick, Hebeisen, and coworkers from the Dwayne Miller group [46,47] designed very compact electron guns to reduce the overall length between the photocathode and samples to 3 cm and increase the high voltage applied on the photocathode to 30-100 kV. A shorter propagation distance and faster electrons can decrease the propagation time of electron pulses to minimize the influence from the space charge effect. The design of short electron gun requires ultraflat photocathode and anode to avoid arcing between them. Although compact electron gun design can generate femtosecond electron pulses, the number of electrons is still limited to be less than 10^4 electrons per electron pulse. In order to study ultrafast dynamics by FED, the pulse duration must be sub-picosecond with enough brightness. However, the propagation distance between the photocathode and the samples in the compact electron guns cannot be unlimited short to achieve ultrabright and femtosecond electron pulses.

In this thesis, another kind of FED setup is used to study the ultrafast dynamics with femtosecond temporal resolution. Instead of reducing propagation time of the electron pulses to generate femtosecond electron pulses, it is possible to reverse the chirp of electrons by a time-dependent electric field to accelerate the back of the electron pulse and decelerate the front [37]. Therefore, the design of the FED setup is not limited by the propagation time of electron pulses. The distance between the photocathode and samples can be more than 50 cm in our FED setup at the University of Toronto, while the brightness of the electron pulses are tens of times higher than typical DC FED setups. A larger distance between the photocathode and the sample gives more flexibility for experiments such as space for an additional cold finger and a rotation stage for different experiments. The electron number per pulse can be more than 300,000, and the pulse duration can still be sub 500 fs at the sample position [49,50]. Three research groups, led by Jom Luiten at the TU Eindhoven [48], Siwick Bradley [48] at the McGill University, and Dwayne Miller at the University of Toronto [49] developed the first FED gun with RF compression.

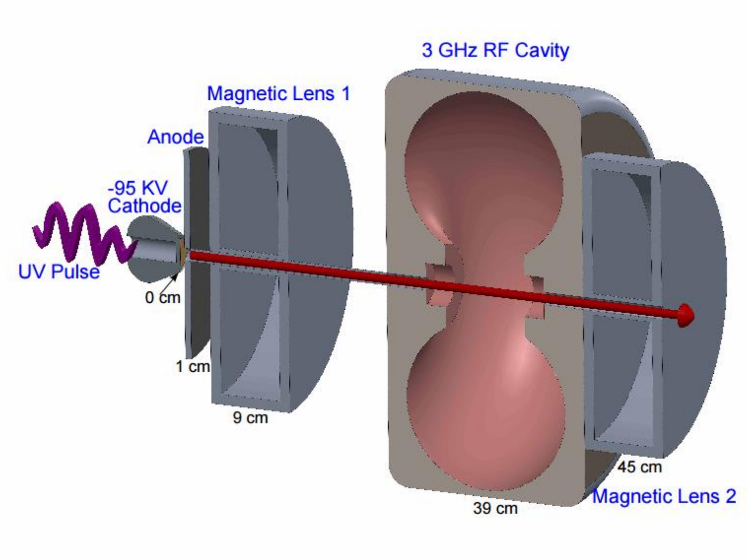

Figure 1.1: General Schematic of the Two Lens Hybrid DC-RF Pulse Compression System. The electron bunch is accelerated through a 95 keV extraction field, focused by two magnetic lens, and rebunched by the RF cavity at the sample position. Reprinted with permission from [49]. © 2012 Optical Society of America

1.4 Overview of the thesis

In this thesis, we employ femtosecond electron diffraction (FED), a direct measurement of the nuclear coordinates to study the atomic motions during the photoinduced SCO in single crystal $[Fe(PM–AzA)_2](NCS)_2$. FED has been uniquely calibrated by exploiting the thermal cycling of the high spin and low spin states of SCO over systems to show it has enough spatial resolution to track the metal-ligand elongation and other atomic motions during SCO transitions. Furthermore, a photo-triggered streak camera is used to characterize the temporal resolution of our DC-RF hybrid electron source. Our FED has atomic spatial resolution and sub-300 fs temporal resolution to study the atomic motions in SCO transitions.

After the FED data analysis including structure factor calculations and a structural refinement algorithm based on a parameterized molecular model, a molecule movie of the photoinduced SCO transition is obtained. The relationship between the metal-ligand elongation and electronic state dynamics is discussed. A molecule movie of the photoinduced SCO transitions is presented by three key dynamical groups and temporal evolution of each key dynamical group.

Chapter 2 gives an overview of the experimental setup used in femtosecond electron diffraction (FED). All important parts in the setup are explained with detailed information. The most critical component in FED is the RF cavity which is employed to reduce the pulse duration of the electron pulses to the order of femtoseconds.

Chapter 3 introduces the time-resolved streak camera which is used to characterize the electron pulses from our DC-RF electron source to prove its femtosecond pulse duration and high brightness. Furthermore, the streak camera is used to measure timing problems in our FED system, and a time-stamping technique is introduced to correct the timing problems in order to improve the temporal resolution of our FED system.

Chapter 4 offers a brief overview of fundamental information of electron crystallography. The time resolved crystallography also discussed for further FED data analysis.

Chapter 5 gives an overview of SCO dynamics. Then, multiple important time-resolved studies of the photoinduced SCO dynamics are discussed, including time-resolved XANES and UV-Vis spectroscopy studies. Furthermore, recent studies of single crystal $[Fe(PM\text{-}AzA)_2](NCS)_2$ are summarized for further FED experiments.

Chapter 6 shows the FED experimental results, focusing on the ultrafast structural change of the photoinduced SCO dynamics in single crystal $[Fe(PM–AzA)_2](NCS)_2$. The time-resolved electron diffraction patterns are analyzed to present the atomic motions in the SCO transition with atomic spatial resolution and femtosecond temporal resolution. We apply structure factor calculations and a structural refinement algorithm based on a parameterized molecular model to discuss and obtain a molecule movie of the photoinduced SCO transition.

Chapter 7 summarizes the conclusion obtained in this thesis. An overview of future work on the photoinduced SCO dynamics is discussed.

Chapter 2

Experimental Setup of RF Compressed Femtosecond Electron Source

This chapter describes the components of our ultrabright femtosecond electron source at the University of Toronto, including the laser system, the electron gun, the RF cavity, and the sample chamber [49-51]. The most critical component is the RF cavity. It is employed to reduce the pulse duration of the electron pulses to the order of femtoseconds at the sample position.

A schematic and a photograph of the RF compressed femtosecond electron diffraction setup at the University of Toronto are shown in Figure 2.1. Femtosecond electron diffraction is a time-dependent pump-probe experiment. Laser pulses of 60 fs full width at half maximum (FWHM) duration, centered at 800 nm and within a repetition rate of 100 Hz, are employed to excite samples as the pump, and the femtosecond electron pulses are used to measure ultrafast structure changes as the probe.

The output of a Ti:Al_2O_3 regenerative amplifier the laser system is split to two laser beams by a 1:9 beam splitter. The 10% intensity beam is directed to a third harmonic generation (THG) system. The frequency-tripled laser beam at 267 nm (the third harmonic) is used to produce photo-electrons in the electron gun. They are then accelerated to 95 keV by the photocathode and the anode. The electron pulses are also focused transversely by a magnetic lens before the RF cavity to optimize in the transverse direction for more efficient RF compression.

The FED setup at the University of Toronto is mainly built by Dr. Meng Gao and Dr. Hubert Jean-Ruel. This project was initiated and led by Prof. R. J. Dwayne Miller. Dr. Maher Harb performed the initial RF compression simulations, designed the diffractometer, and wrote the initial experimental control software. Dr. Sergui Krulig completed the first GPT and Superfish simulations to help in the design of the RF cavity in collaboration with Mark de Jong from Canadian Light Source (CLS). This chapter contains many references about the FED setup from Dr. Meng Gao, Dr. Hubert Jean-Ruel [49-53], my master dissertation [54].

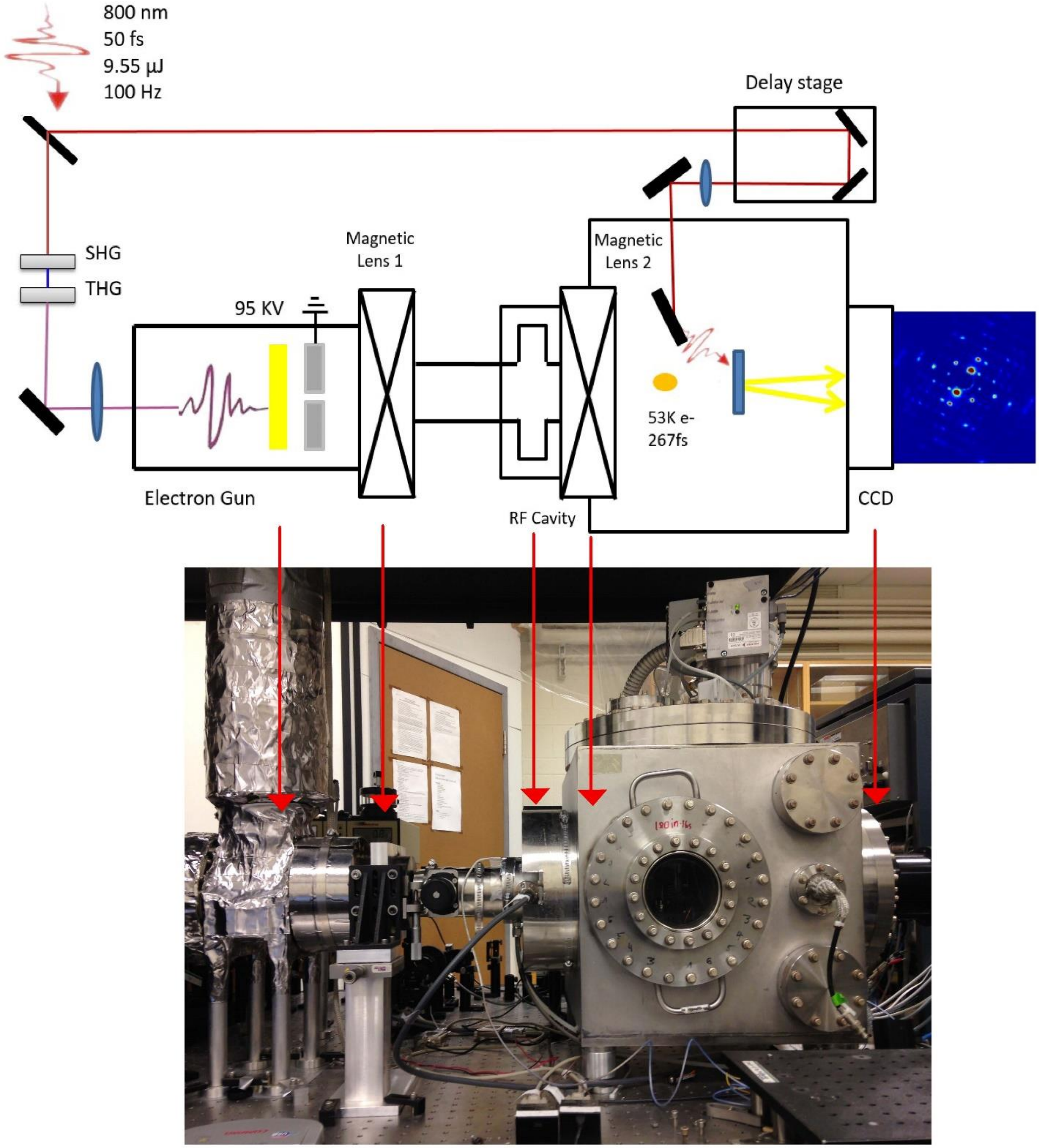

Figure 2.1: Schematic and photograph of the RF compressed femtosecond electron at the University of Toronto. Femtosecond laser pulses are split by a beam splitter. The 10% intensity laser beam is employed to generate femtosecond electron pulses, and the remaining intensity are used to trigger ultrafast dynamics.

2.1 Laser system

FED is a classic pump-probe experiment, and the femtosecond laser system is one of the most important components in our FED system. At first, it pumps the samples to trigger ultrafast dynamics, so the pulse duration of this femtosecond laser beam determines the minimum time resolution of the FED experiment. Then, the laser is also used to generate femtosecond electron pulses by the photoelectric effect to probe ultrafast dynamics, so the femtosecond laser pulses determine the initial time resolution of the electron pulses. Furthermore, the RF compression system is also required to be synchronized to the femtosecond laser.

The temporal resolution of a FED experiment is the convolution of several factors, and it can be estimated as follows [37]:

$$\tau_{total}^2 = \tau_{laser}^2 + \tau_{electron}^2 + (\tau_{geometric} + \tau_{sampe})^2 \tag{2.1}$$

where τ_{laser} and τ_{electron} are the pulse duration of the pump laser and the probe electron pulse, respectively, $\tau_{\mathrm{geometric}}$ is from the temporal broadening of the crossing angle [37], τ_{sample} is from the velocity mismatch [37] between the electron pulse and the laser pulse. The contribution from τ_{sample} can be ignored for thin (10-100 nm) samples. Therefore, the femtosecond laser system plays an important role in determining the temporal resolution of the RF-compressed femtosecond electron diffraction system.

The femtosecond laser system has two major parts: an oscillator and a regenerative amplifier [52]. A Micra Ti:Sapphire oscillator from Coherence Inc. generates a pulse train (repetition rate 75 MHz, wavelength centered at 800 nm, average power 350 mW, and pulse duration 50 fs FWHM). The pulses from the oscillator seed a home-built regenerative amplifier after a stretcher. The home-built regenerative amplifier is pumped by a Q-switched Nd:YLF nanosecond laser (average power 8 W and wavelength centered at 532 nm). After the grating compressor, the final output of the laser system has 0.4 mJ intensity, 50 fs pulse duration with 1 kHz repetition rate, and is centered at 800 nm with 30 nm of bandwidth FWHM. The repetition rate can be changed depending on pump conditions.

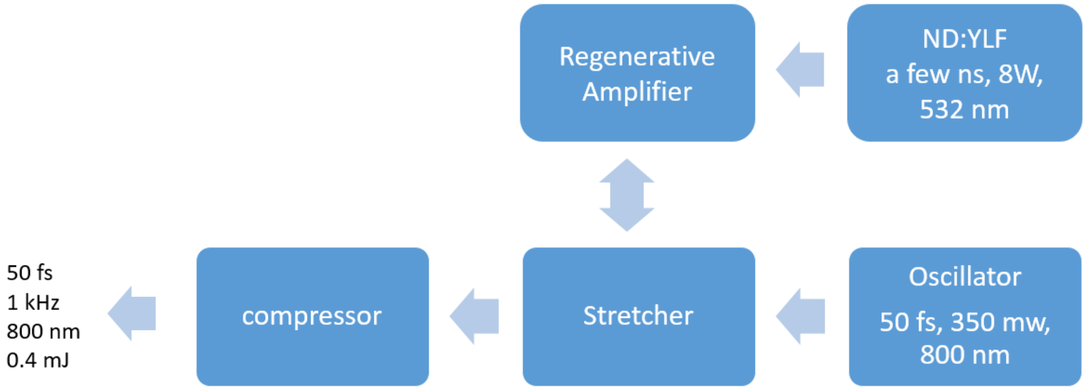

Figure 2.2: Laser system layout used in this thesis.

A higher repetition rate can improve the signal-to-noise ratio of the ultrafast signal and the efficiency of data collections. However, some samples require a lower repetition rate to avoid thermal damages from the heat accumulation. That was the case of the (EDO-TTF)$_2$PF$_6$ metal-to-insulator phase transition study where the repetition rate was set to 10 Hz [50]. In other samples, a lower repetition rate is desirable because more time is necessary for recovery from the excited state to the ground state. For the [Fe(PM-AzA)$_2$](NCS)$_2$ spin crossover dynamics study, the repetition rate is set to be 100 Hz to make sure samples have recovered from the excited HS state to the ground LS state before the arrive of the next pump laser pulse [19].

2.2 Electron source

The electron pulses applied in a FED study must have femtosecond during to probe the ultrafast structure changes of photo-excited dynamics, a feature no met by traditional electron field emission and thermionic emission. In our FED setup, photoelectric effect is employed to generate ultrafast electron pulses as probe, since the response time of metal photocathodes such as gold and silver is sub-50 fs [52,53]. Therefore, the electron pulses generated from such photocathodes by femtosecond laser pulses inherit the femtosecond pulse duration of the laser pulses.

Electron gun

The electron gun is a vacuum chamber maintained at a pressure of 10^{-9} mbar. This is due to avoid electrical arcs across the photocathode and the anode.

UV laser pulses at 267 nm generated by the THG enter the electron gun and illuminate a 20 nm thick gold film deposited on a 1 mm thick sapphire substrate. The THG setup consist of two BBO (beta-barium borate) crystals and a sapphire disk. The first crystal generates a 400 nm beam from the fundamental 800 nm (second harmonic generation) with an efficiency of 30 %. The 400 nm beam and the remain of the 800 nm one pass through the sapphire disk (time delay compensator) and are combine in the second BBO crystal (sum of frequency generation) to create a 267 nm beam. In order to generate photo-electrons, the energy of an absorbed photon in the photocathode materials must be higher than the work function (the electron binding energy) of the photocathode material. The photocathode material in our electron gun is a 20 nm thick gold film, and the work function of the gold film is 3.8 eV [55,56]. Therefore, we choose the laser beam centered at 267 nm with 4.6 eV photo energy to generate photo-electrons in the electron gun.

A 100 kV variable power supply provides the 95 kV for the photocathode. The anode, mounted 10 mm downstream, is directly attached to the vacuum chamber which defines its potential to 0 (grounded). This establishes a 10 kV/mm extraction field. The anode is a 4-inch diameter flat piece of Borum doped Si wafer with a pinhole in the center for the extraction of the electron pulses. At the photocathode, the laser beam transverse width is 30 µm.

The brightness of the electron pulse relates to the electron density of the electron pulses, which depends on the electron number and the transverse width of the electron pulses [52]:

$$d_e = \frac{N_e}{\pi * \left(\frac{w_e}{2}\right)^2} \tag{2.2}$$

where N_e is the electron number in one electron pulse, the w_e is the FWHM width of the electron pulse, and d_e is the electron density in area. The transverse width of the electron pulses at the sample position is ~300 µm. This transverse width is optimized for most organic and inorganic samples. If the transverse width is focused to be less than 300 μm, the pulse duration of the electron pulses will increase because of the space charge effect. If it is focused to be more than 500 μm, it is challenging to prepare large enough single crystal samples for many interesting systems. Since the transverse width of the electron pulses is fixed at 300 μm in most FED experiments, the brightness of the electron pulses is directly proportional to the electron number in each electron pulse. Therefore, we use electron number to represent the brightness of the electron pulses in this thesis.

The width of the pinhole on the anode determines the brightness of the electron pulses and the stability of the brightness over time. Specifically, the width of the pinhole is proportional to the brightness of the electron pulses extracted from the electron gun. In Figure 2.3, we notice there is a saturated regime of the brightness of the electron pulses. If the UV laser power exciting the photocathode is in this regime, the fluctuation in the UV laser power have little effect in the electron brightness. In the $[Fe(PM\text{-}AzA)_2](NCS)_2$ spin crossover study, the relative changes in the diffraction intensity of Bragg peaks is only ~3% because of small structure changes during the spin switching from the low spin state to the high spin state. In order to improve the signal-to-noise ratio of the time-resolved traces, the width of pinhole on the anode was reduced from 500 μm to 200 μm. The smaller anode pinhole decreased the electron number to 53,000 with < 0.5% stability of single electron brightness, while the larger pinhole can extract 300,000 electrons with 1% stability.

In Figure 2.3, the electron number of single electron pulse varies from 10^3 to 10^5 by changing UV laser intensity on the photocathode. As mentioned before, a saturated regime of the brightness of the electron pulses occurs above ~150 nJ UV laser power. In our FED experiments, we usually set the UV laser power at this regime, such that the fluctuation of UV laser power has minimal contribution to the brightness.

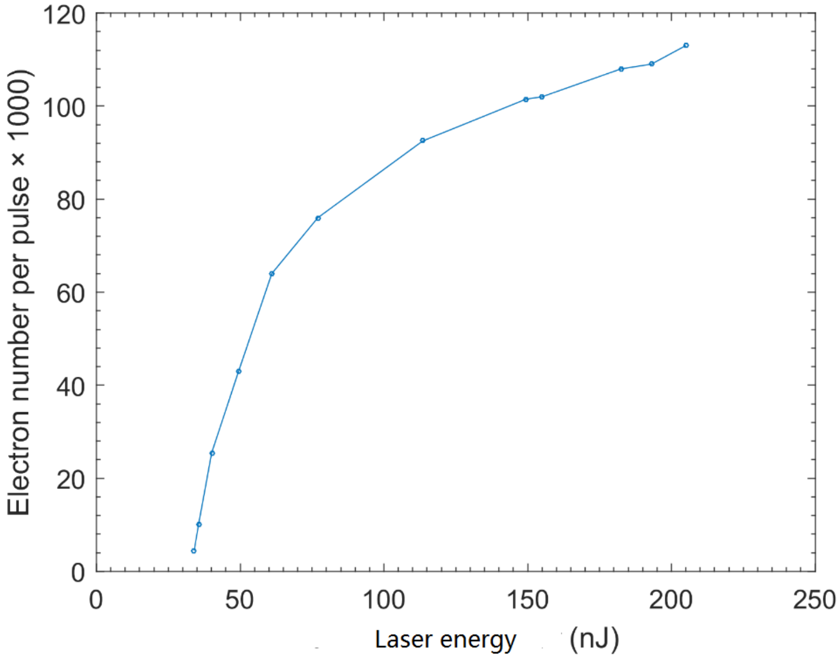

Figure 2.3: Electron number per pulse vs. 267 nm laser energy. The relationship between the laser illuminating on the photocathode and the output electron number from anode is not linear. After 110 nJ 267 nm laser, the output electron number is saturated. Therefore, if the input 267 nm laser energy is higher than 110 nJ, the fluctuation of electron brightness from the UV laser energy can be improved.

Magnetic lenses

The transverse width of the electron pulses increases during the propagation from the anode in the electron gun to a charge-coupled device (CCD) camera, the detector because of the space charge effect. However, a ~300 µm transverse width of the electron pulses at the sample position is ideal for the best RF recompression efficiency and pump-probe overlap. The diffracted electron pulses also need to be focused on the CCD camera to obtain diffraction patterns for further data analysis. On the other hand, the RF compression cavity increases the transverse width of the electron pulses while compressing the longitudinal width (pulse duration). Therefore, two magnetic lens are placed in the FED system in Figure 2.1. The first is placed between the electron gun and the RF compression cavity to optimize the efficiency of the RF compression. The second one is mounted after the RF compression cavity to focus the electron pulses onto both the sample position and the CCD camera. By changing the RF field amplitude and the current on the two magnetic lens, the transverse width of the electron pulses is optimized for imaging the electron diffraction patterns while the pulse duration (longitudinal width) is kept at <500 fs [52,53].

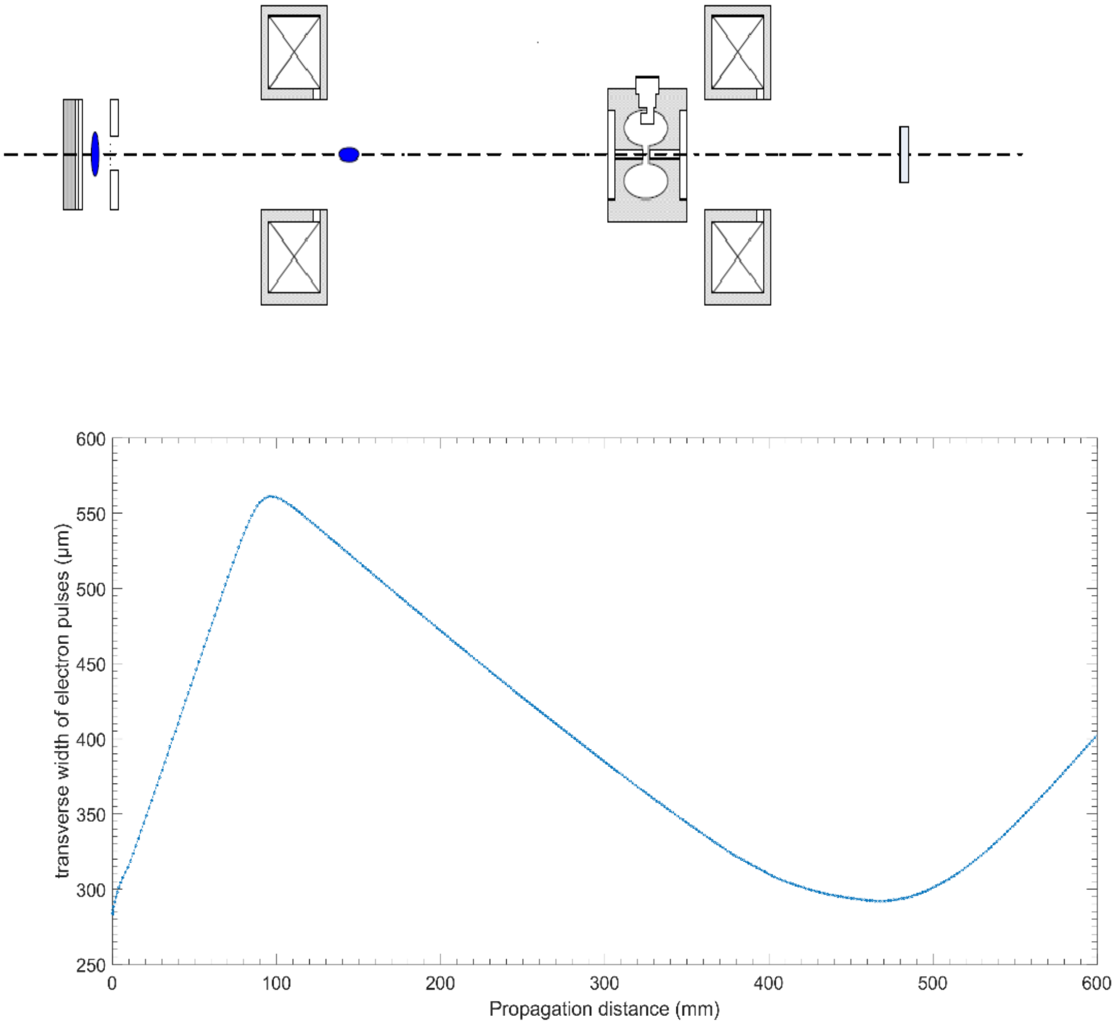

Figure 2.4: GPT [57] simulation of transverse width of electron pulses vs. propagation distance.

Sample chamber

The sample chamber in our FED setup is a 40×40×40 cm^3 cubic chamber (see Figure 2.1). The sample chamber is connected to the electron gun by a vacuum valve to make sure that the electron gun can be kept in ultrahigh vacuum (10^{-9} mbar) while the sample chamber is opened to change samples or setup experiments (adjusting the position of optical mirrors, adding a cold finger to cool down the samples, and installing a streak camera for pulse duration measurements). The sample chamber has a set of three axes of MICOS PLS-85 translation stage. The travel range of them is 10 cm with 1 μm accuracy. An optical bread board is installed on the translation stages for mounting sample holders, optics mirrors, and streak cameras.

Detectors

The detector is a Spectral Instruments 800 series ultra low noise fiber-coupled CCD camera. The pixel resolution of the CCD chip is 2048×2048, and each pixel is 14×14 μm^2. The readout noise can be decreased greatly to 3 counts per pixel by cooling the CCD chip to -20 degrees Celsius. The fiber plate is coated with a 50 nm thick aluminium layer to decrease the unwanted background noise from the scattered pump laser beam. After electrons pulses go through the sample, most of the electrons are unscattered and collected as the (0 0 0) Bragg peak on the electron diffraction pattern. Some electrons are scattered by the sample and contain rich transient structural information relevant to the study of the ultrafast dynamics.

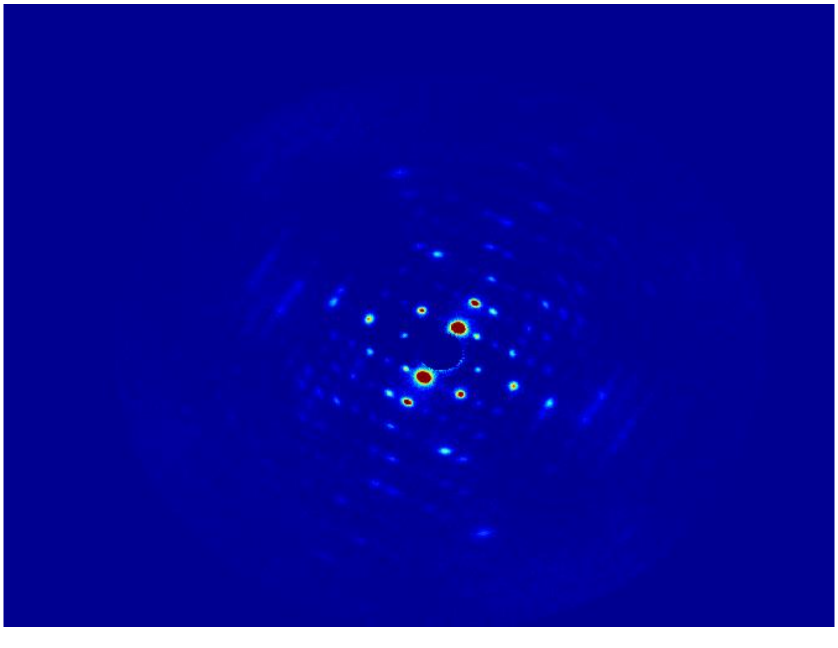

Figure 2.5: A typical electron diffraction pattern of single crystal $[Fe(PM\text{-}AzA)_2](NCS)_2$. The (000) Bragg peak and the inelastic scattering background are removed by software to obtain a clear diffraction pattern.

2.3 RF compression system

One of the most important feature of our FED system is the RF compression system. It is necessary to compress the pulse duration of the electron pulses at sample position to obtain ultrabright femtosecond electron pulses.

2.3.1 Space change effect in electron source

The on-axis potential of the charge distribution is given by [37]

$$V(z) = \frac{N}{2\varepsilon_0 \pi r^2}\left[\sqrt{z^2 + r^2} - z\right] \tag{2.3}$$

where N is the number of electrons in the pulse, r is the beam radius, e is the electron charge, ε_0 is the permittivity of free space, and z is the axial distance from the center of the pulse. Therefore, the force of an on-axis electron is given by

$$F_z\big|_{z=l/2} = -e\frac{dV}{dz}\bigg|_{z=l/2} = m\frac{dv_z}{dt}\bigg|_{z=l/2} \tag{2.4}$$

where l is the total length of an on-axis electron at the leading edge of a pulse. $dl/dt=2v_z$, so the equation can be rewrite as

$$\frac{d^2 l}{dt^2} = \frac{Ne^2}{m\varepsilon_0 \pi r^2}\left(1 - \frac{l}{\sqrt{l^2+4r^2}}\right) \tag{2.5}$$

In Figure 2.6, Siwick *et al.* [37] simulated the longitudinal phase-space evolution of an electron pulse propagating from N-body charged particle simulations. The initial electron pulse on surface of a photocathode will quickly broaden and develop a linear chirp.

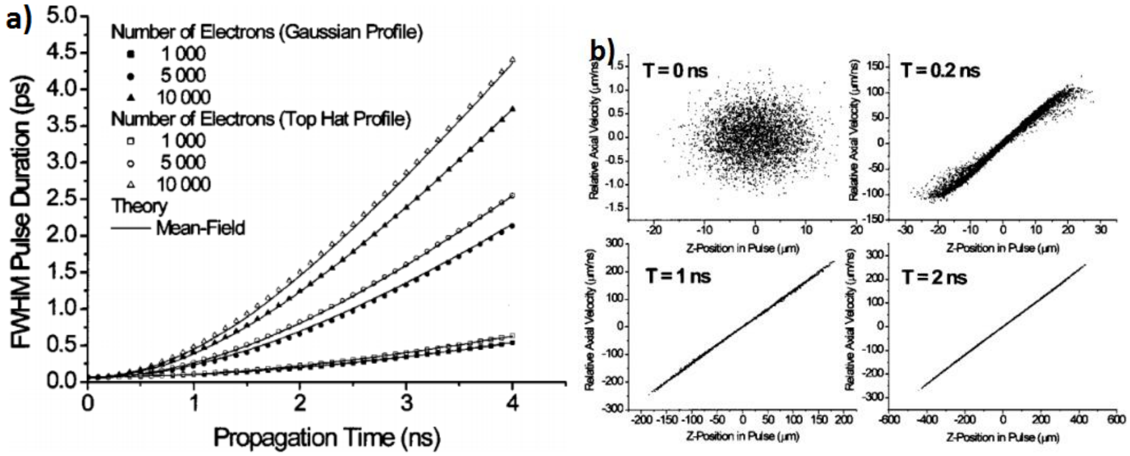

Figure 2.6, Siwick *et al*. simulated the longitudinal phase-space evolution of an electron bunch. (a) Simulation shows the FWHM pulse duration vs. propagation time for Gaussian and top hat beams. It is clear to find the number of electrons in the electron beam decides the broaden speed in propagation. (b) axial velocity vs. axial position for all electrons in the beam at four different propagation time. Because of the space charge effect, the front part of electron beam is accelerated and the back part of electron beam is decelerated. In only 0.2 ns, electron beam has been broadened. Reprinted with permission from [37]. ©2002 American Institute of Physics.

In Figure 2.6 and equation 2.5, the simulation shows that the pulse duration of electron pulses accelerated by the same high voltage depends on the brightness and the travel time of the electron pulses.

2.3.2 DC-RF hybrid electron source

The biggest challenge of FED setups is the space charge effect which makes delivering ultrabright femtosecond electron pulses very difficult. Several different types of FED setups have been built to achieve femtosecond electron pulses by compact electron sources [46,47], single electron sources [38], and MeV electron sources [42-45]. However, there is another way to achieve femtosecond electron pulses by recompressing the electron pulses by a time-dependent electric field [48].

Siwick et al. [37] first found that the initial disk charge at the photocathode broadens quickly into a linear chirp distribution. The principle of RF compression is from pulse compression in optics. Any laser pulses with a linear chirp can be compressed using a system of optical elements to reverse the phase space distribution, such as a grating compressor.

The RF cavity in our DC-RF hybrid electron source is cylindrically symmetric and its geometry is optimized for maximizing the coupling efficiency and minimizing the power dissipation [52].

The longitudinal electric field E_z near the central z axis of the RF cavity is given by [49]:

$$E_z = E_0 \sin(2\pi f t + \Phi_0) \tag{2.6}$$

where the E_0 is the field amplitude, f is the resonant frequency and Φ_0 is the phase. The resonance frequency of this cavity is 2.998 GHz, giving a period of 334 ps. On the other hand, the travel time of the electron pulses in the RF cavity is ~62 ps, based on the 1 cm length of the RF cavity and 1.62 x 10^8 m/s speed of the electron pulses. Therefore, for the electron pulses traveling through the RF cavity, the RF field can be considered as a linear portion of the sinusoidal function. The phase Φ_0 is set to make sure the middle part of the electron pulse receives no RF field from the RF cavity while the front and back parts are decelerated and accelerated by the RF field, respectively. Compressing the longitudinal width (pulse duration) of the electron pulses causes broadening of the transverse width of the electron pulses on the CCD screen because of the space charge effect. Therefore, the phase of the RF field can be optimized by checking the transverse width of the electron pulses.

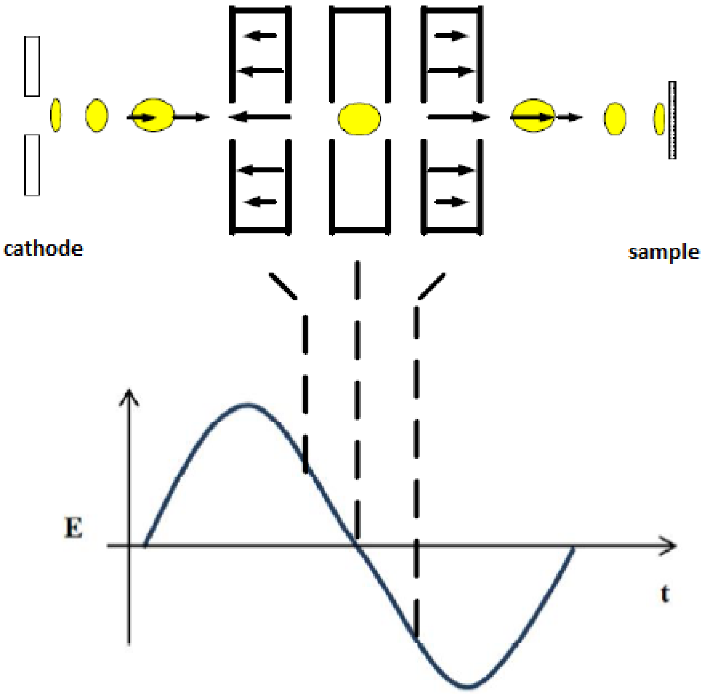

Figure 2.7: Principle of longitudinal radio frequency(RF) compression. The distribution of electron pulses emitted from the cathode broaden into a linear chirp quickly. For the electron pulses traveling in the RF cavity, the electric field can be considered as a linear portion of the sinusoidal function. The phase is optimized to make sure the middle part of the electron pulses gets no RF field. Front and back parts are decelerated and accelerated by the RF field, respectively. At the sample position, the pulse duration is compressed to sub-picosecond.

The synchronization between the RF field and the electron pulses is critical to achieve sub-picosecond pulse duration at the sample position [52,58]. If the electron pulses arrive too early or too late with respect to the zero crossing of the electric field, additional kinetic energy from the RF field will change the velocity of every individual electron pulse. Then, at the sample position, the timing jitter between the pump laser and the probe electron pulses are introduced by different velocity of the electron pulses. Even though the pulse duration of single electron pulses can be reduced by the RF field in the RF cavity to less than a picosecond, the large temporal jitter from the synchronization of the electron pulses and the RF field increases the overall pulse duration to picoseconds. In Chapter 3, more details about the timing jitter are discussed with measurements from the photo-trigged streak camera.

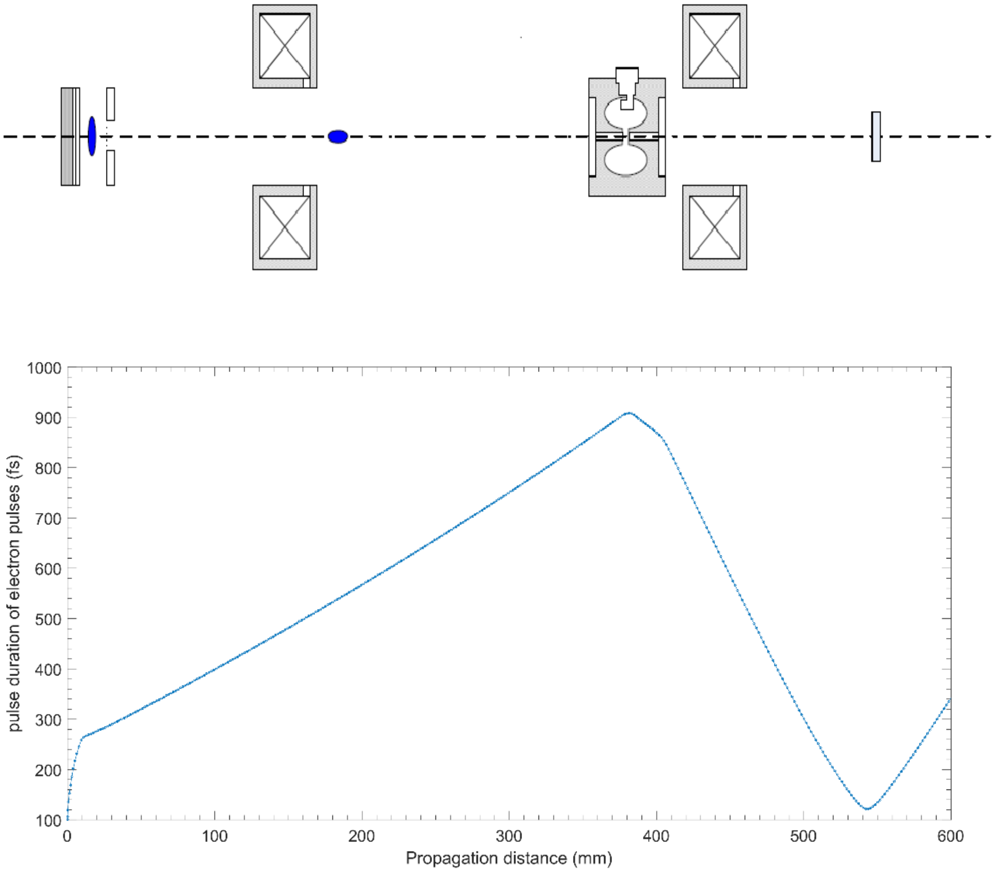

Figure 2.8 GPT [57] Simulation of pulse duration of electron pulses vs. propagation distance. A 270 nm UV pulse illuminates a gold cathode and generates an electron pulse. The electron bunch is accelerated through a 95 keV high voltage field, recompressed in the 3 GHz RF cavity, and then focused again at the sample position.

In our lab, the synchronization between the RF field and the arrival time of the electron pulses is achieved using a 3 GHz Phase-Lock Loop (PLL) synchronizer [59] developed by Acctec B.V. The frequency of the laser oscillator is locked to 75 MHz by a Synchro Locker AP from Coherent Inc.. A part of the oscillator output laser is detected and converted to an electronic signal by a fast photodiode, and the PLL filters the higher harmonic of this signal to phase lock the output of a 3 GHz Voltage Controlled Oscillator (VCO). Then, the output signal from the PLL is amplified and coupled to the RF cavity.

2.4 Overview of propagating procedure of DC-RF electron source

To summary the whole work procedure of the DC-RF hybrid femtosecond electron source, from generating the electron pulses on the photocathode to collecting the electron diffraction patterns on the CCD screen, I describe the overall of DC-RF electron source propagation in the order of time.

At first, the electron gun and sample chamber are pumped down to a vacuum better than 10^{-9} mbar and 10^{-7} mbar, respectively. The 267 nm UV laser pulses generated by THG of the 800 nm femtosecond laser pulses go through a quartz window and produces electrons by irradiating the gold photocathode in the electron gun. At this time, the electron pulses have the same temporal profile of the input laser.

Then, these electron pulses are accelerated by the electric field between the 95 kV photocathode and the grounded anode. They pass the first magnetic lens to optimize the transverse width. The pulse duration (longitudinal width) are recompressed by the RF field in the RF cavity. After the second magnetic lens, the probe femtosecond electron pulses are focused transversally and longitudinally to the sample position where they are overlapped with the pump laser pulses. In the experiment, the arrival time of the pump laser and the electron pulses must be synchronized by changing the time delay of the pump laser. On the other hand, the space overlap of the pump laser, the electron pulse, and the sample also needs to be optimized.

Finally, the electron diffraction patterns which contain transient structural information of the samples are collected by the CCD camera. By changing the time delay between the pump laser and the probe femtosecond electron pulse, a molecular movie with atomic spatial resolution and femtosecond temporal resolution can be obtained.

Chapter 3

Pulse duration and timing jitter

The work from chapter 2 introduces the radio frequency (RF) compression cavity and its principle to achieve both high temporal resolution and high brightness simultaneously. It is also important to characterize the electron pulses from our DC-RF electron source to determine its femtosecond pulse duration and high brightness. To study ultrafast atomic motions, one of the most critical features of FED setups is the femtosecond pulse duration of electron pulses. In our hybrid DC-RF electron source, the pulse duration is the key parameter which needs to be verified before time-dependent pump probe experiments are performed. Our group has applied multiple techniques to measure the pulse duration of electron pulses such as ponderomotive scattering [49,60,61], time constant measurements of the electron- phonon relaxation process in Si [53,62], and streak camera [58,63,64]. The RF compression cavity can reduce the pulse duration of ultrabright electron pulses at the sample position to ~300fs [58]. The brightness can be calculated by measuring the electrons number in single pulse and the transverse width of the beam [52].

There are two major timing problems in our DC-RF hybrid FED system [52,58]. One of the main reasons for the short-term of jitter is the amplitude-to-phase noise from the saturation effect of semiconductor photodiodes [58,55-69]. Another reason is from temperature sensitive components in the system such as the coaxial cables between the photodiode and the PLL synchronizer, the PLL itself and the RF cavity [70,71].

The second timing problem is the long-term slow arrival time drift of the probe electron pulses over several hours. The cause for this long-term time-zero shift is also temperature drift of different components. For a set of FED data with high signal-to-noise ratio, more than 20 hours of experiment time are necessary. Especially for small changes in diffraction intensity of the Bragg peaks, the longest data collection of single crystal $[Fe(PM\text{-}AzA)_2](NCS)_2$ is 40 hours continuous experiment. Although several chillers are used to stabilize the temperature of the RF cavity and PLL [49], the temperature stability of the devices still cannot be ignored.

Parts of this chapter have previously been published in the following article [58]: M. Gao, Y. Jiang, G. H. Kassier, and R. J. D. Miller. Single shot time-stamping of ultrabright radio frequency compressed electron pulses. *Appl. Phys. Lett*. 103, 033503 (2013).

3.1 DC-RF hybrid electron source and its advantage

Because of Coulomb repulsion, it is difficult for ultrafast electron source to simultaneously achieve high temporal resolution and high brightness. Typical compact DC electron sources [46,47] reduce the brightness of electron pulses and the distance between the photocathode and the sample to achieve femtosecond temporal resolution. Therefore, DC electron sources need long integration time to gather electron diffraction patterns with high signal-to-noise ratio. This limitation not only reduces the efficiency of experiment, but also increases the difficulty for irreversible dynamics. Therefore, it is crucial for ultrafast electron diffraction to overcome the Coulomb repulsion of high brightness electron bunches.

The FED setup built at the University of Toronto has a DC-RF hybrid electron source [49,50]. The main advantage of the DC-RF electron source is that the brightness of the DC-RF electron source can be much higher than the brightness of compact DC electron sources. The brightness can be increased from thousands up to half million of electrons according to the requirement of different sample systems, while the pulse duration can always be compressed to less than 500 fs at the sample position.

Higher brightness of electron pulses can increase efficiency of experiment greatly. For example, at least 10^6 electrons are necessary to obtain an electron diffraction pattern with good enough signal-to-noise ratio. The brightness of compact DC electron sources [46,47] is only 5000-10000 electrons per single electron pulse, so it will take one second to obtain one electron diffraction pattern even with the repetition rate at 1 kHz. If samples photodegrade in the pump probe experiment at 1 kHz because of accumulated heat or necessary cooling down time for samples to recover from the excited state to the ground state, the repetition rate needs to be reduced to 10 Hz [50]. However, for the DC-RF electron source, its regular brightness is up to 300,000 per single electron pulse, at least 30 times higher than the brightness of compact DC electron sources [49]. Therefore, for the same experiment setting, our DC-RF electron source can reduce the experiment time greatly. Our DC-RF electron source can also overcome limit of compact DC electron sources to study more ultrafast dynamics.

Furthermore, the distance between the photocathode and the sample in our DC-RF electron source can be much bigger than the distance in compact DC electron sources. To achieve sub-picosecond pulse duration at the sample position, compact DC systems make this distance as short as possible. The DC-RF design enables more space in the sample chamber for additional equipment (cold finger and rotation stage). Therefore, the distance between the photocathode and the sample can be adjusted based on special requirement of different samples, while the pulse duration of electron pulses still is sub 500 fs.

3.2 Streak camera

In a streak camera measurement, electron pulses are deflected in the transverse direction by a pair of streak plates with a time-dependent electric field. The magnitude of this deflection is proportional to its arrival time at the streak plates, so the velocity profile of electron pulse is displayed across the CCD (see Figure 3.1) [58,63,64]. The pulse duration can be obtained by measuring the magnitude of the deflection on the CCD and using the following equation [64]:

$$W_{str}^2 = W_{un}^2 + K_s^2 \Delta\tau_e^2 \tag{3.1}$$

where W_{str} is FWHM of streaked beam; W_{un} is FWHM of unstreaked beam; K_s is the streak velocity (SV); $\Delta\tau_e$ is the pulse duration of electron pulse. Therefore, the pulse duration of electron pulse can be obtained given K_s, W_{str} and W_{un}.

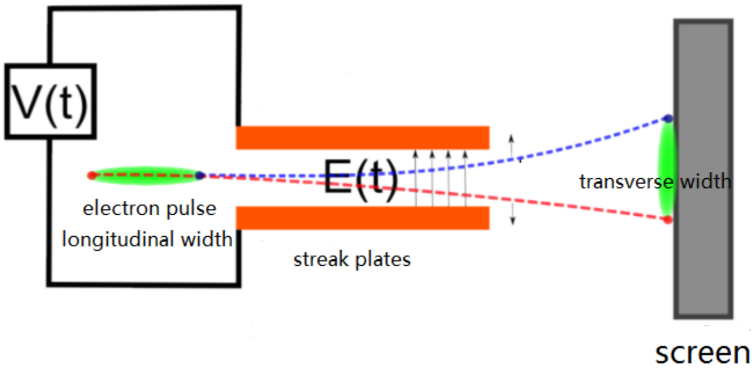

Figure 3.1: The schematics of the streak camera. The electron pulses from electron gun are deflected by a pair of streak plates with a time-dependent electric field. Therefore, temporal width of electron pulses is transferred to the transverse width on CCD screen.

The streak camera is a traditional method to measure the pulse duration of electron pulses [63,64]. The design of our streak camera is simple and small, but traditional streak cameras have limit when they are employed to characterize sub-picosecond electron pulses. The biggest challenge is preparing a photo-switch that can offer a high streak velocity >6 kV/ns and work reliably in high velocity circuit [40]. *Kassier et al.* [63] demonstrated a photo-triggered streak camera which has < 200 fs temporal resolution in accumulation.

3.2.1 Streak camera design

The streak camera from *Kassier et al.* [63] is employed to measure the pulse duration of electron pulses before every time-dependent pump-probe experiment, because the RF field amplitude applied on the RF cavity needs to be optimized for different brightness of electron pulses. Figure 3.2 shows the design of the streak camera [58,63]. 1.5 kV, 60 ns high voltage pulses generated by high voltage pulse generator are applied on the streak camera to increase life time of photo-switch. A pair of compact streak plates are gated by a gallium arsenide (GaAs) photo-switch. The gap width between two streak plates determines the streak velocity of the streak camera. In our lab, there are two different gap sizes of the streak camera. The streak camera with 200 µm gap can offer 47 pixel/ps (2.8 mrad/ps) streak velocity, and the one with 600 µm gap can offer 13 pixel/ps (0.9 mrad/ps) streak velocity [58].

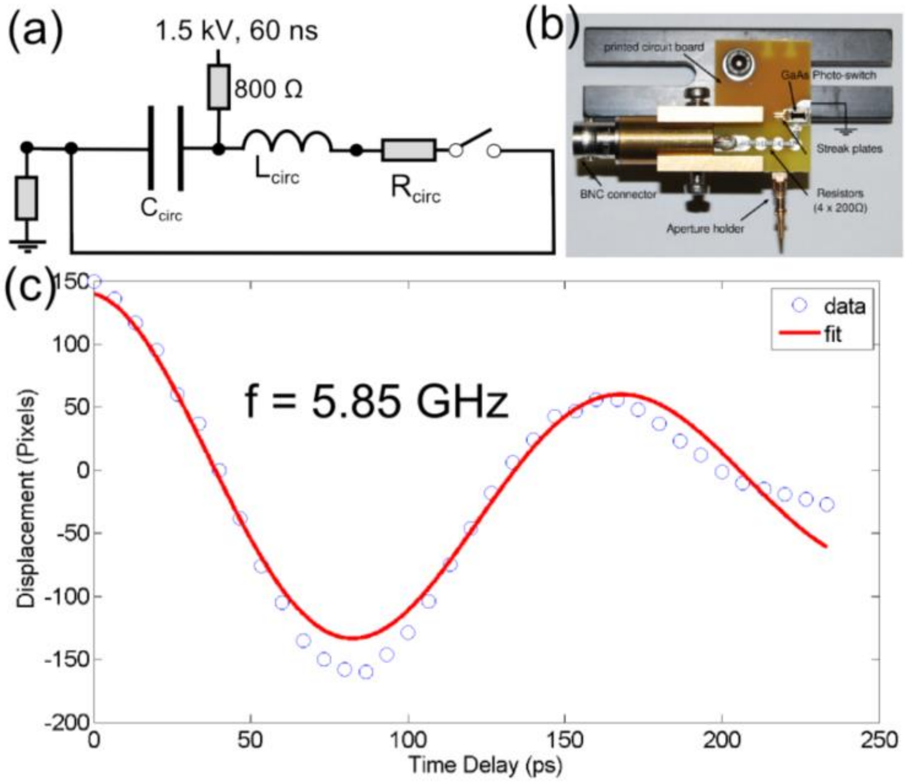

Figure 3.2: Photo-triggered streak camera design. (a) A simple LRC circuit with a photo-switch (b) the streak camera design in real space. (c) Oscillation of the electric field applied on streak plates vs. time delay of the trigger laser on the photo-switch. Reprinted with permission from [58]. ©2010 American Institute of Physics.

After the trigger laser pulse irradiates the photo-switch, the streak camera circuit launches the high voltage across the streak plates. The streak plates have a time-dependent oscillation of the electric field applied on streak plate [63]. In order to obtain the best streak velocity, the timing of the trigger laser is tuned to make sure the electrons arrive at the first zero-crossing.

3.2.2 Pulse duration of electron pulses

The streak velocity of our photo-triggered streak camera is 47 pixel/ps (2.8 mrad/ps) [58]. If the root-mean-square (RMS) streaked electron pulse size can be made as small as 5 pixels on CCD screen, the temporal resolution is about 100 fs which is high enough to measure the pulse duration of electron pulses in our hybrid DC-RF electron source.

Figure 3.3a shows the relation between the pulse duration of the electron pulses and the RF field amplitude. The RF field amplitude is varied between 1.6 MV/m to 1.75 MV/m to find the shortest pulse duration at the sample position while keeping the small transverse width.

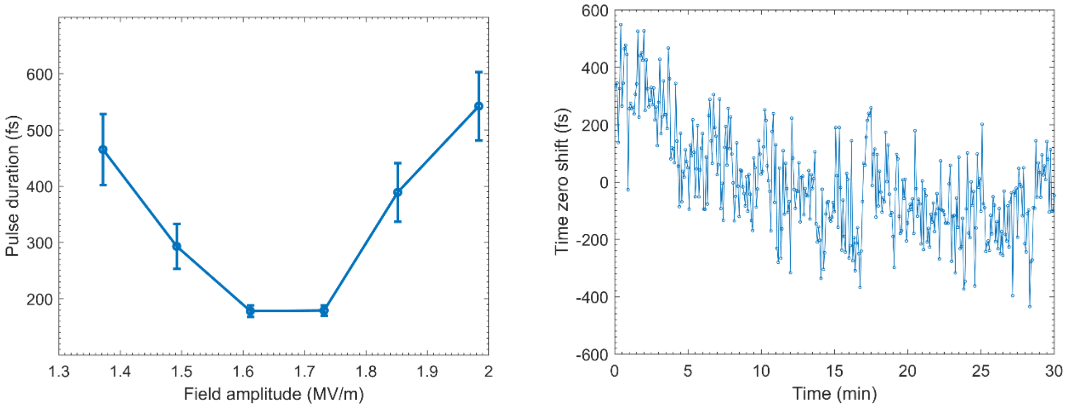

Figure 3.3: Pulse duration measurement. (a) Pulse duration measured by streak camera vs. RF field amplitude. Shortest pulse duration is 178 fs FWHM. (b) Single shot electron time-zero shift vs time. The jitter is 200 fs RMS.

In the DC-RF hybrid electron gun, the measured temporal instrument response function (IRF) gets contributions from both the 200 fs RMS arrival time jitter (Figure 3.3b) and the 178 fs FWHM pulse duration of single electron pulse (Figure 3.3a) based on 63 pixel/ps streak velocity. Thus, the accumulated pulse duration is ~300 fs FWHM with an areal density of 0.92 electron/μm^2. In Figure 3.4, we also increase streak velocity by applying more voltage on streak plates, but the pulse duration of single electron pulse stays around 180 fs FWHM.

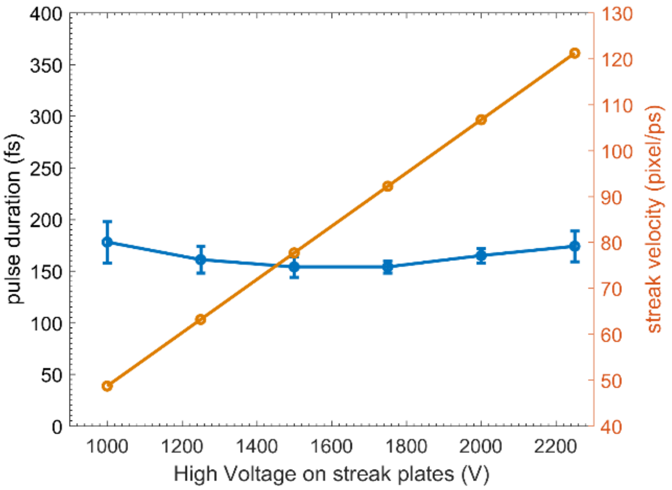

Figure 3.4: pulse duration vs. streak velocity. Pulse duration of single electron pulse stays around 180 fs FWHM at different streak velocity.

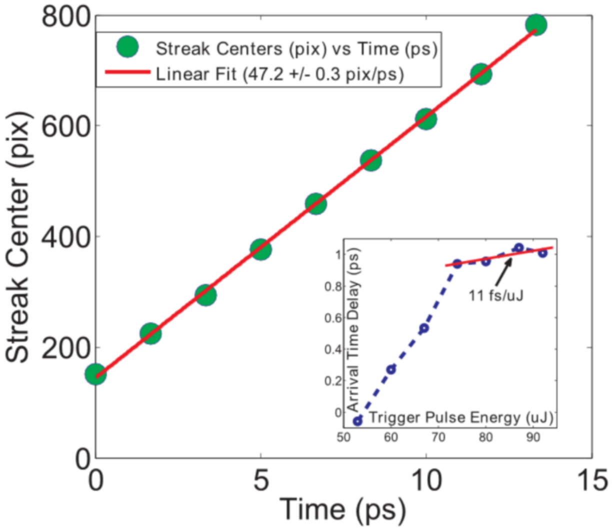

Figure 3.5: Characterization of the streak camera. The streak velocity is obtained by tuning the delay of trigger laser for the streak camera and measuring the displacement of electron pulse on the CCD screen. Inset: The streak velocity and arrival time also get influence from the trigger pulse energy. A saturated regime at 80 µJ is used, because a change in the trigger pulse energy makes a negligible contribution to the arrival time delay (11 fs/µJ) in this regime. Reprinted with permission from [58] ©2013 American Institute of Physics.

3.3. Time-stamping technique

3.3.1 Time-stamping of every single electron pulse

Time-stamping is a technique that determine the temporal overlap of the pump laser pulses and the probe electron pulses by measuring the relative arrival time of electron pulses on the photo-triggered streak camera. Since the streak camera from *Kassier et al* [63] has high enough streak velocity, our group has demonstrated the time-stamping technique by measuring the fast lattice-heating dynamics of Si [58]. The timing jitter is the fluctuation of the arrival time between pump laser and probe electron pulses at the sample position. Effects of both short-term and long-term timing jitter on the temporal resolution of the experiment can be overcome by this technique, because the time-stamping technique can track the arrival time shift of every electron pulse by measuring the displacement of streaked electron pulse on the CCD screen.

Figure 3.6 is the setup of the time-stamping experiment [58]. The 30 nm thick, (001) oriented Si is pumped by a 400 nm, 50 fs FWHM, 2.2 mJ/cm^2 laser. We first tune the first delay stage (DL1) to make sure that the pump laser and the probe electron pulses are overlapped at the sample position in time and space. Then, we adjust the second delay stage such that the electron pulses arrive at the first zero-crossing of the oscillation of the electric field applied on streak plates. Therefore, the timing of the pump laser, the trigger laser and the probe electron pulses are synchronized at the sample position. Since the trigger laser and the pump laser is split from the same laser pulse, we assume there is almost no timing jitter between them.

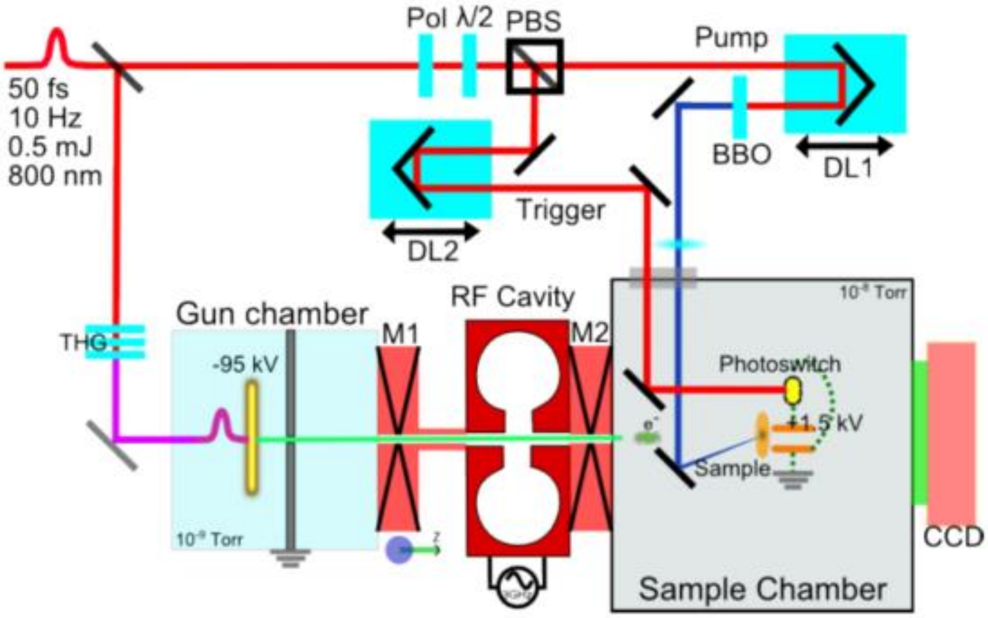

Figure 3.6: Schematic of the experimental setup of time stamping experiment. The electron pulses generated on the photocathode (z = 0 cm) are accelerated 95 keV toward the anode (z =1 cm). After first magnetic lens (M1, z = 9 cm), RF cavity (z = 39 cm), and second magnetic lens (M2, z = 45 cm), the electron pulses are focused at the sample (z = 59 cm). The electron pulses pass through a pair of streak plates (z = 60 cm) with time-resolved high voltage. In the end, the electron diffraction patterns are collected by the CCD detector (z = 85cm). Reprinted with permission from [46] ©2013 American Institute of Physics.

When the timing of the pump laser and the probe electron pulses are perfectly synchronized, the streaked electron pulses are still in the original unstreaked position because there is no voltage on the streak plates at the first zero-crossing of oscillation. If the timing of the pump laser and the probe electron pulses changes because of the timing jitter, the drift in timing can be detected by tracing the displacement of electron pulses on the CCD screen.

In Figure 3.8a, five different traces collected over 15 hours (3 hours each) show clear short-term timing shift of the short-term and long-term jitter of the temperature drift. In Figure 3.8b, we re-bin all the five traces according to their real time points based on the streak velocity and their displacement on the CCD screen. It is easy to see a great improvement in signal-to-noise ratio and resolution of the time constant of the fast lattice-heating dynamics of Si.

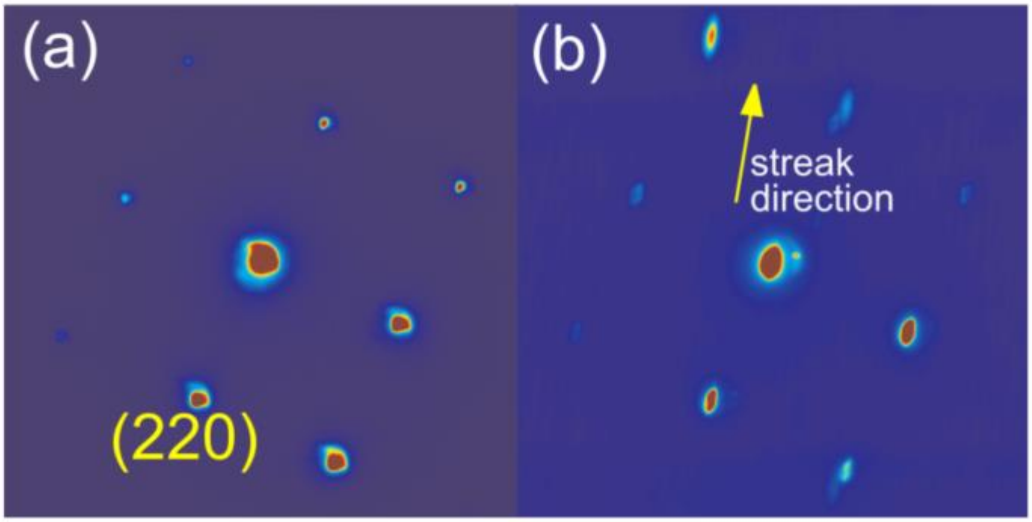

Figure 3.7: Comparison of the streaked and unstreaked diffraction patterns of a Si (001) single crystal. (a) an unstreaked diffraction pattern. (b) the same sample but with the streak camera turned on. Reprinted with permission from [46]. ©2013 American Institute of Physics.

The time-stamping technique can overcome both short-term and long-term timing jitter. However, this technique has its own limitations in FED experiments. The problem of time-stamping method is that the streak plates on the streak camera block electrons scattered at higher angles from reaching the detector. For the streak camera with smaller gap, up to 2/3 of the detector area receives no electrons. These higher diffraction orders contain important information, which is lost. The streak camera must be placed after the sample, because the timing jitter of pump laser and probe electron will introduce change in the incident electron pulse angle which makes data analysis much harder. In order to have a high enough streak velocity, the gap width between two streak plates is only 300 μm, which is too small for most diffracted electrons to pass through the streak plates. On the CCD screen, only Bragg peak (000) and some low order Bragg peaks can be collected, offered limited structural information. If the sample is simple inorganic crystals with high symmetry such as (001) Si, low-order Bragg peaks may offer enough structural change information to understand its ultrafast dynamics. However, for organic samples with complex structures, only these few Bragg peaks are not enough to obtain a full molecular movie.

Second, the streak plates on the streak camera decrease the brightness of the electron diffraction peaks not blocked by the streak camera. For organic compounds, which mostly contains light atoms, the intensity of these Bragg peaks is not high and the ultrafast changes in diffraction intensity are too small. Additional dimming of the Bragg peak intensities caused by time stamp technique makes the study of ultrafast dynamics in organic compounds even more difficult.

Beside all these drawbacks, time-stamping technique allow us to directly track the time of arrival of each electron pulse and correct for the timing jitter down to 30 fs RMS with minimal distortion to the diffraction patterns. Furthermore, the time-stamping technique helps us to correct the laser-electron time zero easily which makes data collection very efficient. It is not necessary to use additional data analysis to reject “bad” scans and correct time zero shift for every scan.

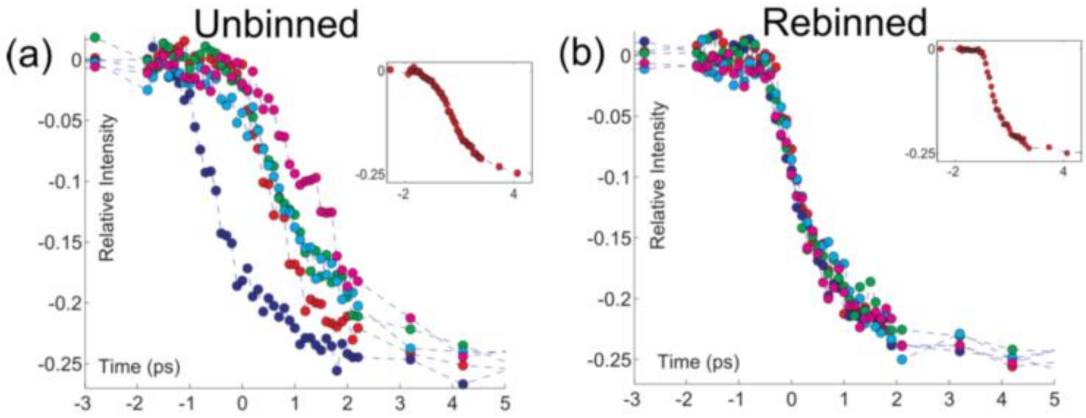

Figure 3.8: FED results with time-stamping. (a) Five traces were taken in 3 hours, showing the time zero shift during the experiment. (b) The same data but with correction of arrival time obtained by the time-stamping. The insets show the average traces in (a) and (b) respectively. Reprinted with permission from [58] ©2013 American Institute of Physics.

3.3.2 Time-stamping of accumulated electron pulses

Although short collection scans and traces recombination based on the time-zero shift of every scan can correct the arrival time drift in the experiment, the data collection is very inefficient. For some ultrafast dynamics with small signals, obvious time-zero determination of time-dependent traces is not possible [52,58]. A simple average of time traces from the original data would have worse time resolution (see Figure 3.8). Therefore, in FED experiments without time-stamping, the laser-electron time-zero must be tuned once every hour to make sure it hasn't drifted too far. Data scans should be finished in around one hour. In the data analysis, every time-dependent trace must be checked carefully to reject "bad" scans. In order to recombine data from different scans with different arrival time shifts, the laser-electron time-zero (the time point when the ultrafast signal starts) must be obtained by fitting [52,58]. Here, we use the time-stamping technique to track the arrival time of every 50 shots, so we can overcome the long-term arrival time shift problem while we still have enough signal-to-noise ratio within a reasonable experiment time. We perform this experiment to confirm that our hybrid DC-RF FED system has enough time resolution to study sub-picosecond dynamics, although it suffers from time-zero shift because of temperature drifts.

The experimental setup is similar to Figure 3.6. A 800 nm laser was used to pump the sample. We accumulated 50 electron pulses in one electron diffraction pattern. One of those 50 electron pulses was streaked by the streak camera to track the arrival time of the electron pulses at that time point. The remaining 49 electron pulses were used to study the ultrafast dynamics of the sample $[Fe(PM\text{-}AzA)_2](NCS)_2$. The one streaked electron pulse cannot represent the arrival time of all 50 electron pulses because of short-term timing jitter (~200 fs RMS (see Figure 3.3b), but its arrival time helps us to track the slow long-term time-zero shift (1.2 ps in 3 hours) (see Figure 3.11).

At first, we measure the contribution of timing jitter to the pulse duration of accumulated electron pulses. In Figure 3.9, it is clear that the contribution of timing jitter reaches maximum after 5 accumulated electron pulses. Although the pulse duration of one single electron pulse is better (~230 fs), the pulse duration of 50 accumulated electron pulses is good enough (~325 fs). Therefore, even though we didn't apply single shot time-stamping technology in this experiment, the time resolution is still good enough to track the ultrafast SCO dynamics in single crystal $[Fe(PM\text{-}AzA)_2](NCS)_2$.

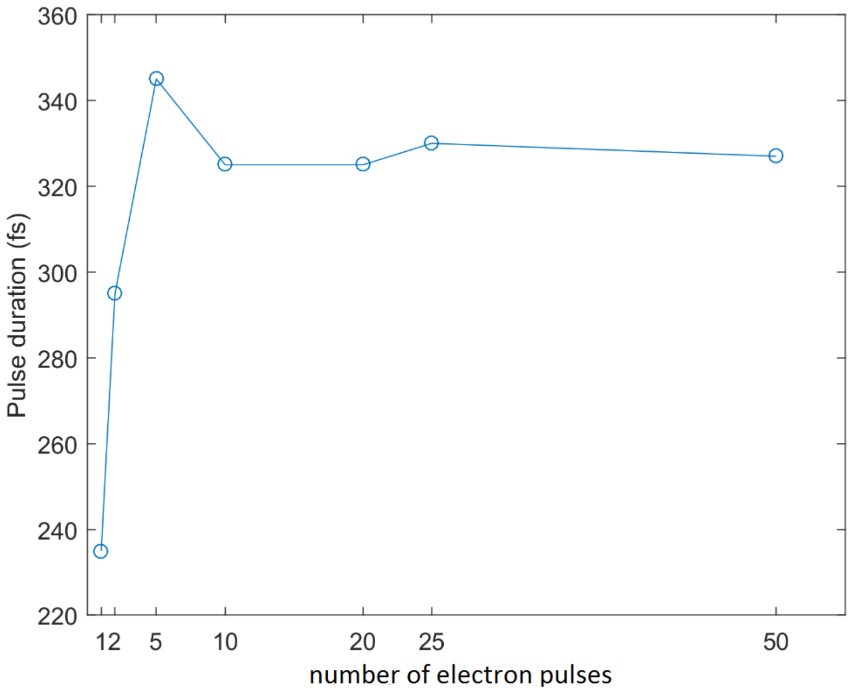

Figure 3.9: Averaged pulse duration vs. number of accumulated electron pulses. The timing jitter from RF cavity increases the pulse duration of accumulated electron pulses, but the contributions from timing jitter reaches maximum after 5 accumulated electron pulses. The electron number was 64,000 per electron pulse and the streak velocity was 60 pixel/ps for this measurement.

Figure 3.10 is a standard electron diffraction pattern in the time-stamping measurement of the accumulated of electron pulses. This electron diffraction pattern was accumulated over fifty electron pulses, and one of these fifty electron pulses was streaked by the streak camera. The delay of trigger laser was tuned to move streaked electron pulse away from most Bragg peaks of electron patterns. At the start of every time trace scan, the original streaked electron pulse position which presents the arrival time of electron pulses was recorded. Then, the time-zero shift in the whole scan could be tracked by measuring the displacement of streaked electron pulse. On the other hand, the quality of electron diffraction pattern was worse than regular electron pattern, since almost 2/3 of electron diffraction pattern was cut over by streak plates. Although some high order Bragg peaks can still be found, the signal-to-noise ratio of them is not good enough for this technique to be applied for the study of ultrafast dynamics.

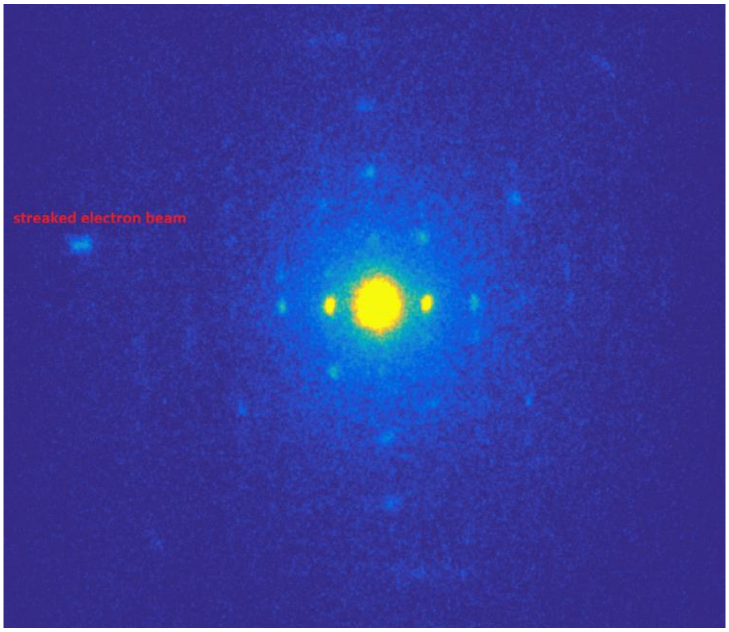

Figure 3.10: Electron diffraction pattern with streaked electron pulse. One electron diffraction pattern is accumulated by fifty electron pulses, and one of these fifty electron pulses is streaked by streak camera to track time-zero shift.

In Figure 3.11, we select 18 hours of experiment to present the arrival time shift of electron pulses in the experiment. In the middle of the experiment, we adjust the arrival time of electron pulses back to 0 ps by tuning the delay of trigger laser for streak camera when the arrival time drifts too much. We notice in Figure 3.11 that it is impossible to anticipate the shift of electron pulse arrival time, since many reasons can change the arrival time of electron pulses. These include the temperature changes in the lab and the temperature variations from the chillers of the RF cavity and the PLL.

In Figure 3.12, we present results of the time-stamping method as applied to overcome the long-term arrival time shifts in $[Fe(PM\text{-}AzA)_2](NCS)_2$ experiment (see Chapter 6 for more details) Figure 3.12(a) shows the time trace analyzed by compact FED data analysis method. We check every individual time trace to reject “bad” data and rebinned based on different arrival time shift. In Figure 3.12b, for the same electron diffraction data, we re-bin the time traces based on the arrival time shift obtained from time-stamping data. The time step from -2 ps to 5 ps is 200 fs, and only the data in this area is applied to generate the time-stamping. Then, we fit an exponential function for both time traces, and the fitted time constant is 3.2 ps and 2.9 ps, respectively. Although time-stamping method is applied to overcome arrival time shift in long-term, the signal-to-noise ratio and time constant of both time traces are still similar.

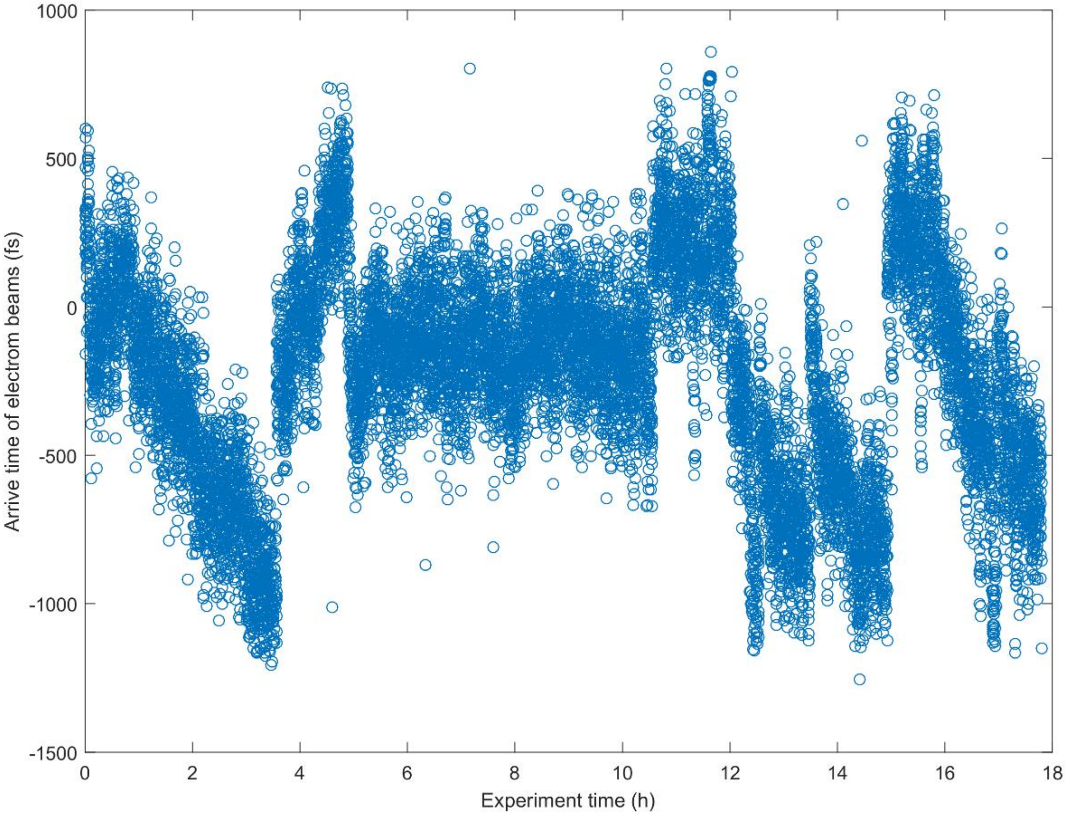

Figure 3.11: Arrival time shift of accumulated electron pulses vs. experimental time. The time-stamping method is used to measure the arrival time of each 50 electron pulses. We adjusted the arrival time of the electron pulses in the middle of the experiment to make sure it hasn't drifted too far.

In Figure 3.11, the pulse duration of accumulated 50 electron pulses is ~300 fs. This pulse duration includes the short-term timing jitter. To correct arrival time shift of electron pulses, we tried both the typical data analysis method and the time-stamping method. They show similar signal-to-noise ratio and time constant. Therefore, there is no doubt that time resolution of our DC-RF FED system is good enough to probe ultrafast dynamics. On the other hand, Figure 3.12 supports the suggestion we made in the study of [Fe(PM-AzA)$_2$](NCS)$_2$ that the time constant of ultrafast structure change in [Fe(PM-AzA)$_2$](NCS)$_2$ is ~ 2.3 ps. This observation of longer time constant structural change than that of other studies is not caused by the time-zero shift in long-term or our data analysis method.

Unbinned

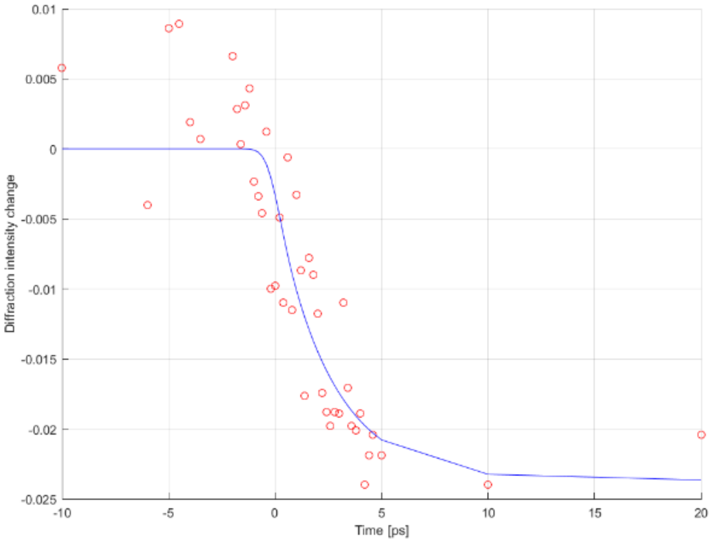

Rebinned

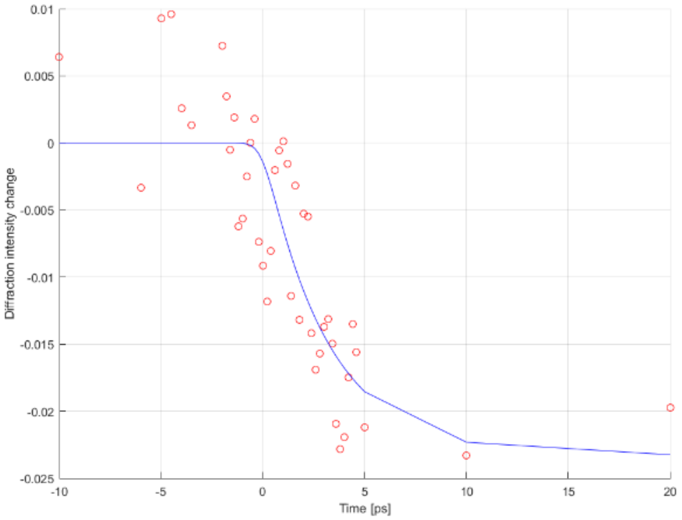

Figure 3.12: Result of time-stamping method for long-term arrival time shift. The [Fe(PM-AzA)$_2$](NCS)$_2$ sample is pumped with same experimental conditions as in optical pump-probe experiments and other FED measurements. The ultrafast changes in diffraction intensity of (110) Bragg peak is plotted as a function of time. The overall experiment time is 18 hours divided over 13 individual scans. (a) The time trace is analyzed by checking every individual time trace to reject "bad" data and rebinning based on different arrival time shift. (b) The same data corrected by the long-term arrival time shift. The time step from -2 ps to 5 ps is 200 fs, and only the data in this area is applied to generate the time-stamping.

3.4 Summary

A photo-triggered streak camera has been used to measure the pulse duration of electron pulses and perform time-stamping technique to correct timing jitter in our hybrid DC-RF electron source down to 30 fs RMS [58]. The typical pulse duration of the electron pulses is ~300 fs FWHM with an areal density of 0.92 electron per μm^2. We measured the short-term timing jitter to be 200 fs RMS and the pulse duration of single electron pulse to be 178 fs RMS. The photo-triggered streak camera has the ability to easily measure the temporal resolution before every pump probe experiment to make sure the system has both high brightness and sub picosecond temporal resolution. We used time-stamping technique to study the ultrafast lattice heating dynamics of single crystal Si [58] and ultrafast spin crossover of single crystal $[Fe(PM\text{-}AzA)_2](NCS)_2$ to present the principle and performance of this technique in FED experiment, especially the improvement on temporal resolution.

For simple inorganic compounds with high symmetry, by applying time-stamping technique on every electron pulse, both short-term and long-term timing jitter can be corrected to improve the temporal resolution of the hybrid DC-RF electron source down to around 200 fs RMS (the pulse duration of single electron pulse) [58]. However, for complicated organic compounds, this technique has its own limitations such as cutting diffraction pattern and reducing diffraction intensity, but it can still correct long-term timing jitter caused by the temperature drift in the experiment.

Chapter 4

Electron Diffraction Theory and Time-resolved Crystallography

As mentioned in Chapter 1, the electron diffraction has atomic spatial resolution to track structure change in many ultrafast dynamics. X-ray and electron diffraction crystallography is developed based on the pioneer contributions of M.V. Laue, W.H. Bragg, and W.L. Bragg [36]. In this Chapter, fundamentals of electron crystallography are introduced first, including Bragg's law, Ewald sphere, Zones, and structure factor. Furthermore, the time-resolved crystallography used widely in FED data analysis is discussed for further discussion of FED experimental results in Chapter 6, including structure refinement method.

4.1 Fundamentals of electron crystallography

Because of the wave particle duality of electrons [36], the wavelength and the frequency can be related with the energy and the momentum of the particle by the de Broglie equation:

$$\lambda = \frac{h}{p} = \frac{h}{mv} \tag{4.1}$$

where *h* is the Planck constant, *p* is the relativistic momentum of the electron, *m* is the mass of the electron and *v* is the electron velocity. When electrons are accelerated by an electric potential, the kinetic energy of the electron is given by:

$$E = eV = \frac{m_0 v^2}{2} \tag{4.2}$$

where *e* is the elementary charge and m_0 is the rest mass of the electron. The wavelength of the electron is then given by:

$$\lambda = \frac{h}{\sqrt{2m_0 ev}} \tag{4.3}$$

In most FED studies, the accelerating voltage is higher than 50 kV, so the velocity of the electrons can be more than 33% of the speed of light. Therefore, the wavelength of the electron need to corrected for relativistic effects:

$$\lambda = \frac{h}{\sqrt{2em_0 V(1+\frac{eV}{2m_0 c^2})}} \tag{4.4}$$

where *c* is the speed of light.

Table 4.1: Accelerating voltage vs. electron wavelength (with relativistic corrections)

V_{acc} (kV)	100	200	300	400	1000
Wavelength (Å)	0.037	0.0251	0.0197	0.0164	0.0087
Velocity (10^8 m/s)	1.64	2.09	2.33	2.48	2.82

In our hybrid DC-RF electron source, for an accelerating voltage of 95 kV, the wavelength of electron is 0.0381Å.

4.1.1 Bragg’s law

Electrons have the properties of waves and particles. When electron waves pass through a crystal, electron waves are scattered by atoms in the crystal. Because of the long-range order of the crystal, constructive interference of the scattered electron waves occurs at specific angles where all the scattered electron waves are in phase, resulting in an electron diffraction pattern on the camera screen.

In Figure 4.1, monochromatic electron waves are incident on two identical atomic planes with interplanar spacing d. The scattering angle of atomic planes is θ. The path difference of the two scattered waves is $2d\sin\theta$. A and B are the two incident beams with same wavelength and phases, and A1 and B1 are the two scattered beams. If the path differences of the scattered wave of the first plane (OA1) and the scattered wave of the second plane (RB1) is the sum of SR and RT, the path difference (δ) equals $2d\sin\theta$.

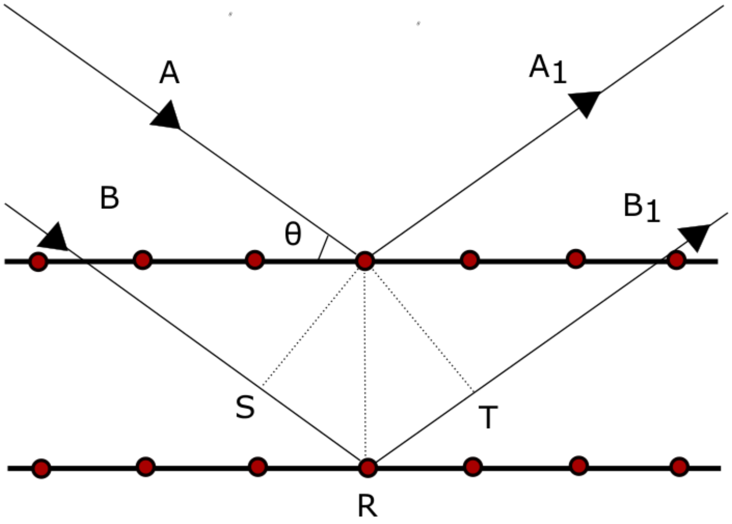

Figure 4.1: Bragg’s law. The incident angle of electron beam and scatter angle of atomic planes is θ. The path difference (SR+RT) of the two scattered waves is $2d\sin\theta$. A and B are the two incident beams with same wavelength and phases, and A1 and B1 are the two scattered beams.

The condition of constructive interference for the two waves is that the path difference is an integer number of the wavelength. Therefore, Bragg's law is given by:

$$2d\sin\theta = \mathrm{n}\lambda \tag{4.5}$$

where d is the interplanar spacing, θ is the scattering angle, n is an integer number and λ is the wavelength. The Bragg's law determines the geometric condition for diffraction peaks to occur in a diffraction pattern. If the Bragg condition are satisfied by the interplanar spacing d and the scattering angle θ, Bragg peaks will occur in the diffraction pattern:

$$2\frac{d_{hkl}}{n}sin\theta = \lambda \tag{4.6}$$

According to the definition of Miller indices,

$$2\frac{d_{hkl}}{n}sin\theta = 2d_{nh.nk.nl}sin\theta = \lambda \tag{4.7}$$

n is the diffraction order of a set of parallel planes (Bragg planes) (*hkl*), so the nth order diffraction of Bragg planes (*hkl*) equals to the first order diffraction of Bragg planes (*nh,nk,nl*). Therefore, n can be taken as n=1 in a simplified Bragg's law,

$$2dsin\theta = \lambda \tag{4.8}$$

The accelerating voltage in FED and TEM is about 100-200 kV, so the wavelength of the electrons is ~10^{-3} nm. The interplanar spacing in common crystals is ~10^{-1} nm. Under the Bragg condition, the scattering angle is ~1°. Therefore, the crystal planes which can generate Bragg diffraction are almost parallel to the incident electron beams.

4.1.2 Ewald sphere

Bragg's law can be written as:

$$sin\theta = \frac{\frac{1}{d}}{\frac{2}{\lambda}} \tag{4.9}$$

The electron scattering geometry of an electron beam with wavelength (λ) and a crystal interplanar distance (d) can be visualized using the concept of the Ewald sphere. In Figure 4.2, the crystal is placed in the center position of the Ewald sphere (O_1). AO_1 is the direction of the incident electron beam. When AO_1 passes through the crystal at O1, some electrons transmit through the crystal and end up at O while other electrons are scattered by the Bragg plane (hkl) in the direction of O_1G. g is reciprocal lattice vector, g=OG=1/d_{hkl}, AO=2/ λ, $\angle$OAG=θ.

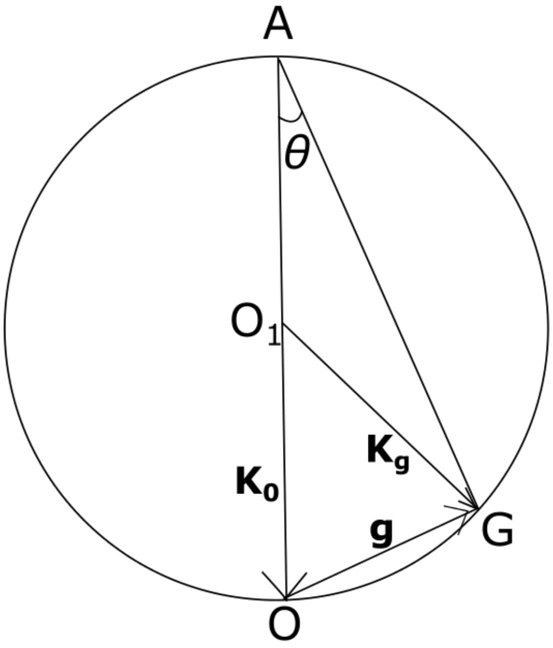

Figure 4.2: 2D representation of Ewald sphere. AO_1 is the direction of the incident electron beam. Sample is placed at O_1. O is the end of transmitted electron beams, and G is the end of scattered electron beams. $\mathbf{K_0}$ and $\mathbf{K_g}$ are incident and scattered vectors, respectively. **g** is the reciprocal lattice vector.

The incident wavevector $\boldsymbol{K_0}$ and scattered wavevector $\boldsymbol{K_g}$ have same length of 1/ λ, because of elastic scattering. Their directions represent the direction of the incident electron beam and the scattered electron beam, respectively. $\boldsymbol{g}$ is the reciprocal lattice vector of Bragg planes (*hkl*), so the Bragg's law is given by:

$$|g_{hkl}| = |K_s - K_0| = \frac{1}{d_{hkl}} = 2\frac{1}{\lambda}sin\theta \quad (4.10)$$

Therefore, we get from equation (4.10):

$$2d_{hkl}\sin\theta = \lambda \tag{4.11}$$

4.1.3 Zones and zone axis

In crystallography, zone refers a set of planes whose intersection lines are all parallel to each other, and zone axis refers the intersection line. Zone axis can be presented by [*uvw*] in crystallography. Therefore, the reciprocal lattice zone is perpendicular to the zone axis [*uvw*], and the reciprocal plane (*uvw)** is orthogonal to zone axis [*uvw*].

The Zone axis is described by $\boldsymbol{r} = ua+vb+wc$ and the set of Bragg planes (*hkl*) is described by reciprocal vector $\boldsymbol{g}_{hkl}=ha^*+kb^*+lc^*$. Because the reciprocal lattice zone is perpendicular to the zone axis [*uvw*], **r*****G** is given by:

$$hu+kv+lw=0 \tag{4.12}$$

This equation 4.12 called Weiss zone law is useful in data analysis of electron diffraction. (*uvw*)* is the reciprocal plane which is orthogonal to zone axis [*uvw*]. Therefore, all reciprocal points (*hkl*) of [*uvw*] zones are on reciprocal plane (*uvw*)*. According to Weiss zone law, if (h_1, k_1, l_1) and (h_2, k_2, l_2) are two Bragg planes of [*uvw*] zones,

$$h_1u+k_1v+l_1w=0 \tag{4.13}$$

$$h_2u+k_2v+l_2w=0 \tag{4.14}$$

Therefore, the zone axis [*uvw*] can be given by:

$$u = \begin{vmatrix} k_1 & l_1 \\ k_2 & l_2 \end{vmatrix}, v = \begin{vmatrix} l_1 & h_1 \\ l_2 & h_2 \end{vmatrix}, w = \begin{vmatrix} h_1 & k_1 \\ h_2 & k_2 \end{vmatrix} \tag{4.15}$$

One Bragg plane (*hkl*) in real space can be described by a reciprocal point *hkl* in reciprocal plane, and one zone [*uvw*] in real space can be described by a reciprocal plane (*uvw*)* (see Figure 4.3).

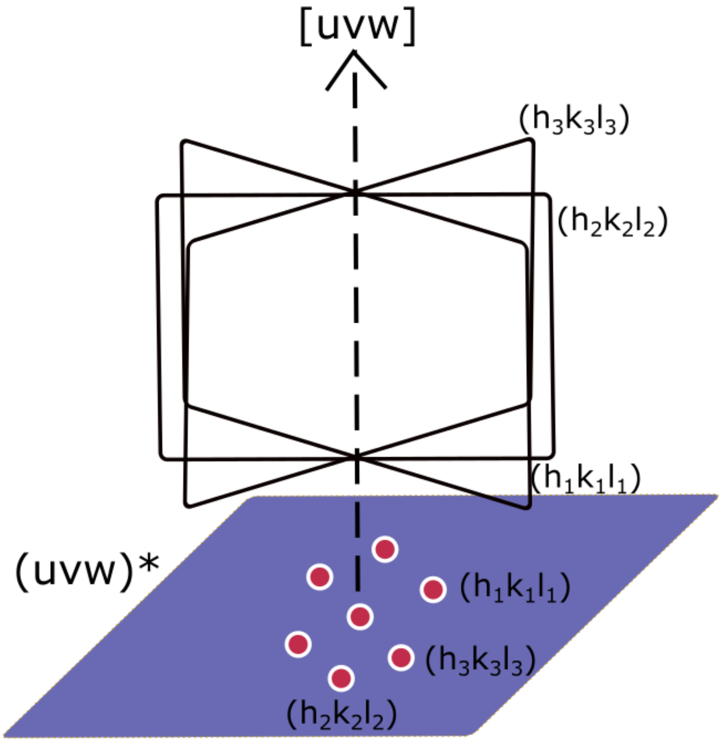

Figure 4.3: zone and zone axis in real space and reciprocal space.

4.2 Structure factor calculation and diffraction intensity

The position of points in the reciprocal lattice depends on the geometry of the crystal, but the Bragg spots in the electron diffraction have different shape and intensity containing the information about the content of the unit cell. We introduce the concept of structure factor to present the relationship between reciprocal lattice and Bragg peaks. Many references in this section is from Zhou [36].

The structure factor is the most important quantity for structure in electron diffraction data analysis, because the square of the structure factors $|F|^2$ are proportional to the diffraction intensity of the Bragg peaks.

$$I \propto |F^2| \tag{4.16}$$

Therefore, the structure factors link the points in reciprocal lattice to the Bragg peaks in diffraction pattern, and points in reciprocal lattice have more structural information such as size, shape and intensity.

The structure factors depend on crystal structure: the type of atoms present and their location. The structure factor of a Bragg plane is defined as:

$$\mathrm{F}(\boldsymbol{u}) = \sum_{j=1}^{N} f_j(\boldsymbol{u}) \cdot exp2\pi i(\boldsymbol{u} \cdot \boldsymbol{r}_j) \tag{4.17}$$

$$\boldsymbol{u} \cdot \boldsymbol{r} = (h\boldsymbol{a}^{*}+k\boldsymbol{b}^{*}+l\boldsymbol{c}^{*}) \cdot (x\boldsymbol{a} + y\boldsymbol{b} + z\boldsymbol{c}) = (hx + ky + lz) \tag{4.18}$$

where $f_j(\boldsymbol{u})$ is the atomic scattering factor. The structure factor can be complex and is written in terms of its amplitude and phase component:

$$F(\boldsymbol{u}) = |F(\boldsymbol{u})| \exp(i\varphi_f(\boldsymbol{u})) \tag{4.19}$$

where φ_f is the phase of the structure factor.

In an electron diffraction experiment, only the amplitudes $|F(hkl)|$ can be obtained from the electron diffraction patterns, not the phases, so it is impossible to obtain the molecular structure from the electron diffraction patterns only. The structure factor phases are the quantities that determine the relative position of the atoms in the unit cell, known as the phase problem of crystallography. However, if the molecular structure of initial and final states are known from other studies such as X-ray diffraction, the electron diffraction patterns can be simulated by calculating the structure factors mentioned above.

4.3 Electron diffraction patterns of thin polycrystalline and amorphous films

When monochromatic electron waves pass through a crystal, the electrons are scattered by the constituent atoms. The constructive interference of the electrons waves generates Bragg peaks on the camera screen. For thin samples (thickness of less than 100 nm), assuming negligible absorption of the incident radiation and single elastic scattering, the amplitude of the N scattered wavelets is given by [37]

$$A(s) = \sum_{n} f_n \exp(-2\pi i s \cdot r_n) \tag{4.20}$$

$$s = 2\sin(\theta)/\lambda \tag{4.21}$$

where s is the scattering vector, f_n is the scattering factor, r_n is the position of N atoms, θ is incident angle of electron beams, and λ is the wavelength of the incident electron beams. In an electron diffraction experiment, the observed quantity is the intensity of Bragg peaks $I(s)$:

$$I(s) = |A(s)|^2 = \sum_{n} \sum_{n'}^{n} f_n f_{n'} \exp\left[-2\pi i s \cdot (r_n - r_{n'})\right] \tag{4.22}$$

If $n \neq n'$, $I(s)$ can be written because of conjugate terms,

$$\begin{aligned} & f_n f_{n'} \exp\left[-2\pi i s \cdot (r_n - r_{n'})\right] + f_n f_{n'} \exp\left[-2\pi i s \cdot (r_n - r_{n'})\right] \\ &= f_n f_{n'} (\cos[2\pi s \cdot (r_n - r_{n'})] + \cos[2\pi s \cdot (r_{n'} - r_n)] \end{aligned} \tag{4.23}$$

Defining $r_{nn'}$ as the vector from atom n to atom n',

$$I(s) = \sum_{n} f_n^2 + \sum_{n} \sum_{n \neq n'} f_n f_{n'} \cos(2\pi s \cdot r_{nn'}) \tag{4.24}$$

4.4 Structure refinement method

We apply structure refinement method to obtain intermediate structures from observed changes of diffraction patterns from FED experiment in previous studies [50,51]. Spin crossover dynamics of single crystal $[Fe(PM\text{-}AzA)_2](NCS)_2$ will be analyzed by this structure refinement method in Chapter 6. In Figure 4.4, because of the phase problem of crystallography, the intermediate structure (f) can not be obtained from the observed diffraction pattern changes from FED experiment (e). However, the initial structure and final structure of sample molecule (a) are generally known by other studies such as X-ray diffraction and theoretical calculations, and even the ultrafast intermediate structure of some reactions can be simulated based on theory and other supplementary experiments. Therefore, an assumed intermediate structure (b) can be built by a model with several free parameters based on the structures of the initial and final states. Then, the differential diffraction pattern (c) can be simulated using the structure factors calculation from the initial structure and the intermediate structure of the sample molecule. An order parameter (d) is applied to determine the difference between simulated structure change and observed one. After many repetitions over steps (b), (c), (d), the free parameters are optimized and a solution intermediate structure is then found.

The order parameter we applied in our structure refinement is the Pearson correlation coefficient: $\gamma(F_1, F_2)$ [50]:

$$\gamma_p(F_1, F_2) = \frac{\sum_k c_1(k) c_2(k)}{\sqrt{\sum_k c_1(k)^2}\sqrt{\sum_k c_2(k)^2}} \tag{4.25}$$

$$c_i(k) = \frac{F_i(k) - \overline{F_\iota}}{\overline{F_\iota}} \tag{4.26}$$

$$\overline{F_\iota} = \frac{\sum_k F_i(k)}{N} \tag{4.27}$$

where F_1 and F_2 are the experimental structure factors and the calculated structure factors, respectively. The value of $\gamma(F_1, F_2)$ varies from -1 (perfect anti-correlation), to 0 (no correlation), to +1 (perfect correlation).

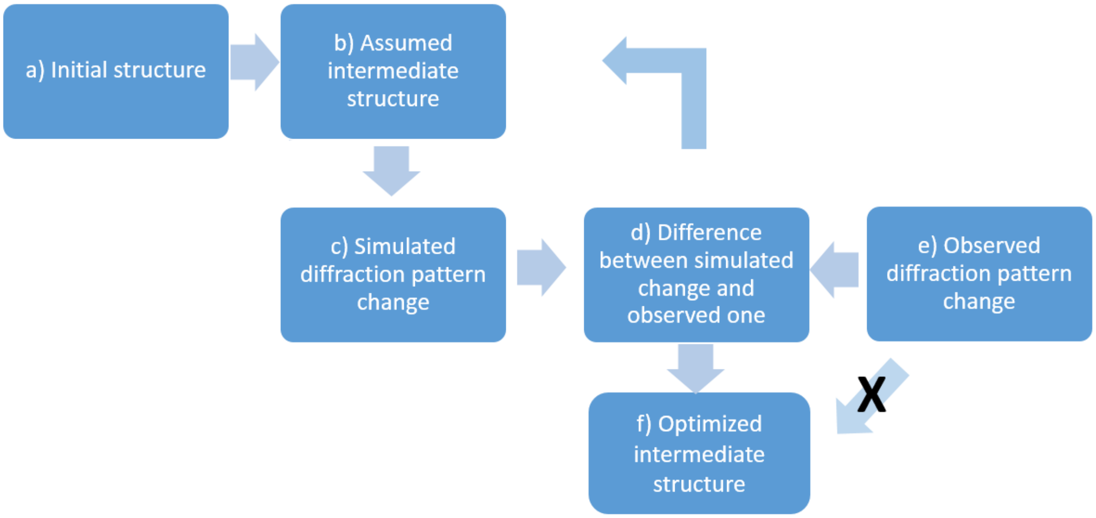

Figure 4.4: The structure refinement algorithm. (a) The initial structure is known from other studies as starting point. (b) The initial structure is modified to obtain initial intermediate structure. (c) The relative diffraction pattern changes can be simulated by the structure factors calculation. (d) An order parameter is applied to determine the difference between the simulated change from (c) and the observed one from (e). If the error is above a threshold, then the process goes back to (b) to alter the initial intermediate structure. This process is repeated for many times until an optimized intermediate structure is obtained. (e) The observed diffraction pattern change can be obtained from the FED experiment by calculating $(\mathbf{I}_{\text{pump-on}}\text{-}\mathbf{I}_{\text{pump-off}})/\mathbf{I}_{\text{pump-off}}$. (f) The optimized intermediate structure is obtained by repeating steps (b) – (d).

4.5 The advantages of electron diffraction over X-ray diffraction

X-ray diffraction and electron diffraction are widely used to determine the crystal structures with sub-Å spatial resolution [36]. In femtochemistry, ultrafast electron diffraction (UED) and ultrafast X-ray diffraction (UXD) are developed as ultrafast structural probes. The principle of these two diffraction techniques is similar, and they are considered as both competitive and complementary techniques. In certain fields of study, electron diffraction has some advantages over X-ray diffraction. First, electrons are scattered more strongly by crystals than X-rays. The electrons interact with the Coulomb potential of the nuclei and the bound electrons of the atoms, while the X-rays are scattered by the electric dipole of the atoms. Furthermore, the damage introduced by electrons is much smaller. X-rays at high energy can damage the crystals in one shot [20,21]. Therefore, most UXD experiments need to change samples for every shot, while the samples in UED show no noticeably damage despite long exposure of the electrons. Finally, UED setups are much less expensive and smaller than UEX setups. The cost of a tabletop scale UED devices is under € 1 million, and two doctoral students can operate and maintain it easily. However, the new generations of UXD such as X-ray Free Electron Lasers (XFELs) and Linac Coherent Light Source (LCLS) requires > € 1 billion budget and hundreds of senior scientists and engineers.

Chapter 5

Spin Crossover

In this chapter, the background of SCO dynamics is introduced first. Then, time-resolved studies are discussed to investigate the photoinduced SCO dynamics, including time-resolved X-ray absorption near edge spectra (XANES) and UV-Vis spectroscopy studies. Furthermore, studies of single crystal $[Fe(PM\text{-}AzA)_2](NCS)_2$, a classic model system of the SCO dynamics, are summarized for further discussions in Chapter 6. In the following thesis, explanations and theories of the SCO dynamics are about the iron(II) metal center compounds. This chapter has many references from Hauser [6].

5.1 Ligand field theory

The discovery of the phenomenon was almost simultaneously to the formulation of the ligand field theory [71]. With the development of the ligand field theory, the SCO dynamics has been explained by *Van Vleck and Ewald et al.* [72,73].

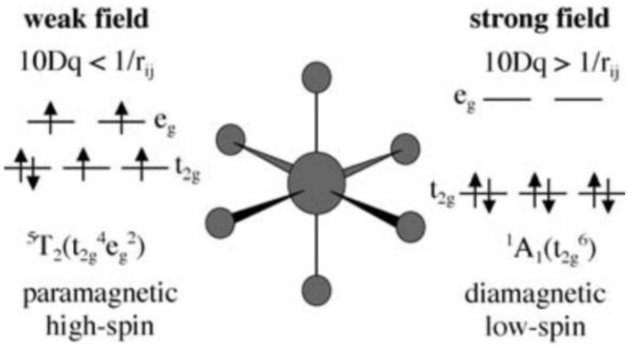

Figure 5.1: The electronic configurations of the LS and the HS states in the iron(II) octahedral complex. In this figure,10Dq is the ligand field strength, and r_{ij} is the distance between the metal center and the ligand. Reprinted with permission from [6] ©2004 Springer-Verlag Berlin Heidelberg.

Figure 5.1 is a classic iron(II) FeN_6 octahedral coordination [6]. $^1A_1$ and $^5T_2$ are Mulliken symbols which represent the symmetric information of electronic states. In Figure 5.1, *t* refers to triply degenerate levels orbitals while *g* refers to “gerade” (even) the orbitals which have the same symmetry with respect to the inversion center. On the other hand, *e* refers doubly degenerate orbitals. Five d orbitals from iron(II) atoms are split into a subset of three non-bonding orbitals, d_{xy}, d_{yz} and d_{zx} (t_{2g}) and a subset of two anti-bonding orbitals, d_{z2} and d_{x2-y2}(e_g). The t_{2g} orbitals are non-bonding and the e_g orbitals are anti-bonding, so t_{2g} orbitals are at lower energy than the e_g orbitals. The splitting between these two sets of orbitals is called ligand field strength. The electronic configurations of the LS and the HS states depend on the competition between the ligand field strength, 10Dq and the spin pairing energy $\prod$. If the ligand field strength is larger than the spin pairing energy, the six electrons in the d orbitals will pair up in the t2g orbitals as $^1A_1(t_{2g}{}^6)$. Otherwise, the six d electrons will follow the Hund’s rule to occupy all five d orbitals as $^5T_2(t_{2g}{}^4e_g{}^2)$. In both thermal and photoinduced SCO dynamics, the LS $^1A_1(t_{2g}{}^6)$ ground states transfer to the HS $^5T_2(t_{2g}{}^4e_g{}^2)$ excited states by 2 paired electrons in the t_{2g} sublevel entering the e_g sublevel as unpaired electrons.

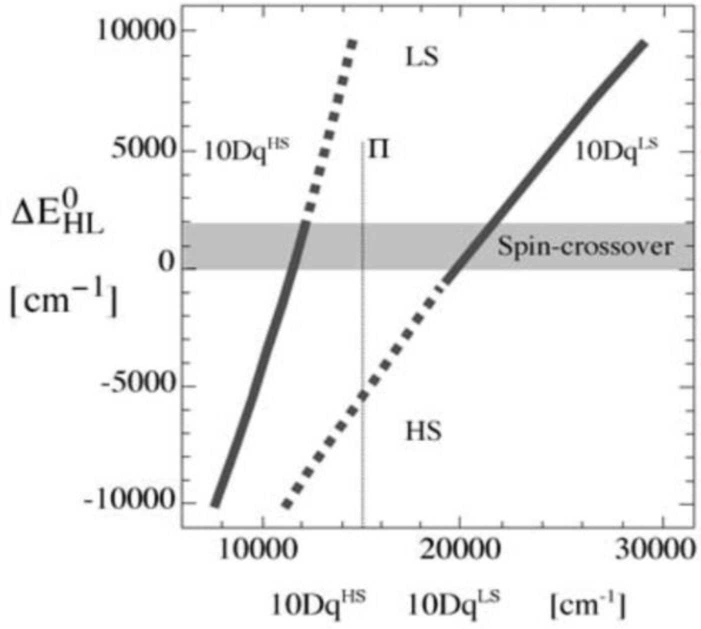

Figure 5.2 Regions of stability of either one or the other spin state as a function of the ligand field strength. The region of spin crossover compounds is indicated by the shaded area. Reprinted with permission from [6] ©2004 Springer-Verlag Berlin Heidelberg.

Whether one compound can have thermal SCO depends on the competition between the zero-point energy difference and the ligand field strength. In Figure 5.2, the zero-point energy difference(ΔE^0_{HL}) between the HS state and the LS state can be presented as a function of $10Dq^{HS}$ and $10Dq^{LS}$. If $10Dq^{HS}$<10,000 cm^{-1}, ΔE^0_{HL}<0, the high spin state is the thermodynamically stable state. On the other hand, if $10Dq^{LS}$>23,000 cm^{-1}, ΔE^0_{HL}>2,000 cm^{-1}, the low spin state is the thermodynamically stable state. Only the narrow range of the shaded area ($10Dq^{LS}$≈11,000-12,500 cm^{-1}, $10Dq^{HS}$≈19,000-22,000 cm^{-1} and ΔE^0_{HL}≈0-2000 cm^{-1}) has thermal SCO dynamics.

5.2 Thermal spin crossover

In the thermal SCO dynamics, if the zero-point energy difference(ΔE^0_{HL}) between two potential energy wells of the HS state and the LS state is comparable to the thermally accessible energies (k_BT), a thermal SCO between the HS state and the LS state is possible. (see Figure 5.3)

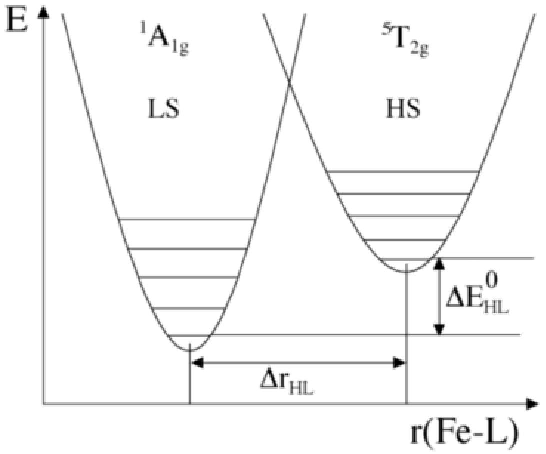

Figure 5.3 Potentials for the HS and LS are plotted with Fe-L which is considered as the most structural change in thermal SCO. In the figure, L is the ligand and r_{HL} is the difference of iron-ligand bond between the LS state and the HS state. Reprinted with permission from [6] ©2004 Springer-Verlag Berlin Heidelberg.

In the SCO dynamics from the LS state to the HS state, the relative occupancies of the d orbitals changes from $^1A_1(t_{2g}{}^6)$ to $^5T_2(t_{2g}{}^4e_g{}^2)$, so the HS state has two unpaired electrons in the anti-bonding eg orbitals. After SCO from the LS state to the HS state, two paired electrons from the t_{2g} orbital enter e_g orbital as unpaired electrons, so the banding energy of the metal center and the ligand is weaker and there are unpaired electrons in the HS state. Therefore, the two most important consequences of a SCO transition are changes in the metal ligand atom distance (the Fe-N bond distance in most iron(II) compounds) and changes in the magnetic properties [6].

5.3 Characterization of spin states

In present study, the SCO dynamics can be monitored by several different techniques from different parameters of the SCO compounds, such as the metal ligand bond elongation, the magnetic changes and the change of electron configuration of the metal center. The most common method to monitor the SCO is the measurement of the magnetic susceptibility, because this measurement can direct probe the changes of the magnetic properties [6]. However, the limited time resolution of the magnetic susceptibility method makes this method more useful in the study of thermal SCO instead of the photoinduced SCO dynamics. With the development of the femtosecond laser and the time resulted X-ray technology, optical spectroscopies and XANES offer indirect probes to study the ultrafast photoinduced SCO dynamics with femtosecond time resolution.

The typical probe to study the SCO compounds is the measurement of the magnetic susceptibility as a function of temperature. (in Figure 5.4 (a)) SQUID (superconducting quantum interference device) magnetometers are generally applied for their higher sensitivity and accuracy rather than other types of magnetometers [75,76]. In present studies, the XANES [20-26] (in Figure 5.4b) and the optical spectroscopies [11-19] (in Figure 5.4 (c)) are also employed generally to track the change of the spin state as a function of temperature.

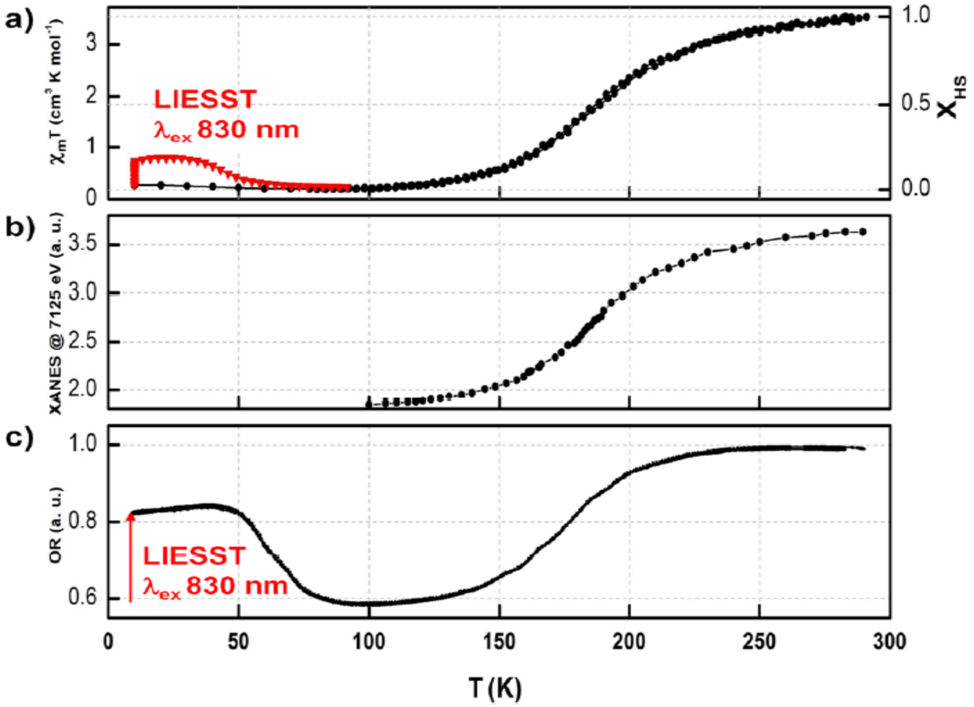

Figure. 5.4: Temperature dependence of (a) χ_M.T (b)XANES (c) optical reflectivity for spin crossover of the $[Fe(PM\text{-}AzA)_2](NCS)_2$. Reprinted with permission from [21] ©2015 Prof. Eric Collet

Figure 5.4 is the magnetic susceptibility of a classic iron(II) SCO compound $[Fe(PM\text{-}AzA)_2](NCS)_2$ [21]. In this figure, χ_M.T is determined by the temperature dependent contributions χ_{HS} and χ_{LS} according to equation 5.1, while χ_{HS} and χ_{LS} are the mole fraction of the HS state and the LS state, respectively.

$$\chi(\mathrm{T}) = X_{HS}\chi_{HS} + (1 - X_{HS})\chi_{LS} \tag{5.1}$$

It shows $[Fe(PM\text{-}AzA)_2](NCS)_2$ crystals undergo a smooth isostructural spin crossover with $T_{\frac{1}{2}}$=184K, a typical of non cooperative systems. The degree of cooperativity depends on the effects of the spin changes which are propagated throughout the solid and determined by the lattice properties.

5.4 Time-resolved XANES studies on photoinduced SCO dynamics

Time-resolved X-ray methods has been used to investigate the photoinduced SCO dynamics of the Fe(II) metal compounds with the development of ultrafast X-ray laser pulses from X-ray free electron lasers (XFEL), including X-ray absorption [24,77], emission [22], and diffraction [79,80]. Among those time-resolved X-ray methods, the XANES [20,21,25,81] is generally applied to study multiple Fe(II) sample systems to probe the SCO dynamics with femtosecond time resolution. The features of given samples in the X-ray absorption spectra (XAS) are from the photo-absorption cross section from an atomic core level to final states. The features in the energy region above the ionization energy "edges" are called XANES, and the region at higher energy is called extended X-ray absorption fine structure (EXAFS). Since XANES is reported [20,21,25,81] to be sensitive to both structural and electronic changes in a selected target atom (the core Fe(II) atom in our Fe(II) SCO studies), the photoinduced SCO dynamics can be monitored by tracing the time-resolved changes of the features in the XAS.

$Fe(phen)_2(NCS)_2$, an Fe(II) SCO compound, has been extensively studied by various time-resolved techniques [20,81]. Figure 5.5 is an XANES experimental spectra of Fe(phen)2(NCS)2 compounds at the Fe K edge at temperatures below and above the spin transition temperature [81]. It has many obvious changes in absorption of XANES between the LS and the HS states during the spin switch by thermal SCO. In an XANES experimental spectra, one of the most important features is that the intensity of the shoulder labeled A in the "edge" (7125 eV) reduces to the intensity of the shoulder labeled A'. Another important feature is that a new shoulder labeled C' (7133 eV) appears. For those changes of the resonances (A, B), *Briois et al.* [81] explained these changes by a transition toward antibonding states that results from hybridization between N(2p) and Fe(4s, 4p) orbitals. When the Fe-N bond distance is reduced, the enhanced hybridization introduces both the energy shift of the edge and the change of the resonance intensity. Furthermore, there is a large bump labeled X (7170 eV). According to *Briois et al.*, X and X' energies is related by Natoli's well-known rule [81]:

$$Ed^2 = cste \tag{5.2}$$

where E is the resonance energy; $cste$ is a constant; d is the mean distance of the Fe-N bond. *Cammarata et al.* [20] further suggest that the changes of these features mainly result from the Fe-N bond elongation and they are important fingerprints of the SCO based on this study.

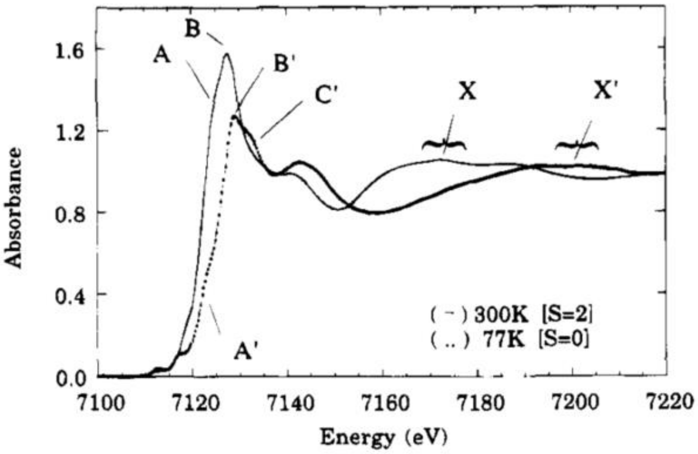

Figure 5.5: XANES experimental spectra of the SCO transition $Fe(phen)_2(NCS)_2$ compounds at the Fe(II) K edge. Reprinted with permission from [81] ©1995 American Chemical Society.

Time-resolved XANES has been applied to study the SCO dynamics on single crystal samples. In 2014, *Cammarata et al.* [20] studied the time-resolved SCO dynamics of single crystal $Fe(phen)_2(NCS)_2$ by both the femtosecond optical spectroscopy and XANES. They believe the changes of the XAS features is related to the Fe-N bond elongation. The energy shift in the rising edge (in Figure 5.6(a)) is introduced by an increase in the energy of the anti-bonding MOs because of shorter Fe-N bond lengths. Furthermore, the energy shift also has the contribution from the p-orbitals to the bonding MOs. The time constant of those features in Figure 5.6b is 170(10) fs fitted with a single-exponential function of the rising edge. Furthermore, the absorption changes in Figure 5.6 are reported to be due to the changes in the Fe-N bond lengths according to SCO theory studies and XANES simulations [24,77,81]. In the end, they suggest that there is a fast inter system crossing driving a Fe-N bond elongation followed by an additional bending phonons in the SCO dynamics of $Fe(phen)_2(NCS)_2$ based on their experimental observations.

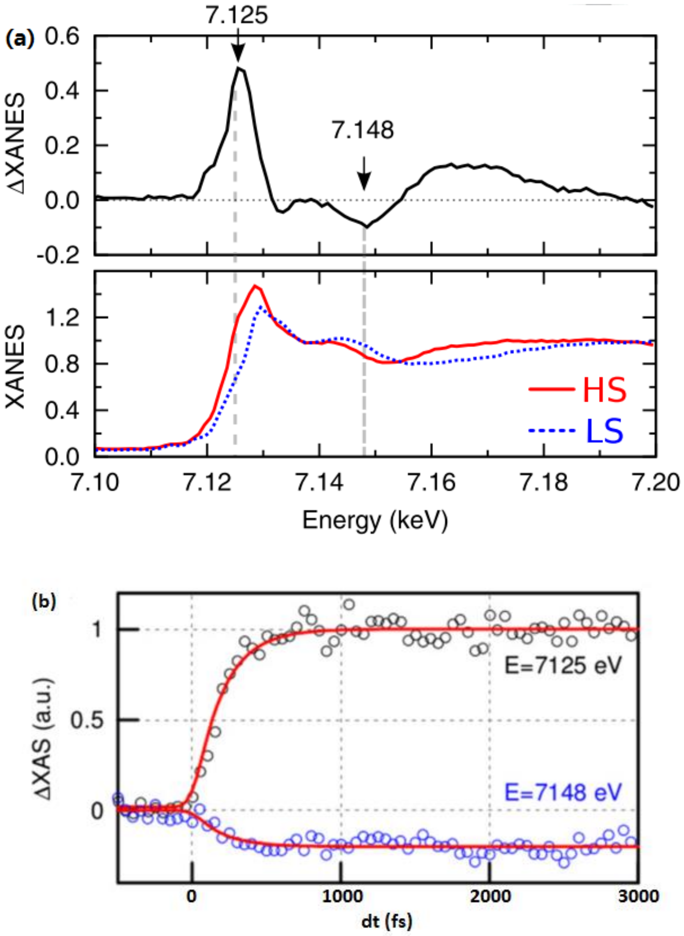

Figure 5.6: (a) XANES spectra and difference ΔXANES measured between the LS and HS states (b) Time-resolved traces of XANES at 7125 and 7148 eV Reprinted with permission from [20] ©2014 American Physical Society

The SCO dynamics in liquid have been studied by the XANES. In 2009, *Bressler et al.* [20] employed XANES to study the SCO dynamics of $[Fe^{II}(bpy)_3]^{2+}$ in solution. A simulation of XANES spectrum to show a nearly linear relationship between the Fe-N bond distance and the intensity of the B-feature in the rising edge. Therefore, they also believe the B-feature intensity in the rising edge of XAMES is a signature of the Fe-N bond elongation [20,77].

5.5 Time-resolved UV-Vis spectroscopy studies on photoinduced SCO

The SCO dynamics have been studied by the time-resolved UV-Vis spectroscopy as well [11-19]. Most of studies published in recent years reported similar spectroscopic observables of the photocycle leading to the SCO transition, but the timescale of the decay from the metal ligand charge transfer (MLCT) state into the HS state reported is instrument response limited in most studies, such as X-ray absorption [20,21,25], ultraviolet absorption [82], Raman emission [14]. *Auböck et al.* [11] claimed the temporal resolution of the experiment is the key issue of the time constants debate, and they reported the decay rate of the MLCT state into the HS state is <50 fs by their improved time resolution experimental setup. They summarised the timescales of the electronic states in the SCO dynamics [11]. At first, the SCO process is believed to occur in a much shorter than 150 fs timescale. Then, the SCO from the MLCT manifold to the HS state is reported to be finished in <50 fs, and the lifetime of the MLCT state is more than 20 fs [25,83] and close to 50 fs [19]. Furthermore, a vibrational cooling of the molecule on timescales of 1.1 and 3.4 ps is observed. This is the reported interpretation [11].

5.6 SCO studies on single crystal $[Fe(PM\text{-}AzA)_2](NCS)_2$

In this section, the background information of single crystal $[Fe(PM\text{-}AzA)_2](NCS)_2$ is discussed. The ultrafast SCO dynamics of single crystal $[Fe(PM\text{-}AzA)_2](NCS)_2$ is also discussed, which based on the present time-resolved studies, including the femtosecond optical reflectivity [19,21] and XANES [21].

5.6.1 Overview of $[Fe(PM\text{-}AzA)_2](NCS)_2$

Létard. J. F et al. [84] measured the magnetic susceptibility of this single crystal $[Fe(PM\text{-}AzA)_2](NCS)_2$ (Cis-bis(thiocyanato)-bis(N-2′-pyridyl methylene)-4-(phenylazo) aniline iron(II)) by both Faraday-type magnetometer and SQUID magnetometer. Figure 5.7 shows single crystal of $[Fe(PM\text{-}AzA)_2](NCS)_2$ has a gradual spin state change from a mainly HS state above 295 K to a mainly LS state below 110K, and it undergoes a smooth spin crossover with $T_{\frac{1}{2}}$=184K, a typical of non cooperative system [19].

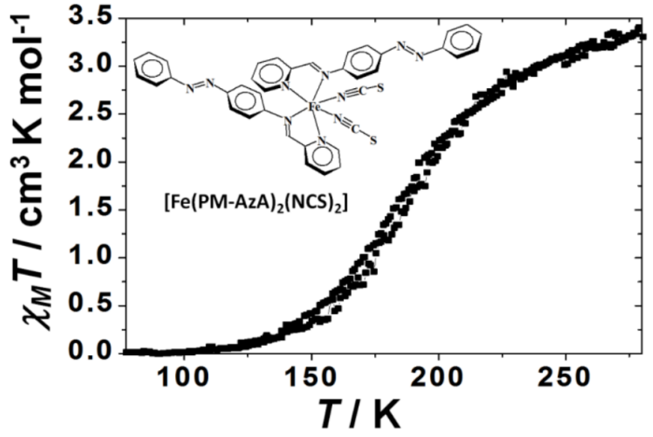

Figure 5.7: Structure of $[Fe(PM\text{-}AzA)_2](NCS)_2$ and thermal SCO characterized by magnetic susceptibility Reprinted with permission from [19] ©2013 Elsevier Ltd.

X-ray diffraction was applied to obtain single crystal structure of the Fe(II) spin crossover (SCO) compound $[Fe(PM\text{-}AzA)_2](NCS)$ by *Guioneau et al* [85]. Crystal information files of both states are downloaded from CCDC (Cambridge Crystallographic Data Centre). Some key crystal information is summarized in Table 5.1, including three unit cell edge lengths (a, b and c) and three internal angles (α, β and γ). The LS and the HS structures were collected at 110K and 295K, respectively.

From the LS state to the HS state, the crystal system and the space group are still same, so there is no appearance or disappearance of Bragg peaks during the SCO process. The structural motions in the local FeN_6 octahedron are the elongation of six Fe-N bonds and the distortion of the N-Fe-N angles. The average Fe-N bond distance increases ~0.2 Å form the LS to the HS which is considered as a key structure signature of the SCO process in the

FeN_6 environment. The expansion of the unit cell during the thermal SCO is not homogeneous, while the Fe atom fraction position in the unit cell changes as well. Specially the change along c axis is bigger than a and b axis's. Therefore, in the electron diffraction experiment, a shift of diffraction peaks especially those peaks ($h=k=0$, $l\neq0$) indicts the unit cell expansion in the $[Fe(PM\text{-}AzA)_2](NCS)_2$ SCO process.

Table 5.1: Single crystal information of $[Fe(PM\text{-}AzA)_2](NCS)_2$ at different temperature [93]

Temperature (K)	110K	295K
Crystal system	Monoclinic	Monoclinic
Space group	P 21/c	P 21/c
a (Å)	15.038	15.155
b (Å)	14.396	14.623
c (Å)	16.677	17.068
α (deg)	90	90
β (deg)	92.84	92.95
γ (deg)	90	90
V (Å^3)	3605.92	3777.45
Fe-N bond (Å)	1.97	2.16
Fe atom fraction	(0.291 0.284 0.068)	(0.292 0.287 0.055)

$[Fe(PM\text{-}AzA)_2](NCS)_2$ is a classic system of the Fe(II) d^6 electronic configuration [21,84]. Figure 5.8 shows the SCO phase transition of single crystalline $[Fe(PM\text{-}AzA)_2](NCS)_2$ and the Fe atoms in both the LS and the HS molecules are fixed to compare the structure change in the local FeN_6 environment. The energy of Fe-N coordination bond is smaller in the HS state, because two electrons are pormoted to the antibonding e_g orbital and loss of pi-backbonding from the t_{2g}. Therefore, the Fe-N bond distance in the HS state is elongated by ~0.2 Å.

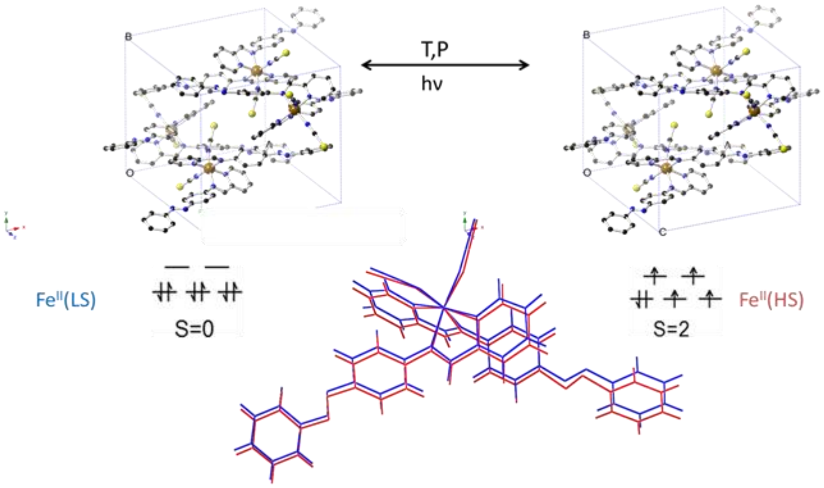

Figure 5.8: Spin crossover phase transition from LS state to HS state. [Fe(PM-AzA)$_2$](NCS)$_2$ has both the thermal and the photoinduce SCO. Fe atoms in both the LS and the HS molecules are fixed to compare the structure change in the local FeN$_6$ environment.

5.6.2 Time-resolved optical reflectivity studies of [Fe(PM-AzA)$_2$](NCS)$_2$

The SCO dynamics can be monitored by optical pump probe measurements, because the color of SCO compounds changes during the SCO [10]. The optical reflectivity is generally applied to study the ultrafast SCO dynamics, because the optical density of ~100 μm thick [Fe(PM-AzA)$_2$](NCS)$_2$ is too high to allow transmission measurements [19,21].

In Figure 5.9(a), the thermal SCO of the [Fe(PM-AzA)$_2$](NCS)$_2$ crystals have been monitored by the optical reflectively measurement to show the change of the optical reflectivity between the LS state and the HS state [66]. A isosbestic point at ~690 nm with two distinct regions is considered as the optical fingerprint of the [Fe(PM-AzA)$_2$](NCS)$_2$ SCO dynamics. Therefore, in the optical pump probe experiment, 640 nm, 690 nm and 720 nm are chosen as probe wavelengths to track those optical fingerprints.

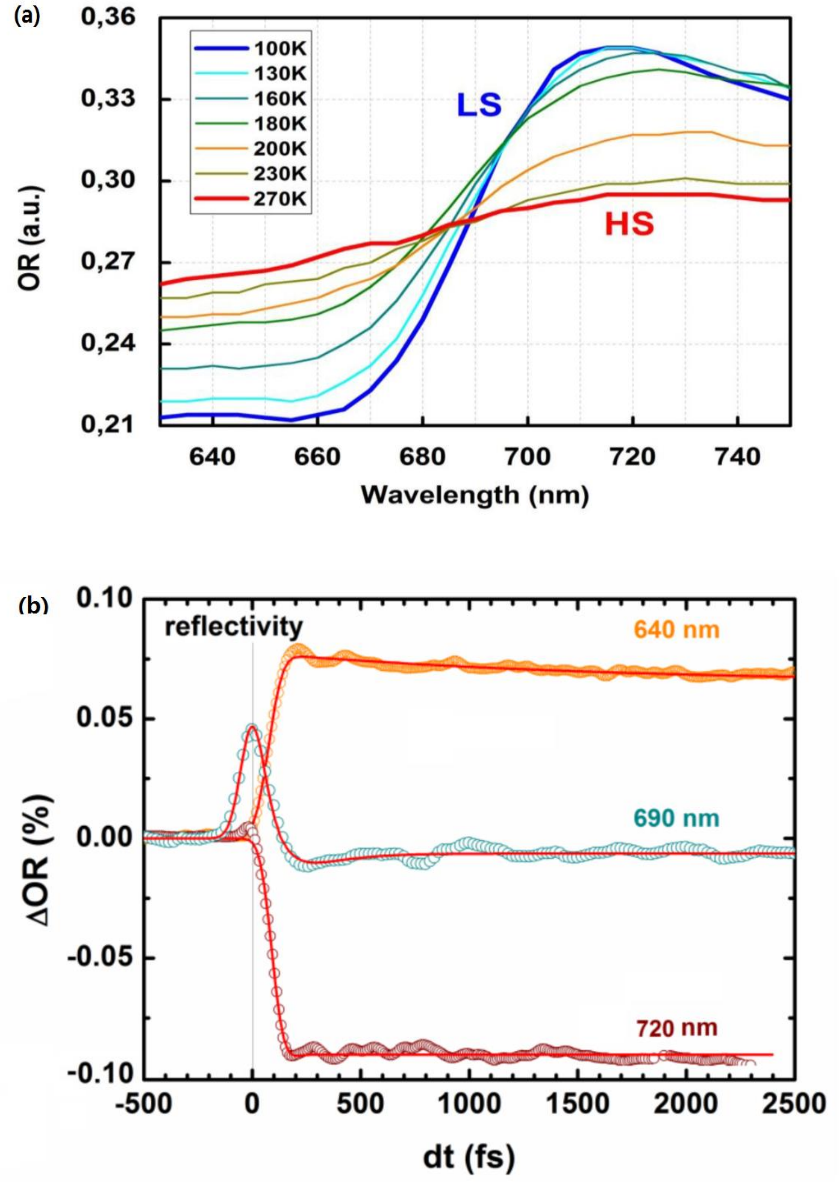

Figure 5.9: (a) Change of $[Fe(PM\text{-}AzA)_2](NCS)_2$ optical reflectivity spectra at different temperature. (b) Ultrafast SCO dynamics was trackd by optical pump probe experiment. An 850 nm laser was used to trigger the photoinduce SCO. The probe wavelengths are set to be at 640 nm, 690 nm and 720 nm which are considered as optical fingerprints of the $[Fe(PM\text{-}AzA)_2](NCS)_2$ SCO dynamics. Reprinted with permission from [21] ©2015 Prof. Eric Collet

In order to track the ultrafast SCO dynamics in single crystal $[Fe(PM\text{-}AzA)_2](NCS)_2$, the time resolution is critical for the experiment. For the pump-probe experiment, pump and probe lasers are two ultrafast laser pulses with ~40 fs each [19]. Overall instrumental response function (IRF) is on the order of ~80 fs. In Figure 5.9b, the time traces obtained by three different probe wavelengths 640 nm, 690 nm and 720 nm show an ultrafast OR increase at 640 nm and decrease at 720 nm. The step function of the OR changes at 640 nm and 720 nm and the fitting of the Gaussian shape transient peaks observed at 690 nm shows that the experimental time resolution is not high enough to track the SCO dynamics. Therefore, the time constant of SCO dynamics from the LS state to the HS state can only be estimated to be less than 50 fs [21].

Furthermore, Figure 5.10 reports a time constant on the order of 1-2 ps after the photoexcitation at 660 nm and 635 nm probe wavelength [19]. This slower time constant compared to sub 50 fs SCO dynamics is believed as a non radiative vibrational relaxation in the HS potential called vibrational cooling [19,21]. The excess energy deposited on the molecule from pump laser (~1.46 eV) has no time to dissipate in sub 50 fs SCO dynamics. Therefore, they reported that the highly vibrational excited state of the HS state relaxes to the bottom of the HS potential well in a time scale of 1-2 ps.

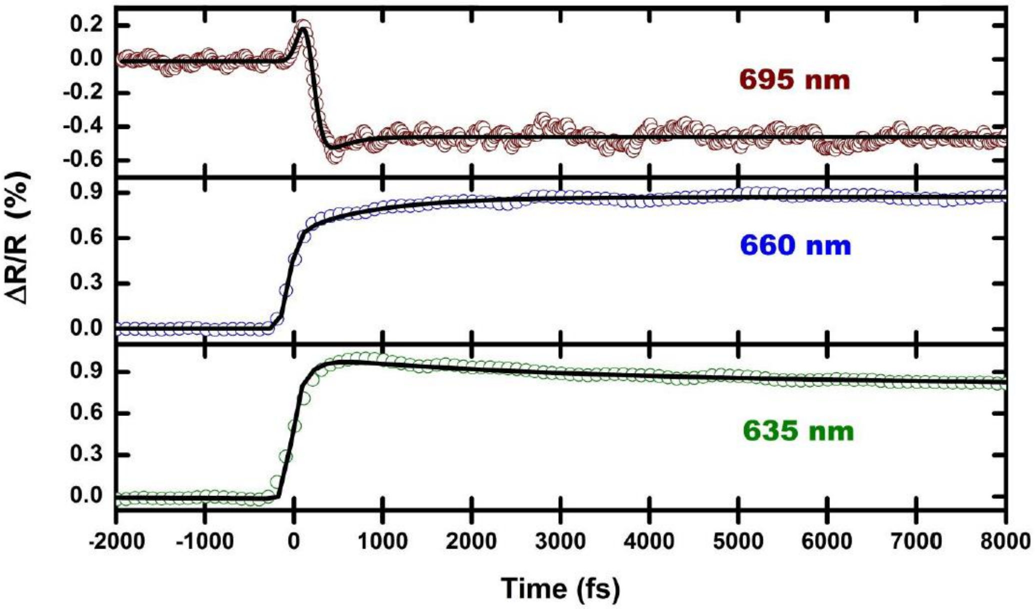

Figure 5.10: Longer time scale of optical pump probe experiment. The probes at 660 nm and 635 nm show a fast increase with sub 50 fs time constant and a slow vibrational cooling in 1-2 ps time constant. Reprinted with permission from [19] ©2013 Elsevier Ltd.

5.6.3 Time-resolved XANES studies of $[Fe(PM\text{-}AzA)_2](NCS)_2$

The time-resolved XANES [21] was also applied to study the SCO dynamics of single crystal $[Fe(PM\text{-}AzA)_2](NCS)_2$, because the optical pump probe experiment is only sensitive at electronic configuration changes in the SCO dynamics. XANES has been reported to have the ability of monitoring the dynamics of the Fe-N bond elongation with the accuracy of 100 fs [20]. Figure 5.11 is the time trace of the XANES signal of single crystal $[Fe(PM\text{-}AzA)_2](NCS)_2$ [21]. The sample is pumped by 50 fs FWHM laser pulses to trigger the SCO dynamics and probed by 30 fs X-ray pulses at of 7125 eV which has the biggest difference of absorption between the LS state and the HS state. The time constant of XANES increase is 160 (20) fs with the 110 (10) fs FWHM IRF. This time constant is believed to be the time for the molecule to elongate the Fe-N bonds after the photoinduced SCO, because the SCO from the LS state to the HS state decrease the Fe-N bond energy by two electrons from non-bonding orbitals entering anti-bonding orbits as unpaired electrons.

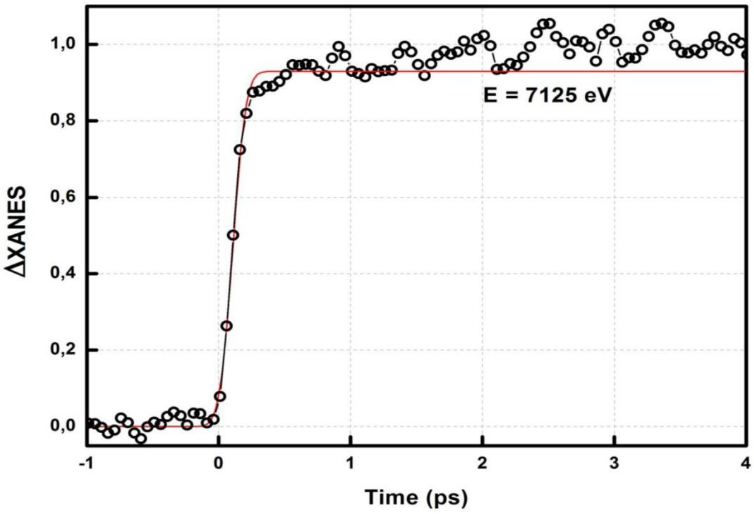

Figure 5.11: SCO dynamics $[Fe(PM\text{-}AzA)_2](NCS)_2$ of is monitored by XANES at the Fe K-edge after 850 nm wavelength pump laser. The increase of XANES with a time constant of 160 fs is believed to be the signature of the Fe-N bond elongation characteristic in SCO. Reprinted with permission from [21] ©2015 Prof. Eric Collet.

The observations from the ultrafast optical pump probe and the time-resolved XANES measurements are summarized in Figure 5.12 [21]. After a photoexcitation by a pump laser at 850 nm, the HS state is speculated to be reached in 50 fs through several intermediate states. The Fe-N bond elongation occurs with a time constant of 160 fs as the result of two electrons from the non-bonding orbitals being promoted to the anti-bonding orbitals as unpaired electrons in the SCO dynamics. The highly vibrational excited state of the HS state relaxes to the bottom of the HS potential in a time scale of 1-2 ps.

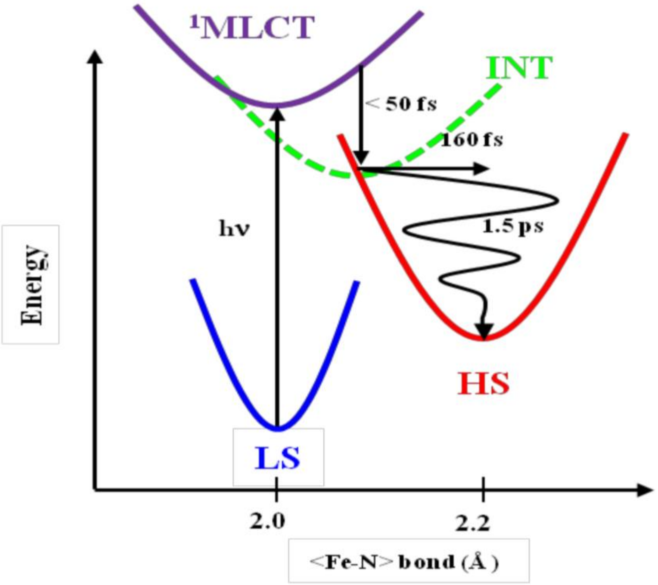

Figure 5.12: Schematic summary of the ultrafast photoinduce SCO dynamics of [Fe(PM-AzA)$_2$](NCS)$_2$ based on the observations from ultrafast optical pump probe and time-resolved XANES measurements. After photoexcitation, the excited HS state is reached in time constant of sub 50 fs. The Fe-N bond elongation occurs with a time constant of 160 fs. Reprinted with permission from [21] ©2015 Prof. Eric Collet.

5.7 Summary

In this chapter, the SCO dynamics are discussed with details including thermal SCO and photoinduced SCO. Basically, the phenomenon of SCO is a property due to the interplay between the ligand field strength and the electron-electron repulsion. The photoinduced SCO dynamics have been studied by XANES, transient absorption and reflection spectroscopies. Most of studies published in recent years reported similar spectroscopic observables of the photoinduced SCO transitions. One important consequence of the SCO is changes in the metal-donor atom distance. This metal-donor bond elongation is considered as the signature of the SCO dynamics. One key issue is that metal-donor bond elongation is reported to be directly correlated in time (150 fs) to the electronic state dynamics. Although multiple methods have been used to study the photoinduced SCO dynamics, they are more sensitive to changes in the electronic state rather than atomic motions. In Chapter 6, I will report the studies on the photoinduced SCO by FED, a direct probe of structure changes, with atomic spatial resolution and femtosecond temporal resolution.

Chapter 6

FED study on single crystal $[Fe(PM–AzA)_2](NCS)_2$

In this Chapter, I will discuss the study of the photoinduced SCO dynamics in single crystal $[Fe(PM–AzA)_2](NCS)_2$ by our ultrabright DC-RF hybrid femtosecond electron source. As mentioned in Chapter 5, the photoinduced SCO dynamics in single crystal $[Fe(PM–AzA)_2](NCS)_2$ have been investigated by XANES and optical reflectivity studies[66,91]. *Marino et al*. [21] suggest that the SCO dynamics of single crystalline $[Fe(PM-AzA)_2](NCS)_2$ electronic state is a two-step process with a fast sub-150 fs relaxation of short-lived intermediate states (INT), following with a slow 1.6 ps vibrational cooling of the photoinduced high spin state (see Figure 6.1).

The key issue is that recent time-resolved studies [20-26] reported that the Fe-N bond elongation was coupled to the electronic spin transition which in turn was correlated in time (150 fs) to the excited state dynamics as observed by changes in spectral signatures. They suggested that the excitation is to an antibonding state, which should instantly result in a repulsive force on the Fe and N atoms, and atoms separate along the bond direction. The problem is to identify uniquely which change in absorption and electronic surface is related to the spin transition and bond elongation. Although various measurements have been used to study the SCO dynamics, optical pump probe studies are more sensitive to changes in the electronic state rather than atomic displacements.

Here we provide a direct measurement of the Fe-N bond distance which has been uniquely calibrated by exploiting the thermal cycling of the high spin and low spin states of spin cross over systems. We definitely show the structural change of Fe and N atoms and electronic state change in Fe are concomitant but not simultaneous. The Fe–N bond elongation, compared to other ligand motions in SCO, is not a conclusive signature of SCO, and it is coupled to the other ligand motion in phase transition. The time scale of the Fe–N bond elongation is significantly slower than the Fe(II) electronic state dynamics.

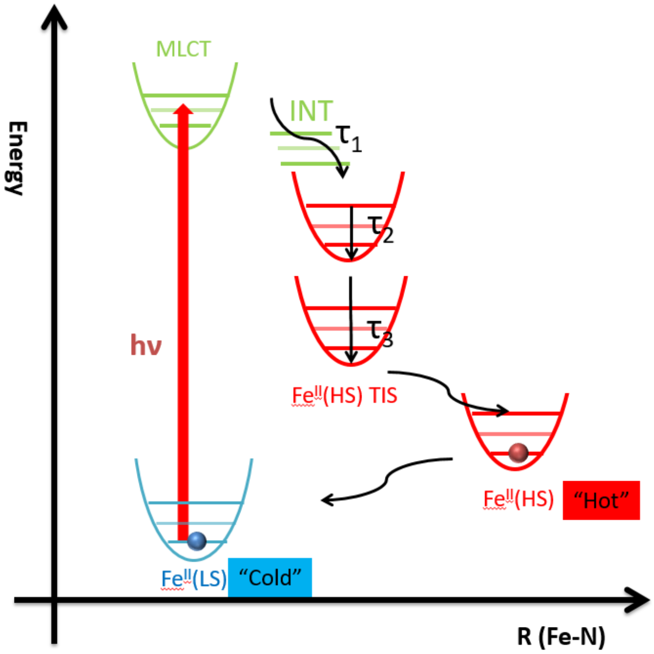

Figure 6.1 Schematic pathway of photoinduced SCO based on present works

6.1 FED experimental conditions

6.1.1 Excitation conditions

The femtosecond electron diffraction experiment has similar excitation conditions of optical pump-probe reflectivity studies [19,21]. Samples are mounted on TEM grid, and the equilibrium temperature is measured to be 170 K. At this temperature, 25 % of molecules in the crystal are at the high spin state and 75 % of molecules are at the low spin state.

60fs FWHM laser pulses, centered at 800 nm are used as the pump. Optical reflectively study [19] reported that single crystal $[Fe(PM\text{-}AzA)_2](NCS)_2$ need ~1 ms to recover from the HS excited state to the LS ground state, so the repetition rate of this pump-probe experiment is 100 Hz to make sure the excited molecule has recovered to the ground state before the next pump laser. The excitation fluence is 1.28 mJ/cm^2, and there is no damage from heat accumulations during the experiment.

Ultrabright femtosecond electron pulses [49,50], generated by a 95 keV hybrid DC-RF electron source, are used as the structure probe to track the ultrafast structure dynamics in the SCO. Figure 6.2 is the schematic diagram of the FED setup at the University of Toronto. The ultrabright femtosecond electron pulses have 5.3×10^4 electrons per pulse with a spot size of (275±20) µm diameter (0.86 $e^-/\mu m^2$), a repetition rate of 100 Hz and 0.5 % electron shot to shot intensity stability.

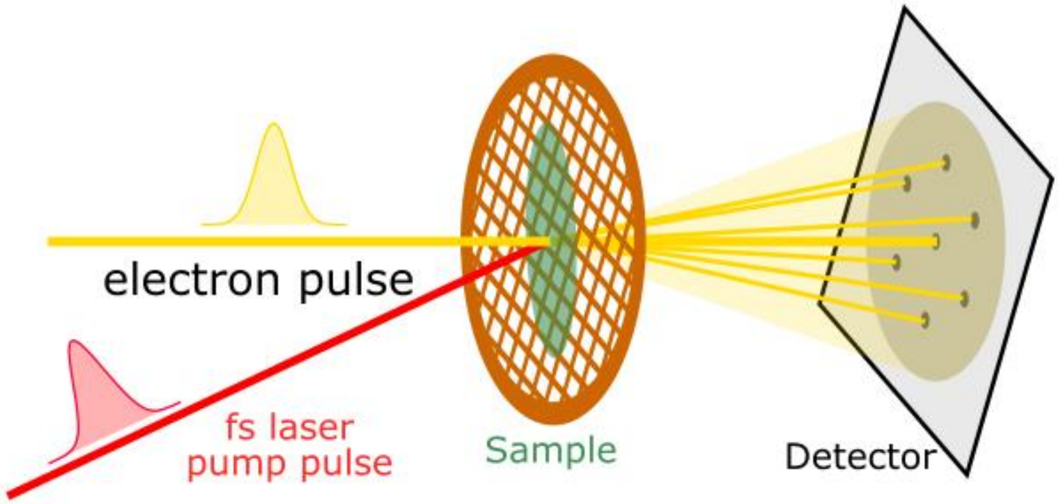

Figure 6.2: Schematic of ultrafast electron diffraction setup.

6.1.2 Temporal Resolution Measurement

One of the most important features of FED experiment is the ultrabright electron pulses have enough spatial and temporal resolution to study ultrafast atomic displacements.

Electron pulses accelerated by a 95 keV high voltage have enough spatial resolution to track the atomic motions in < 0.1 Å. However, because of the space charge effect (mentioned in Chapter 2), the pulse duration of the electron pulses is one key parameter for the overall temporal resolution of the FED system. Therefore, the pulse duration needs to be confirmed before every pump-probe experiment. The RF cavity in our DC-RF hybrid electron source can reduce the pulse duration of the ultrabright electron pulses at the sample position to ~300 fs [49,58]. Time-resolved streak camera is employed to measure the pulse duration of electron pulses before every pump probe experiment in this experiment. The RF field amplitude applies on the RF cavity needs to be optimize for different brightness of electron pulses.

Figure 6.3 shows the relationship between the pulse duration of electron pulses and the RF field amplitude. In order to keep small transverse width of electron pulse and obtain ultrashort pulse duration, the RF field amplitude is comprised between 1.6 MV/m to 1.75 MV/m. Therefore, the RF field amplitude is set to be 1.68 MV/m to obtain ultrashort and stable pulse duration. We also tried to increase the streak velocity by applying more voltage on the streak plates, because higher streak velocity increases the temporal resolution of the streak camera. However, the pulse duration of single electron pulse stayed around 180 fs FWHM.

In DC-RF hybrid electron gun, there are two main contributions to overall system temporal resolution. One is the pulse duration of single electron pulse 178 fs FWHM (Figure 6.3a) based on 63 pixel/ps streak velocity. The other is the arrival time jitter 200 fs RMS (Figure 6.3b). Therefore, the pulse duration of accumulated electron pulses is ~300 fs FWHM.

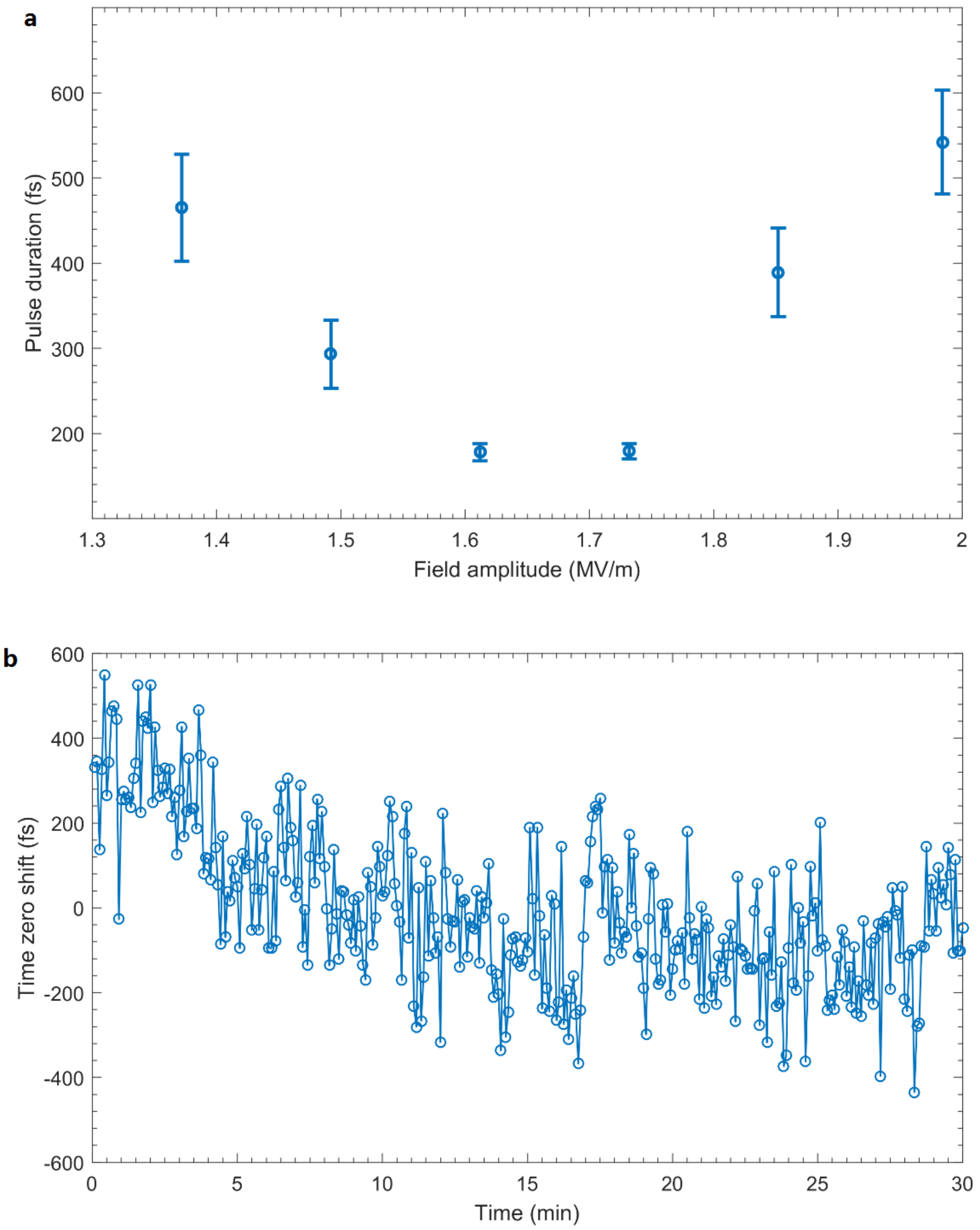

Figure 6.3: Pulse duration measurement. (a) Pulse duration measured by streak camera vs. RF field amplitude. Shortest pulse duration of single electron pulses is ~178 fs FWHM. (b) Single shot electron time zero shift vs time. The jitter of arrival time is ~200 fs RMS.

6.1.3 Excitation Fraction Calculation

To investigate the SCO dynamics of [Fe(PM-AzA)$_2$](NCS)$_2$, the pump pulse duration is (60±5) fs centered at 800nm. At the sample position, the energy per pulse of the pump is (9.55±0.05) µJ with a width of (550±20) µm. Therefore, the incident excitation fluence at the sample position was 1.28 mJ/cm^2. We also measured the transmission of the pump 800 nm laser to be (38±2) % at 170 K for further excitation calculations. Based on the above measurements, the excitation fraction of the experiment is 12.5% by calculating the number of absorbed photons and molecules in the crystal.

The excitation fraction calculation is critical in further electron diffraction data analysis, but the excitation fraction calculated from optical data may not be precise enough. Therefore, in order to confirm the excitation fraction, we applied another two methods to calculate the excitation fraction from electron diffraction signal beside excitation fraction obtained from laser excitation conditions.

First, the excitation fraction can also be calculated based on the intensity of Bragg peaks [50].

$$\eta_{exc} = \frac{F_{\exp}(k,t_{\infty})-F_{LT}(k)}{F_{HT}(k)-F_{LT}(k)} \tag{6.1}$$

η_{exc} is the excitation fraction; F_{LS} is the structure factor of the low spin state; F_{HS} is the structure factor of the high spin state. We assume the excited molecules have reached the HS excited state after 10 ps, and starts to have phonons oscillation at 20 ps, because the optical studies show that the SCO is finished in <50 fs. Therefore, we take the range between 10 ps and 20 ps as t_{∞}. A distributed of excitation fraction is expected, because η_{exc} calculated by this equation is sensitive to the signal-to-noise ratio of every Bragg peak. Figure 6.4 is the calculated excitation fractions of the strongest 26 diffraction peaks. The mean of excitation fraction is ~13.5 %.

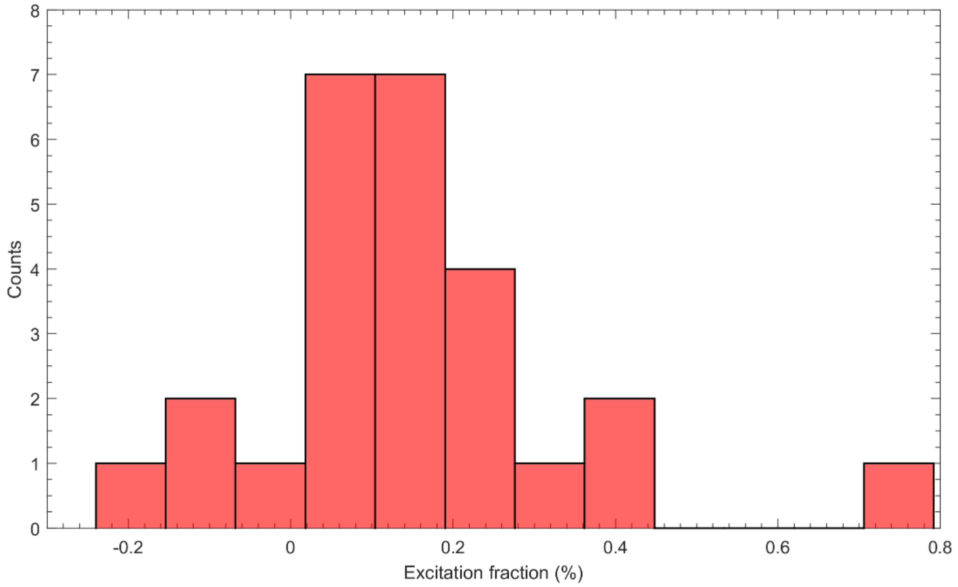

Figure 6.4: distributed of excitation fraction of selected 26 diffraction peaks

Furthermore, a systematic and clear shift in the position of Bragg peaks is observed in Figure 6.14a during the both thermal SCO when the temperature at the sample is raised from 170 K to 300 K. We believe this shift in the position of Bragg peaks is a result of the expansion of the unit cell mainly along the c-axis that accompanies thermal SCO phase transition. In Figure 6.14b, a similar shift in the position of Bragg peaks is also observed in photoinduced SCO. We fitted each Bragg peak with a 2D Gaussian function to determine the unit cell parameter c for each different condition of sample crystals.

Table 6.1: Determination the unit cell parameter c for each condition of sample crystals

T = 300 K, c_{HS}	17.0680 Å (from XRD data)
T = 110 K, c_{LS}	16.6770 Å (from XRD data)
T = 170 K, t = +10 ps, pump off, c_{OFF}	16.753 Å
T = 170 K, t = +10 ps, pump on, c_{ON}	16.783 Å
T = 170 K, c_{LT}	16.768 Å
T = 300 K, c_{HT}	17.076 Å

According to Vegard's law, these values can be related by using α and η, so the LS fraction at T= 170 K and the excitation fraction, respectively:

$$c_{LT} = \alpha c_{LS} + (1 - \alpha)c_{HS}$$

$$c_{HT} = c_{HS}$$

$$c_{OFF} = c_{LT}$$

$$c_{ON} = \alpha\big((1 - \eta)c_{LS} + \eta c_{HS}\big) + (1 - \alpha)c_{HS} \tag{6.2}$$

By solving these two unknown parameters, we calculate α = 78.9% and η = 9.6%, which are consistent estimation compared to the result obtained by other methods such as temperature-dependent magnetic susceptibility ($\alpha \sim$ 75%) and pump laser fluence data ($\eta \sim$ 12.5%).

6.1.4 FED Data Collection

Time-resolved electron diffraction patterns were obtained with an exposure time of 0.2 seconds at 100 Hz (20 electron pulses). 20 electron pulses accumulated in one diffraction pattern can avoid saturation of peak (0 0 0) on CCD screen. On the other hand, 100 Hz repetition rate can make sure samples can recover from last excitation before next pump laser.

The change of Bragg peak intensity in this SCO dynamics ($(I_{on}$-$I_{off})/I_{off}$) is sub 3%, so the stability of the electron pulses needs to be improved. Therefore, as mentioned in Chapter 2, the width of the pinhole on the anode in the electron gun was reduced from 500 μm to 200 μm to improve the brightness stability. Although intensity of UV laser which is directly related to the brightness of the electron pulses may change during up to 20 hour's experiment, the brightness of electron pulse is still stable. In order to increase the single-to-noise ratio of the time-resolved change of Bragg peak intensity, every time step of the time traces was repeated by 250 diffraction patterns. The final time trace is an average of 5,000 pulses per time point.

6.1.5 Fluence Dependence

Fluence dependence is an important supplementary measurement, because a lot of important information can be obtained by the fluence dependence measurement such as the excitation condition and the sample damage induced by heat accumulations. In this supplementary measurement, the fluence dependence of our sample for excitations is measured from 0.93 mJ/cm^2 to 1.38 mJ/cm^2. Higher than 1.38 mJ/cm^2 fluence was tried and a slow decrease of diffraction peaks' intensity in 3 hours which indicates a damage threshold was observed. However, the intensity of diffraction peaks stayed same after weeks' experiment at 1.28 mJ/cm^2 fluence. The changes in the diffraction intensity of the Bragg peaks at lower than 0.93 mJ/cm^2 fluence are close to background noise. Figure 6.5 shows the normalized averaged signals of four selected Bragg peaks in the time step range between 10 ps and 20 ps as a function of the fluence. In this range, the excited molecules have reached the HS state while the phonon oscillation in the crystal have not started. Although the signal-to-noise ratio is not perfect because of relative small changes in the diffraction intensity of the Bragg peaks, it is clear that the fluence we applied to pump single crystal $[Fe(PM\text{-}AzA)_2](NCS)_2$ is in the linear range of the fluence dependence plot. Figure 6.5 and Figure 6.6 show selected peaks' change while pump fluence increasing.

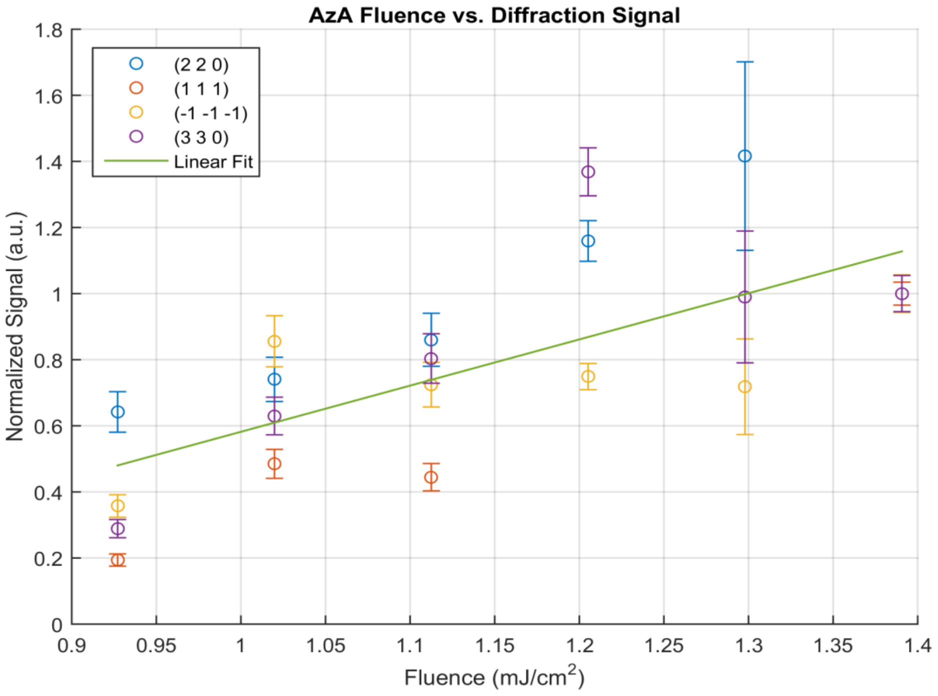

Figure 6.5: Summary of fluence dependence of $[Fe(PM\text{-}AzA)_2](NCS)_2$

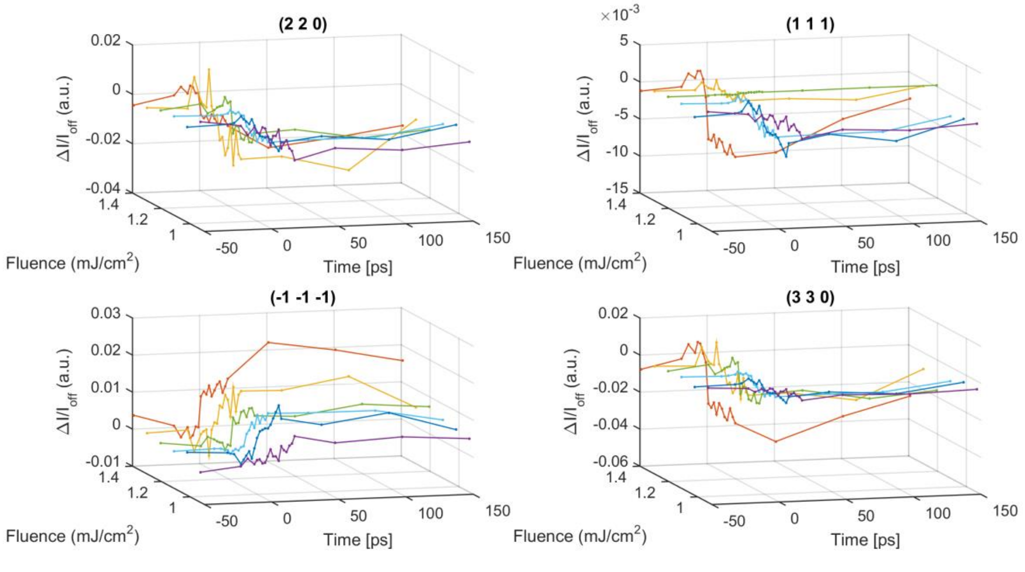

Figure 6.6: Fluence dependence of selected diffraction peaks

6.2 FED data analysis

6.2.1 Orientation determination and indexing

The first step of the time-resolved FED data analysis is to determine of the crystal orientation of the sample, which is also the incident direction of the probing electron pulse. Here, the electron diffraction patterns of the sample are simulated over 8 parameters and compared with the experimental diffraction patterns at T = 300 K to find the crystal orientation. These parameters are: camera parameter, 3 Miller indices, sample thickness, overall coherence length, in-plane sample rotation, Debye-Waller factor.

The camera parameter is the conversion factor between the local coordinate system on the camera sensor to the absolute coordinates in reciprocal space. The 3 Miller indices determine the relative direction of the incident vector to the reciprocal unit vectors. The sample thickness and overall coherence length are modelled using a Gaussian shape function to the reciprocal lattice points; they are the inverse of the width along the parallel and perpendicular direction to the incident vector, respectively. In-plane sample rotation refers to the rotation around the incident direction. The Debye-Waller factor is taking account as Gaussian pre-factor that attenuates the magnitude of the structure factors at higher scattering angles. Figure 6.7 shows the result of the refinement process.

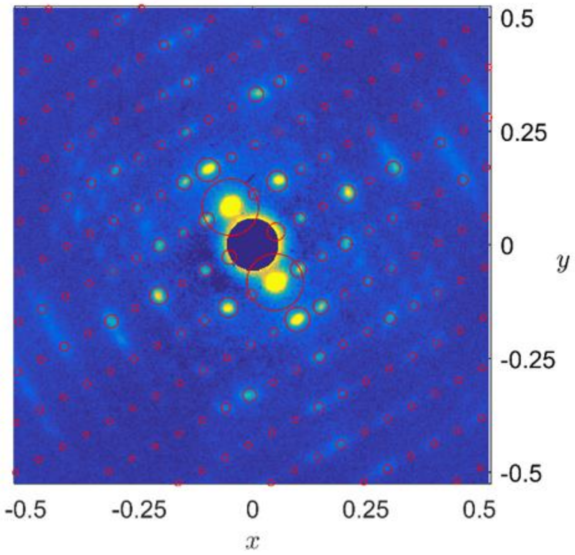

Figure 6.7: Refinement of Crystal Orientation. Electron diffraction pattern at 300 K is overlaid with simulated data under best-fit parameters.

6.2.2 Simulations of structural factor

One important observation in our FED study on single crystal $[Fe(PM\text{-}AzA)_2](NCS)_2$ is that the structure change during the photoinduced SCO goes through both Fe-N bond elongation, ligand motion and unit cell expansion simultaneously. This observation challenge previous studies [19-21] which suggest that the Fe-N elongation happens simultaneously with the changes of the electronic states with sub-150 fs time constant. Therefore, it is critical to confirm whether our FED has enough spatial and temporal resolution to observe ~0.2 Å Fe-N bond elongation in sub 150 fs time scale and simulate the changes in the diffraction intensity of the Bragg peaks which we are supposed to observe if the Fe-N bond elongation happens in sub 150 fs, following with other motions in 2 ps.

The changes in the diffraction intensity of the Bragg peaks are associated with atomic motions by changing the interferences of electrons. Structure factor (F) can indicate these changes in the diffraction intensity of the Bragg peaks, because the position of atom j within the unit cell determines the intensity of a Bragg peak which is proportional to the square of the structure factor [36,86,87].

$$I(hkl) \propto |F(hkl)|^2 \tag{6.3}$$

Therefore, the changes in the diffraction intensity of the electron diffraction patterns in the FED can be simulated, based on structure factor change from motions in the unit cell.

In the data analysis of the time-resolved diffraction patterns, the kinematic theory was applied to simulate the diffraction patterns [36]. Before the use of kinematical theory over dynamical theory, Weak-phase-object approximation (WPO) need to be considered. Based on the FED experimental conditions, it is reasonable to employ the single scattering formulation for the calculations of $[Fe(PM\text{-}AzA)_2](NCS)_2$ electron diffraction patterns [88]:

$$F(k) = \sum_{j=1}^{N} f_{\mathrm{j}} \; \mathrm{e}^{2\pi \mathrm{i} \mathrm{k} \cdot r_j} \tag{6.4}$$

where f_j is the atomic scattering factor for the j^{th} atom, parameterized as [88]:

$$f_j(k) = \sum_{l=1}^{5} a_l e^{\frac{1}{4} b_l k^2} \tag{6.5}$$

6.2.3 Contribution of changes in the diffraction intensity

To simulate the changes of the structure factor during the SCO dynamics, the low spin structure at 110 K and the high spin structure at 300 K from structure data base [85] are used to study the contribution from different motions. The changes in the diffraction intensity of the Bragg peaks can be considered to be the summary of the Fe-N bond elongation and other ligand motions. Figure 6.16 and Figure 6.17 show the contributions of changes in the diffraction intensity (in percentage and indicated by different colors) of selected most intense Bragg peaks.

6.2.4 Structure factor calculation based on the Fe-N elongation and other motions.

Other than the calculation in Chapter 6.2.3, we also calculated the structure factors of different Bragg peaks based on assumptions from previous studies [19-21].

The Fe-N bond elongation and other motions in molecule are considered individually. In the structure factor calculation, we assume, LS=small Fe-N & LS atom position; LS*=big Fe-N & LS atom position; HS*=small Fe-N & HS atom position; HS=big Fe-N & HS atom position.

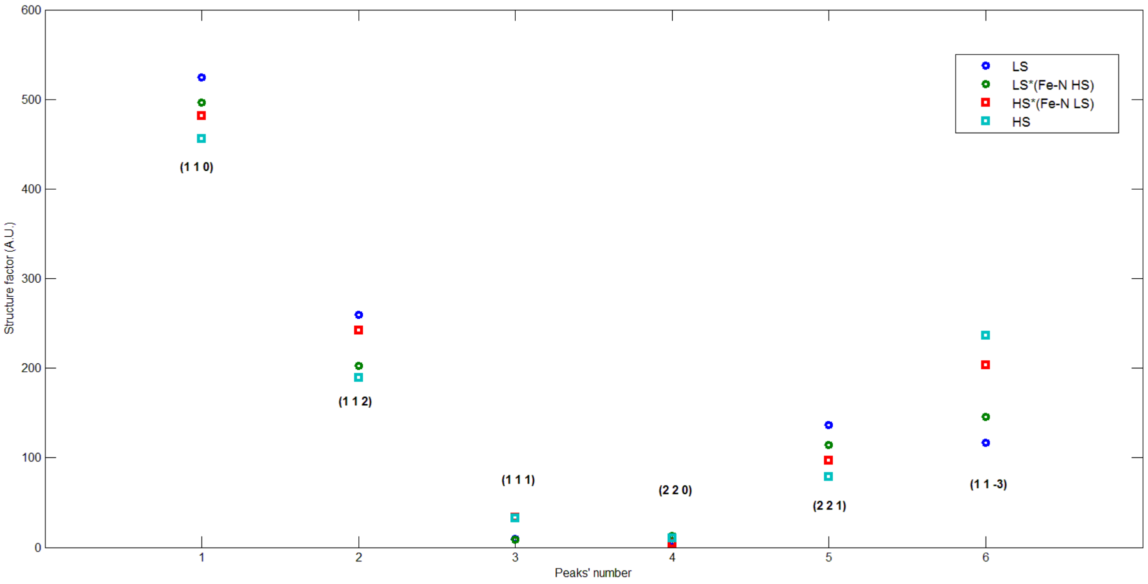

Figure 6.8: Structure factor simulation of the contributions from Fe-N elongation and other motions in SCO dynamics.

For peak (1 1 1), LS (9.86) equals to LS* (8.88) and HS (242) equals to HS* (189), so the changes from big Fe-N and small Fe-N is similar. The intensity of Peak (1 1 1) has no influence from the Fe-N bond elongation, and the change of peak intensity is dominated by molecule reorganization.

For peak (2 2 0), LS (6.27) equals to HS* (4.95) and HS (10.45) equals LS* (12.53), so the changes from big Fe-N and small Fe-N is similar. Most contribution is from Fe-N bond elongation.

For peak (1 1 0), LS* equals to HS*, so the difference between big Fe-N and small Fe-N is similar to the difference between HS atom position and LS atom position. The contributions from Fe-N bond elongation and molecule reorganization are similar.

For most peaks, the changes from the Fe-N bond elongation are big enough to be noticed easily. According to previous SCO literature [65-71], the Fe-N bond elongation happens in sub 200 fs and molecule reorganization happens in sub 2 ps. Therefore, peak (1 1 1), peak (1 1 0) and peak (2 2 0) should have different time constants.

The UED signal of peak (1 1 1) should be the signature of the molecule reorganization and HS vibration cooling, and its time constant is supposed to be around 2 ps. The signal of peak (2 2 0) should show a fast signal around 200 fs. Because our UED system's time resolution is 300 fs, a fast signal should be found around 400 fs and a slower signal is following.

6.2.5 Global Fitting of Time-dependent Diffraction Intensity

In the FED experiment data analysis of $[Fe(PM\text{-}AzA)_2](NCS)_2$, we found that there is only one step of structural changes of the photoinduced SCO. In order to support this statement, we checked the time constant of almost all bright diffraction peaks.

Of the hundreds of observable Bragg peaks, we selected 30 representative ones that are bright and/or show strong pump-probe signal $\Delta I_i(t)$ where

$$\Delta I_i(t) = \frac{I_{i,ON}(t) - I_{i,OFF}(t)}{I_{i,OFF}(t)} \tag{6.6}$$

$I_{i,X}(t)$ is the intensity of diffraction peak i under pump state X at time t. These data points are then described using a global fitting model as follows:

$$\mathrm{S}_i(t) = G_\sigma(t) \, * \, \left[c_i\left(1 - e^{-t/\tau}\right)\right] = \frac{1}{2} c_i \left[\left(1 + \mathrm{erf}\left(\frac{t}{\sqrt{2}\sigma}\right)\right) - e^{-t/\tau} e^{\frac{1}{2}(\sigma/\tau)^2} \left(1 + \mathrm{erf}\left(\frac{t - \sigma^2/\tau}{\sqrt{2}\sigma}\right)\right)\right] \tag{6.7}$$

σ is the instrument response time (267 fs FWHM or 113 fs 1/e) . By fitting all the data points simultaneously, we obtained a robust value for the time constant: $\tau = (2.32 \pm 0.09)$ ps.

6.2.6 Comparison between mono-exponential and bi-exponential behaviour

As mentioned above, literature [19-21] strongly suggests that the Fe-N bond undergoes abrupt elongation on the same timescale as the spin transition, $\tau \sim 150$ fs. However, no such time constant was found in the fitting of our time traces, where each diffraction signal can be fitted to a single and much longer exponential time constant, $\tau \sim 2.32$ ps.

A concern is that a faster signal could be present in our data and is simply obscured by fitting a possible bi-exponential decay with a single mono-exponential function. Such a fast signal would appear with a time constant that is limited by our instrument response time. To check whether a bi-exponential decay of $\tau_1 = 113$ fs and $\tau_2 > \tau_1$ can be fitted by a single mono-exponential decay with $\tau_{1,2} \sim 2.32$ ps, we simulated bi-exponential data $S_{sim}(t, \tau_1, \tau_2)$ over a broad range of possible $\tau_1,\ \tau_2$ and applied our least-square fitting routine with $S_{fit}(t, \tau_{1,2})$.

$$S_{sim}(t, \tau_1, \tau_2) = G_\sigma(t) \ast \left[1 - \frac{1}{2} e^{-t/\tau_1} - \frac{1}{2} e^{-t/\tau_2}\right] \tag{6.8}$$

$$S_{fit}(t, \tau_{1,2}) = G_\sigma(t) \ast \left[1 - e^{-t/\tau_{1,2}}\right] \tag{6.9}$$

In Figure 6.9a, τ_1 is set to the instrument response time and the largest $\tau_{1,2}$ achievable is less than 0.8 ps. In Figure 6.9b, it is clear than no combination of $\tau_1 < 1$ ps and τ_2 yields a signal that can be fitted by a $\tau_{1,2}$ close to the observed value of 2.32 ps.

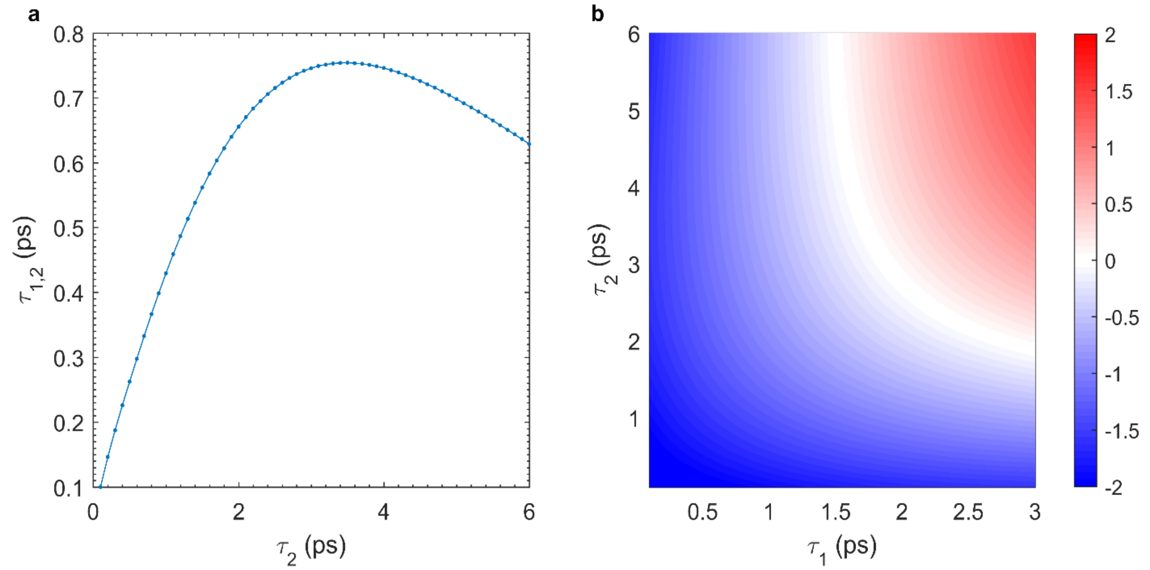

Figure 6.9: Fitting a bi-exponential decay with a single mono-exponential function. (a) Plot of fitted mono-exponential time constant as a function of the τ_2 for τ_1 = 0.113 ps. (b) 2D surface plot of fitted $\tau_{1,2} - 2.32$ ps over the possible values of τ_1 and τ_2.

6.2.7 Time-dependent Model of Atomic Motions

The electron diffraction is a direct probe of atomic positions. Here, we follow the motion of the atoms during the photoinduced SCO by an approach similar to previous works on structure recovery from ultrafast electron diffraction data [50,51]. We applied this similar method to study the time-dependent model of atomic motions. A model is constructed by the atomic displacements parameterizing into 3 normalized variables (ξ_1, ξ_2, ξ_3) that would link the LS and HS molecular structures within their respective crystallographic unit cell. For each time point measured in the experiment, a least square fitting routine is used to find the optimal set of parameters (i.e. reaction coordinates) that would best match the observed changes in diffraction intensity.

We defined these 3 reaction coordinates as follows:

1) Elongation of the 6 Fe-N bond, collinear with the bond direction
2) Motion of the PM-AzA ligands, relative to the Fe atom position

3) Symmetric expansion of the crystallographic unit cell

The result of the fitting is a series of points in the 3D configuration space that best match observation and track out the entire reaction pathway from the initial LS structure to a final HS-like one.

6.2.8 Acoustic Phonon Analysis

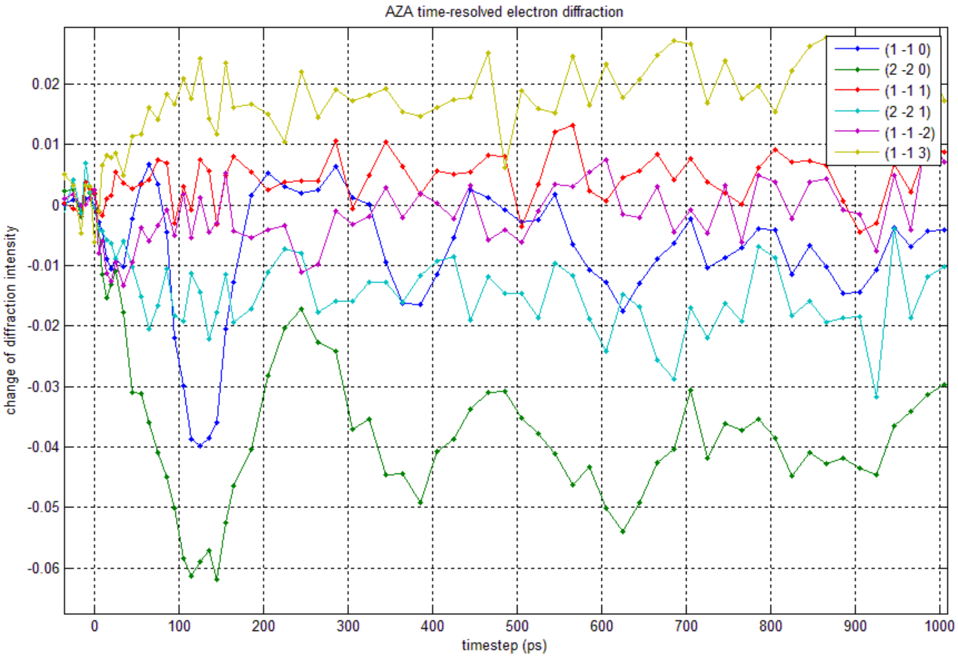

Figure 6.10: Oscillation of changes of diffraction intensity of selected diffraction peaks.

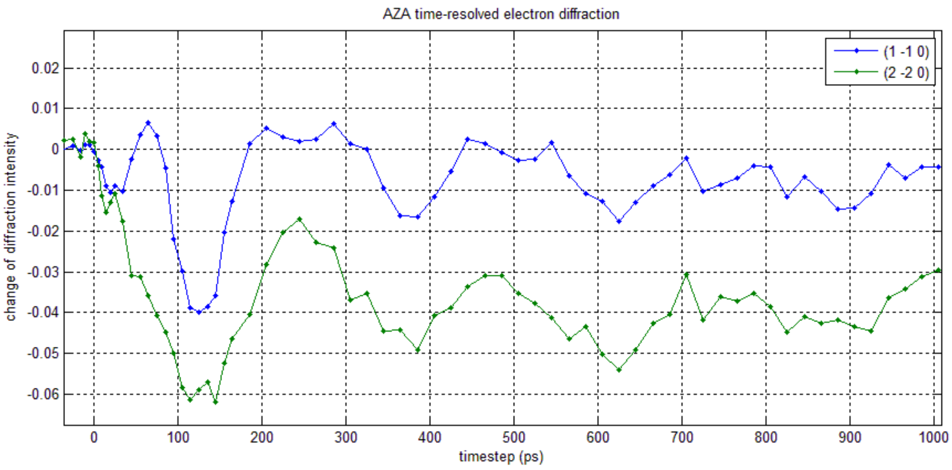

Figure 6.11: Clear oscillation of intensity of Bragg peaks (1 -1 0) and (2 -2 0)

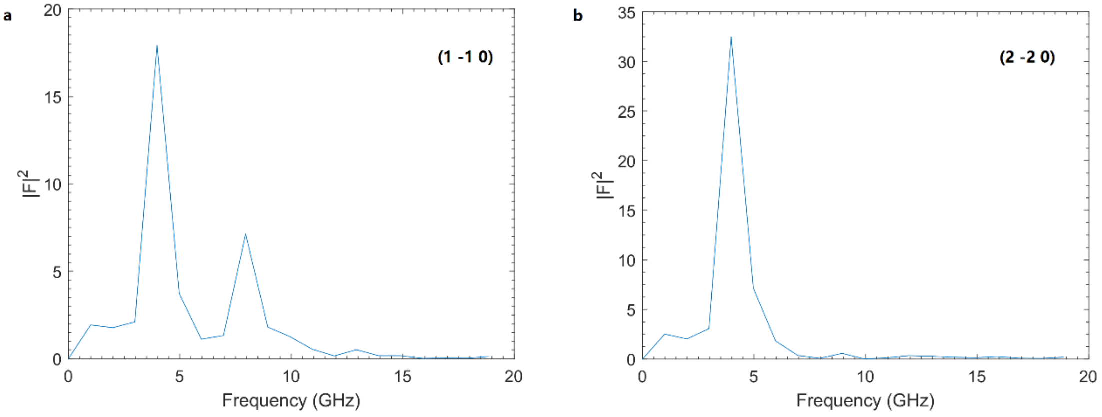

Figure 6.12: Fourier transform of Bragg peak (1 -1 0) to present two frequency components at 3.96 GHz and 7.92 GHz frequency while Bragg peak (2 -2 0) has one frequency components at 3.96 GHz frequency.

In the longer time scale (-50 ps to 1005 ps), the oscillations of diffraction intensity of Bragg peaks are observed (Figure 6.13 inset). The biggest oscillations are from the Bragg peaks (h=k≠0, l=0) which is related to the orientation of crystal. In Figure 6.12, the Bragg peak (1 -1 0) and the Bragg peak (2 -2 0) are selected to displayed oscillation breathing modes in long time scale. Fourier transform is applied to obtain the frequency of oscillations[9]. In Bragg peak (1 -1 0), two frequency components at 3.96 GHz and 7.92 GHz frequency were found, equivalent to the periods of the oscillation of 126 ps and 250 ps. The pump laser exposed on surface of the sample crystal, the periods of these oscillation breathing modes correspond to round-trip acoustic propagation normal to the film surface. Two frequency components represent both longitudinal and transverse acoustic phonons. The period of the biggest oscillation is 250 ps, so the speed of sound implied by the period is 1190 m/s, in good agreement with typical values obtained in molecular crystals [18,89], based on 150 nm sample thickness.

6.3 Result and discussion

Figure 6.13 is the change of static electron diffraction patterns, corresponding the structural changes, from the LS ground state to the HS excited state at 170 K and 300 K, respectively. The change in the intensity of Bragg peak intensity induced by thermal SCO matches approximately with those photoinduced changes measured at 170 K, after first 5 ps SCO dynamics, plateau from 5 to 20 ps in Figure 6.14a. It also matches the simulated changes in the diffraction intensity of Bragg peaks using LS, HS x-ray structure in Figure 6.14b.

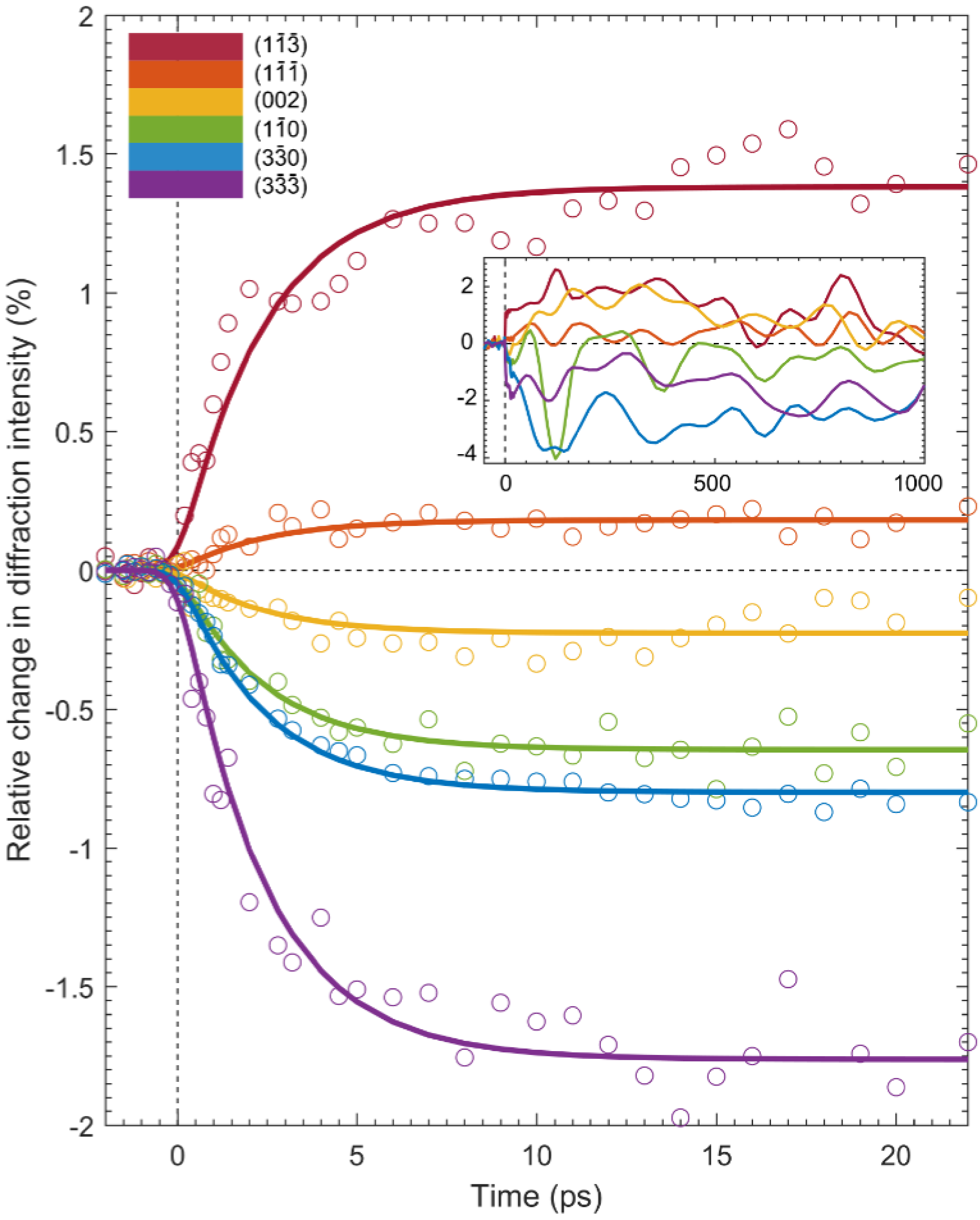

Figure 6.13: short-time relative change in the intensity of select Bragg spots from t = -5 ps to 24 ps; inset: long-time plot from -50 ps to 1000 ps.

However, there is more than just a Fe–N bond elongation but also ligand motion and unit cell expansion in the entire SCO. Figure 6.14 a gives the normalized relative changes in the diffraction intensity of some selected Bragg spots. The transient behavior on the longer time scale was also revealed.

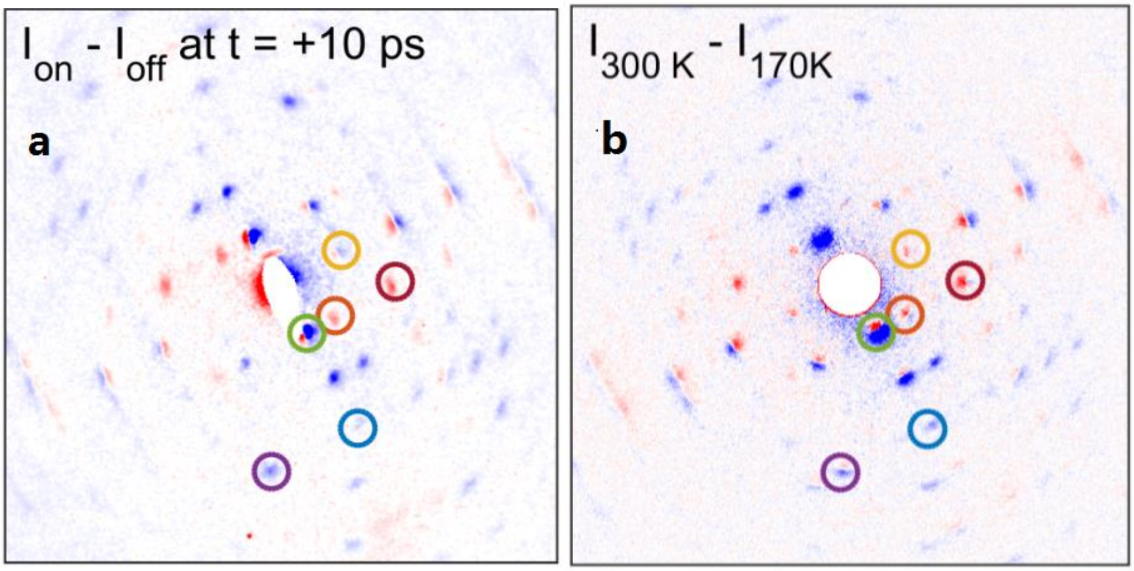

Figure 6.14: (a) Difference electron diffraction patterns from photo-induced SCO (b) Difference electron diffraction patterns after temperature change.

One of most noteworthy features in Figure 6.13 is that for all of the Bragg peaks studied, we only observed one type of behavior: a decay or rise after excitation with ~2 ps time constant. We also note that for Bragg peaks (h=k=0, l≠0) such as (002), (004) and (006), shifts in peak position have same time constant like changes in the diffraction intensity of the Bragg peaks. The shift with same time constant of changes in the diffraction intensity shows substantial unit cell expansion is taking place on the ultrafast time scale with other nuclear motions of entire molecule.

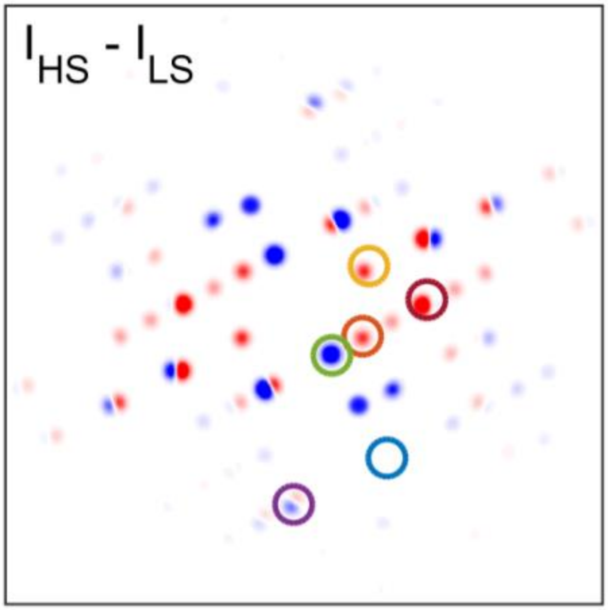

Figure 6.15: Difference electron diffraction patterns simulated based on HS and LS structures from X-ray diffraction measurement.

To obtain molecular motions in real space behind the changes in the diffraction intensity of Bragg peaks and peak position shift, we calculated for most diffraction peaks' structure factor change [36] when the molecule undergo to HS structure by different pathways of atomic motion in Figure 6.16 and Figure 6.17. Two possible pathways for atomic motion were considered. In Figure 6.16, we display the structure factor calculation of the excited state structure after a sub 300 fs ultrafast Fe–N bond elongation and before a 2 ps slower ligand motion suggested by previous literature [19-21]. Most Bragg peaks' behaviour was not observed in the experiment on the subpicosecond time scale (see Figure 6.14a). In contrast, we considered a coupled movement of Fe–N bond elongation and ligand motion with unit cell expansion (see Figure 6.17a) which is a direct motion from LS to HS, and most changes in the diffraction intensity (see Figure 6.17b) are very close to observation from experiment (see Figure 6.14a).

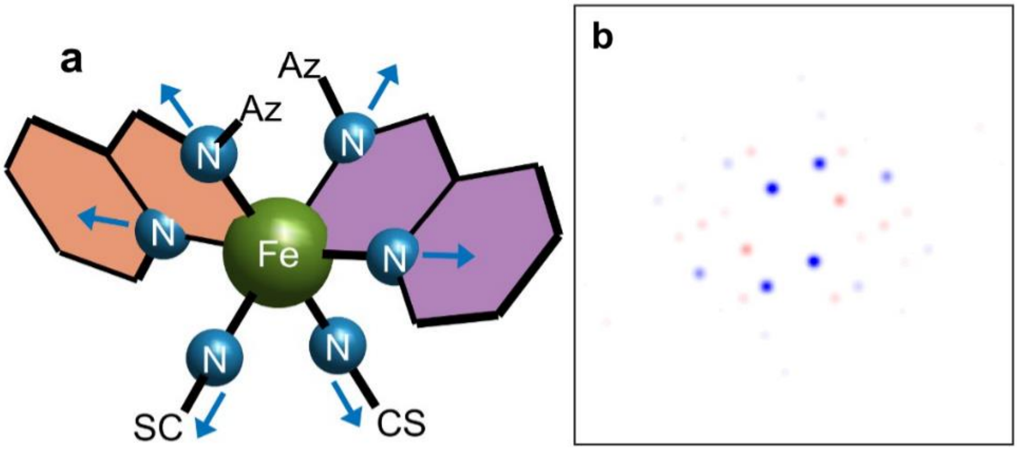

Figure 6.16: (a) model 1: elongation of Fe–N coordination bond by an average of 0.2 A. (b) simulated change in electron diffraction from model 1.

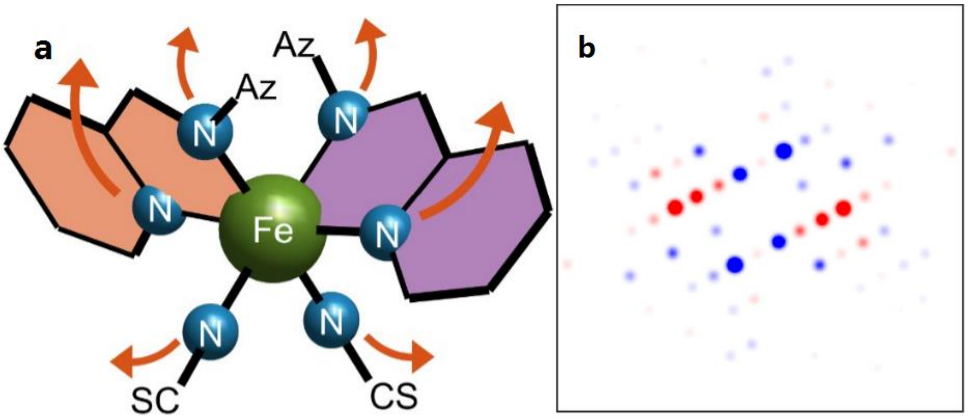

Figure 6.17: (a) model 2: simultaneous nuclear motions from low-spin to high-spin structure. (b) simulated change in electron diffraction from model 2.

On the other hand, the contributions from different molecular motions to Bragg peaks intensity are also calculated. In Figure 6.18, selected peaks receive different contributions from Fe–N bond elongation and ligand motion including unit cell expansion. Most contribution of the change in the diffraction intensity of Bragg peak $(1\bar{1}\bar{1})$ is from ligand motion; Bragg peaks $(1\bar{1}0)$ $(3\bar{3}0)$ (002) obtain different contributions from both Fe–N bond elongation and ligand motion. If Fe–N bond elongation happens in sub 150 fs following with ligand motion in ~2 ps, peak $(1\bar{1}\bar{1})$, peak $(1\bar{1}0)$, peak (002) and peak $(3\bar{3}0)$ should have different time constants which are not observed in experiment. Only coupled motions of Fe–N bond elongation and ligand motion can explain one type behavior of all Bragg peaks.

Fe–N bond distance is usually employed as a smoking gun to describe geometrical changes in SCO including changes of N-Fe-N angle and ligand, because the largest geometrical changes in SCO occur for the Fe–N distance [59,97]. The potential energy surfaces of different electronic states of Fe are plotted as a function of Fe–N bond distance [59]. In ultrafast SCO dynamics, Fe–N elongation, unlike other motions in ligand, is believed to be a conclusive evidence of SCO [65-71] and directly correlated to the electronic state dynamics in time (150 fs), because LS-HS dynamics results in a repulsive force on the atoms for two electrons being promoted to anti-bonding orbitals and Fe–N bonds losing π backbonding. However, the Fe–N bond is longer and much weaker than the N-C bonds in the ligands (2.0 Å vs 1.3 Å). Therefore, the change in energy associated with the Fe–N elongation is too small to allow the immediate distortion of the much stronger bonds in ligand. Instead of incoherent vibrational cooling as reported before, the population of the anti-bonding Fe–N orbital drives the Fe–N stretching mode which is in turn coupled to other modes that coherently/collectively distort the molecule to the new energy minimum. Fe–N bond elongation is coupled to the entire ligand motion and molecule reached bottom of HS state in ~2 ps which was observed by other optical studies [11-19]. The one type of behaviour of changes in the diffraction intensity and position shift shows despite sub 150 fs electronic state change of SCO which decrease the bond energy of Fe–N bond, the Fe–N bond elongation is coupled with entire molecule phase shift including ligand motion and unit cell expansion, and is delayed with respect to the electronic transition.

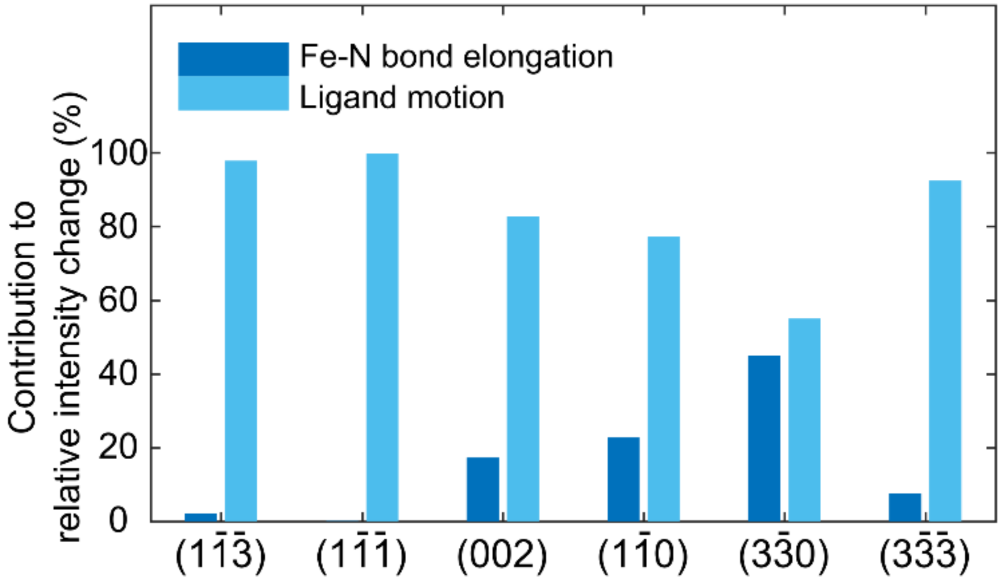

Figure 6.18: Contribution to relative changes in the diffraction intensity. Comparing changes from Fe–N bond elongation versus all other nuclear motions.

Several points are worth mentioning to support our observation and discussion. First, FED system is a direct method to study atom motion with ~0.04 Å space resolution and 267 fs time resolution [49,50,58]. Its space and time resolution is high enough to monitor 0.2 Å Fe–N bond elongation is sub picosecond time scale. Based on the instrument response time, a sub 300 fs change of selected peaks is supposed be seen, if the Fe–N bond distance is directly correlated in time with the electronic state changes. Second, the sub 2 ps ultrafast structure transition in this study is only induced by photo-induced SCO. Although deposited laser energy on lattice can result in lattice expansion and thermal SCO which can also induce Fe–N bond elongation and unit cell expansion, it only happens with inhomogeneous lattice expansion in 10 ns – 10 µs time window, following with homogeneous crystal expansion and thermal SCO at 50 µs [90,91]. Only Bragg peaks (h=k=0 l≠0) had position shift in ultrafast time scale indicating unit cell c axis expansion, and c axis expansion in unit cell is the largest and following with Fe atom fraction change along c axis. Thus, the unit cell expansion in ultrafast time scale is the result of photoinduced SCO instead of pure thermal unit cell expansion. Therefore, all the phase transition observed in this study is local molecular photo-switching with structural motion at LT unit cell. Finally, transient absorption reflectivity spectroscopy and XANES are not direct way to observe the Fe–N elongation because the former approach is more sensitive to the electronic changes [87] of the material whereas the latter one relies on MXAN simulation and assumed INT structures [77,81,92] to speculate Fe–N bond elongation.

Another noteworthy feature is the plateau behaviour observed for time delay from about 5 ps to 20 ps, which reflects an excited HS structure. To obtain a time-dependent map of the molecular motions of SCO, we applied a structural refinement algorithm based on a parameterized molecular model [50,51]. The model refinement calculations compare |Fexp(k, t)| with simulated amplitudes |ηexcFsim,exc(k, ξ)+(1-η)Fsim,LT(k)| and maximize the Pearson correlation coefficient, γ(|Fexp|, |Fsim|). In the photoinduced SCO process, the structure motion from LS to HS can be decomposed to three independent groups: Fe–N bond elongation; ligand motion to HS structure; unit cell expansion. The term ξ is an atomic structural parameter composed of the three time-dependent generalized reaction coordinates (ξ N ξ L ξ U) assigned to the motion of three independent groups.

Figure 6.19 depicts the three key dynamical groups and temporal evolution of each key dynamical group, Fe–N bond elongation and ligand motion and unit cell expansion, representing the ultrafast structure motion dynamics in SCO, respectively. Figure 6.20 is a clear time dependent trace of Fe–N bond elongation to show the average Fe–N bond expanded to 0.171Å in photo-excited state with 2 ps time constant (91% of Fe–N elongation from thermal SCO). The time constant of these three key dynamical groups are 2 ps and they are coupled to each other in the photoinduced SCO. The time-dependent changes of ξ are summarized in Figure 6.20 to show the collective motion of three dynamical groups. The reaction coordinate of three motions represent relative structure motion from initial {ξ = (0,0,0)} LS to {ξ = (1,1,1)} HS. Previous picosecond X-ray diffraction studies on later slow SCO process indicate there is a local excited HS state which is photo switched to HS electronic state with structural reorganization at LT crystal unit cell. Here, we measured the photo-excited HS structure {ξ = (0.9,0.8,0.75)} and found molecule was forced to be reorganized in relative smaller unit cell than regular HS unit cell in HT. We notice unit cell expands in ultrafast time scale and this motion is coupled to Fe–N bond elongation and ligand motion which was not observed in previous X-ray diffraction studies.

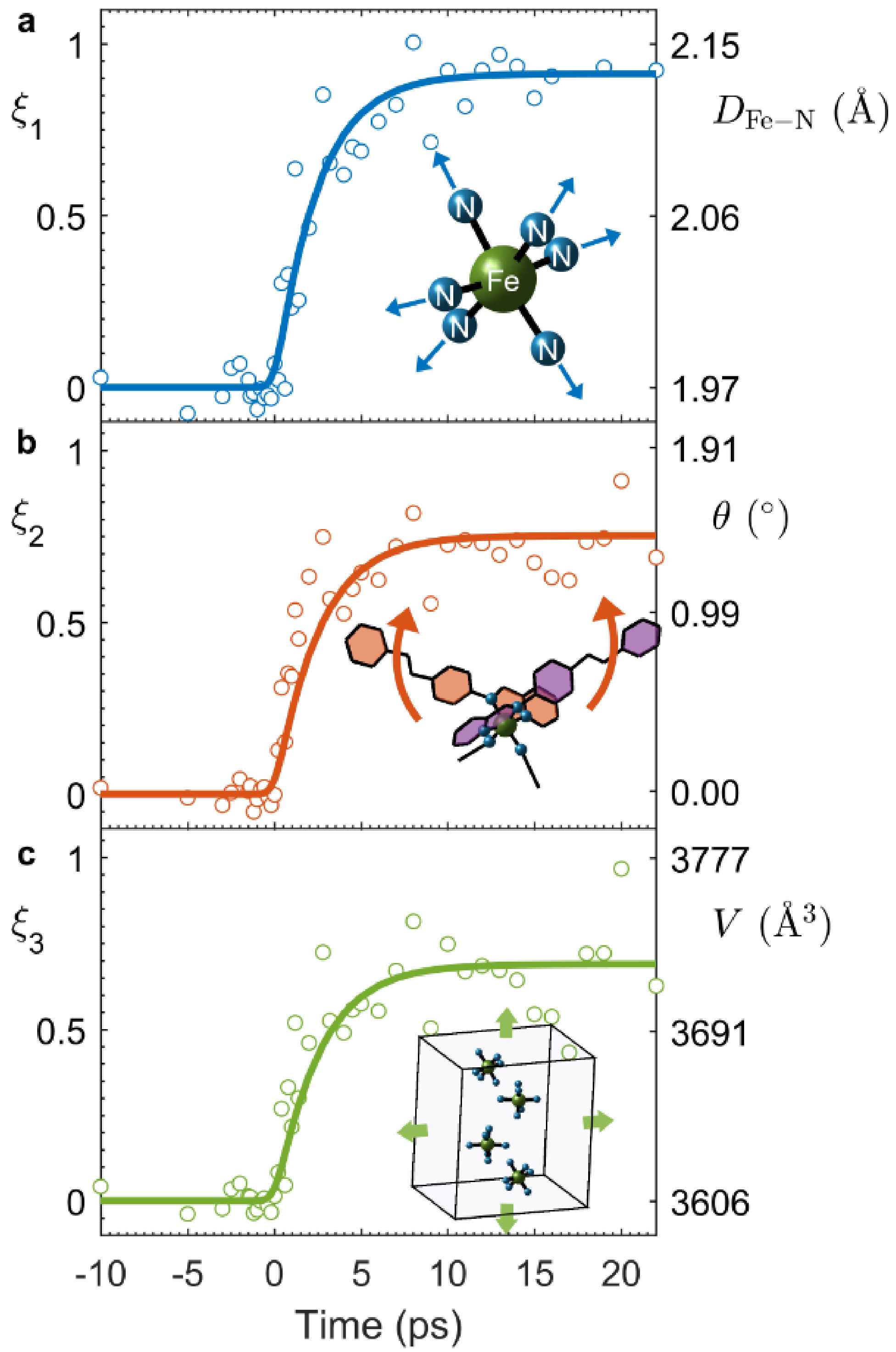

Figure 6.19: Molecular movie. a-c, time-dependence of refined reaction coordinates.

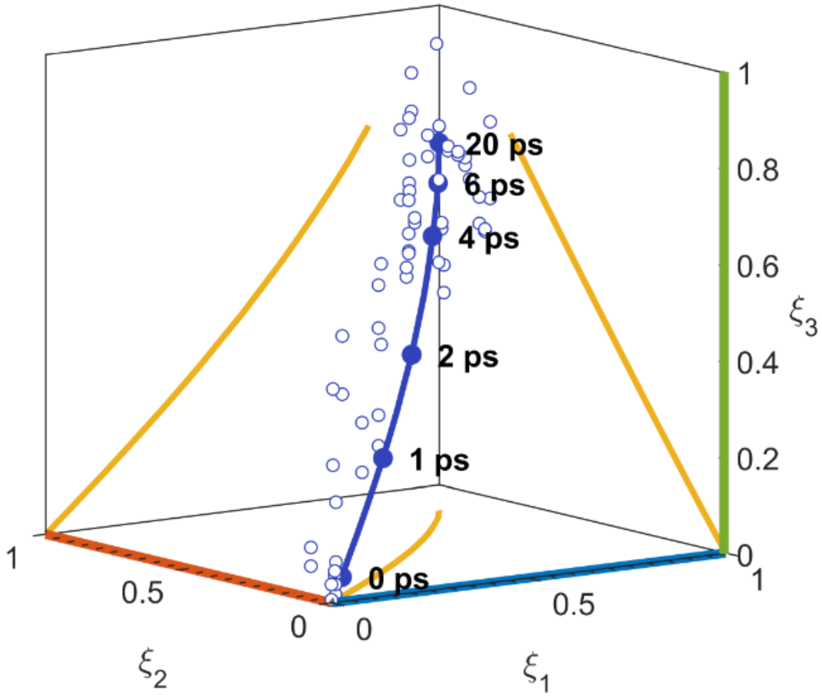

Figure 6.20: Plot of refinement over reaction-coordinate space.

6.4 Conclusion

Figure 6.21 presents the major steps of electronic and structural changes of the SCO dynamics from the structural information in this FED work and previous studies:

(1) The electronic state change of SCO dynamics happens from MLCT manifold to HS $^5T_2$ state within 150 fs via intersystem crossing (ISC) [11,24,36], or a direct MLCT→$^5T_2$ conversion on the extremely short timescale of <50 fs [11]. After 150 fs, the electronic state of Fe(II) atom has reached HS $^5T_2$ state, but the SCO molecule stays at the original LS structure including Fe-N distance, ligand in the LT unit cell.

(2) The vibrational “hot” molecule in the HS state surface undergo vibrational cooling to the fully relaxed bottom of HS state on timescales of 2 ps [11]. In this vibrational cooling process, Fe-N bond distance and other ligand motion in SCO molecule are coupled to switch toward the HS structure from the LS structure on timescales of 2.3 ps.

(3) The vibrational cooling process occurs on timescales of 2 ps. On this time scale, there is no time for thermal unit cell expansion and molecule was forced to be reorganized in relative smaller unit cell than regular HS unit cell in HT. Therefore, the structure of HS state molecule is similar to the HS state molecule in HT unit cell, but the percentage switched of different structure motions varies. Unit cell expands in ultrafast time scale and this motion is coupled to Fe–N bond elongation and ligand motion are observed.

(4) After vibrational cooling, the photoinduced SCO process has finished. The HS fraction reaches plateau until elastic and thermal steps start to increase the HS fraction by deposited laser energy on photo-excited molecules after 0.1 ns [90, 91].

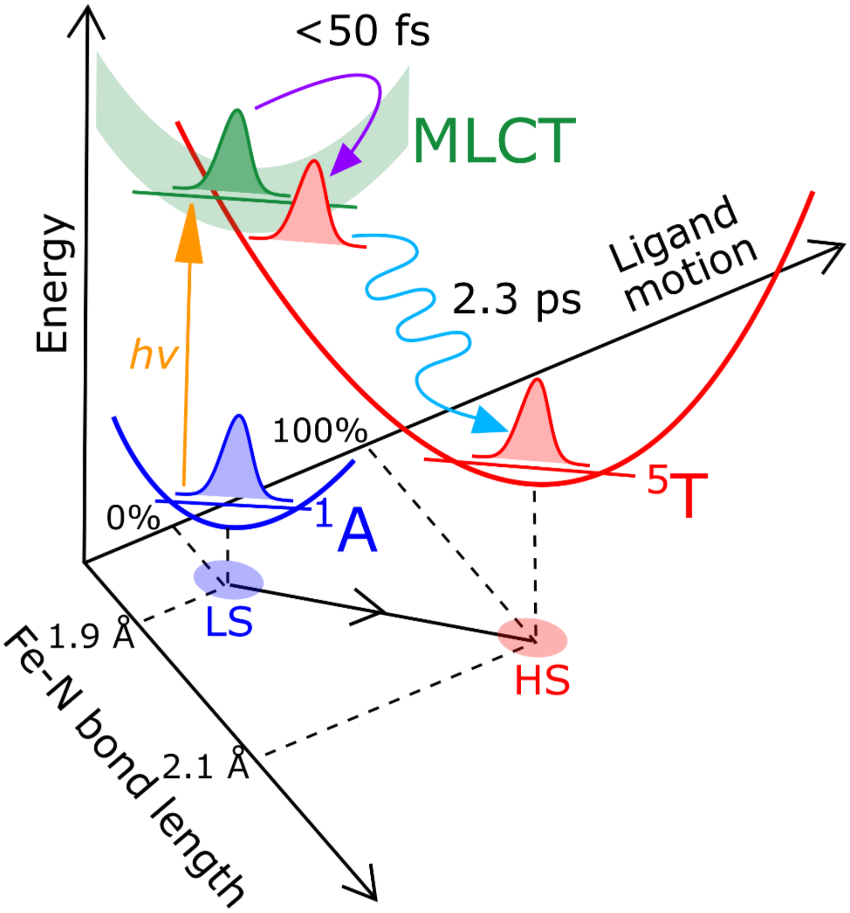

Figure 6.21: Schematic representation of the proposed reaction pathway of SCO in configuration space.

Chapter 7

Conclusions and Future work

In this chapter, a brief overview of the FED study on single crystal $[Fe(PM\text{-}AzA)_2](NCS)_2$ is presented first. Future work on the photoinduced SCO dynamics is discussed as well.

7.1 Summary of $[Fe(PM\text{-}AzA)_2](NCS)_2$ FED results

This thesis describes the FED study on single crystal $[Fe(PM\text{-}AzA)_2](NCS)_2$. Our DC-RF hybrid electron source is used to track molecular motions in single crystal $[Fe(PM\text{-}AzA)_2](NCS)_2$.

The background of the SCO dynamics is discussed to present multiple studies on the SCO dynamics first. Photoinduced SCO, a molecular transition induced by photoexcitation, involves both electronic state changes in center metal atom and atomic motions of the SCO molecule

Our FED is a direct probe of molecular motions with atomic spatial resolution and ~300 fs time resolution [49,58]. Therefore, our FED study on the SCO dynamics is focused on the atomic motions during the SCO transitions. For the atomic motions during the ultrafast photoswitching of spin states, the metal-ligand bond elongation is generally believed as one key motion of SCO [19-26]. The metal-ligand bond elongation is caused by the transfer of two electrons from the nonbonding orbitals to antibonding orbitals and loss of π-backbonding which weaken the Fe-N bonds. Many works [19-26] have reported that the Fe-N bond elongation is directly correlated in time (150 fs) to the electronic state dynamics observed by changes in the SCO compounds' spectral features.

In our FED study on single crystal $[Fe(PM\text{-}AzA)_2](NCS)_2$, we notice that there is only one type of behaviour of all of the Bragg peaks studied, a decay or rise after excitation with ~ 2.3 ps time constant. It is very similar to the time constant of vibrational cooling of the excited HS state observed in both transient absorption and reflection spectroscopies.

In order to understand the molecular motions in real space behind changes in intensity of Bragg peaks, structure factor calculations of most Bragg peaks during the structure change from the LS state to HS state are introduced. Two possible pathways of atomic motion are simulated. Previous works [19-26] report there is a two step structure change, a sub 150 fs ultrafast metal-ligand bond elongation followed with a 2 ps slow ligand rotation. However, the behaviour of most Bragg peaks based on this pathway is not observed in the experiment. However, a coupled movement of the metal-ligand bond elongation and ligand rotation with unit cell expansion which is a direct motion from the LS state to the HS state is suggested. Most changes in intensity of Bragg peaks are very close to the observation from our FED experiment. In order to confirm the possible pathways, the contributions from the metal-ligand bond elongation, ligand motions, and unit cell expansion to intensity of Bragg peaks are also considered. Selected Bragg peaks which receive different contributions have similar time constant. Therefore, only coupled motions of these three motions can explain one type behaviour of all Bragg peaks.

Based the observation from our FED study, we report the metal-ligand bond elongation, compared to other motions during SCO, is not a conclusive signature of SCO, and it is coupled to other ligand motions. The structure change in SCO is significantly delayed with respect to the electronic SCO transition.

Furthermore, the metal-ligand bond elongation, ligand motion, and unit cell expansion are selected as three key motions to obtain molecular movie of the photoinduced SCO. A structural refinement algorithm based on a parameterized molecular model from previous FED studies is used to obtain a time-dependent map of the molecular motions of SCO. The temporal evolution of key motions shows the time constant of these three key motions are ~ 2.3 ps and they are coupled to each other. According to the reaction coordinate of three motions, a photo-excited HS structure is measured which is speculated by previous X-ray diffraction studies [79,80].

7.2 Future work on photoinduced SCO dynamics

Single crystal $[Fe(PM\text{-}AzA)_2](NCS)_2$ is classic Fe(II) SCO compound, and it has both thermal SCO and photoinduced SCO. In our FED study, we can obtain electron diffraction patterns of both the HS state and the LS state easily by changing the temperature of the samples. Based on the changes in intensity of Bragg peaks from the thermal SCO between the HS state and the LS state, the behaviour of photoinduced SCO on the intensity of Bragg peaks can be expected. Therefore, in the FED studies, we can easily determine whether the ultrafast changes in the intensity of Bragg peaks is due to the photoinduced SCO. However, for the SCO compounds with both thermal SCO and photoinduced SCO, we must set the excitation condition carefully, because the deposit heat from pump laser may introduce the thermal SCO. Therefore, a SCO compound with only photoinduced SCO can give supplementary information and help us to further understand photoinduced SCO.

Some SCO compounds only have photoinduced SCO, because the energy gap ΔE between the LS and the HS potential energy surfaces is too large. Among these SCO compound, we choose single crystal iron(II) tris(2,2'-bipyridine) hexafluorophosphate ($[Fe(bpy)_3](PF_6)_2$) as another Fe(II) photoinduced SCO sample system. $[Fe(bpy)_3]^{2+}$ is also a classic Fe(II) SCO system which undergoes a SCO transition by photoexcitation by near-UV and visible light [11]. The optical studies on single crystal $[Fe(bpy)_3](PF_6)_2$ show that the relaxation mechanism leading to the HS state in single crystal $[Fe(bpy)_3](PF_6)_2$ is similar to that in aqueous $[Fe(bpy)_3]^{2+}$ [18]. Therefore, similar structural changes reported by previous works [25] is expected to be observed in the FED study. One of the most important structure changes is the ~0.2 Å Fe-N bond elongation that is finished in sub-picosecond time constant.

The FED experiment was performed with excitation conditions similar to optical pump-probe transmission studies [18]. The single crystal samples are mounted on TEM grid and kept at room temperature. 60 fs FWHM laser pulses, centered at 400 nm with a fluence of 2.5 mJ/cm^2, are used as the pump. In Figure 7.1a, a static electron diffraction pattern of single crystal [Fe(bpy)$_3$](PF$_6$)$_2$ at LS state is presented. After photoexcitation, the average changes in intensity of Bragg peaks between 0 and 150 ps in Figure 7.1b show that almost all Bragg peaks have increasing changes in intensity, while the intensity of the center (0 0 0) Bragg peaks decreases.

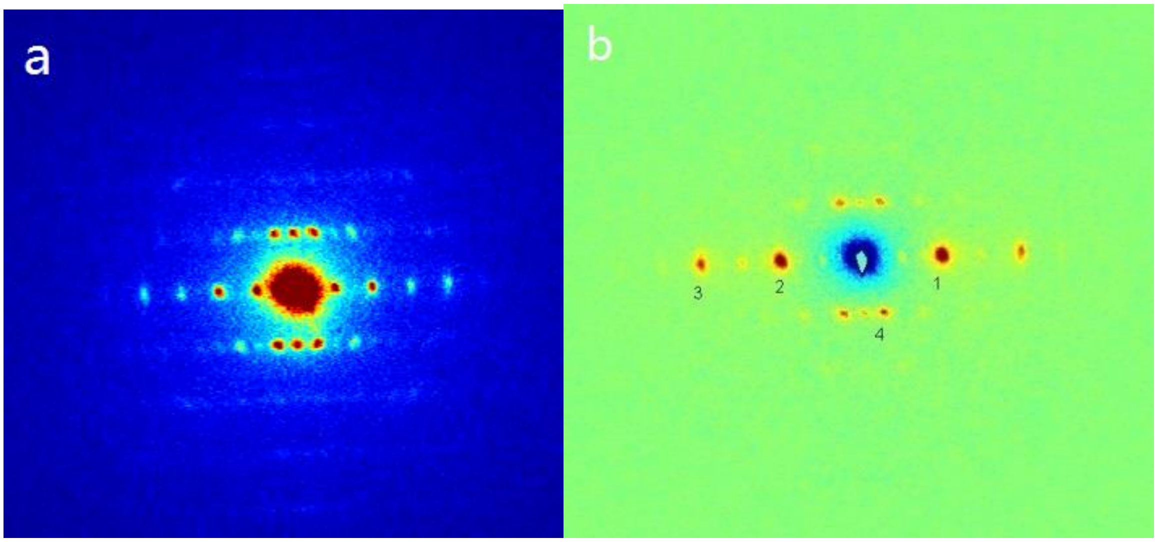

Figure 7.1: Preliminary results of FED study of single crystal [Fe(bpy)$_3$](PF$_6$)$_2$. (a) Static electron diffraction pattern of single crystal [Fe(bpy)$_3$](PF$_6$)$_2$. (b) Average changes in intensity of Bragg peaks between 0 and 150 ps.

In Figure 7.2, preliminary FED study shows there is no ultrafast (sub-picosecond) changes in intensity of selected Bragg peaks. The only change in intensity of Bragg peaks found in the FED study is an ~100 ps slow increase in diffraction intensity. This change is believed to be the acoustic phonon introduced by the pump laser, and it is similar to the oscillation observed in FED study of single crystal Fe(PM–AzA)$_2$](NCS)$_2$ (see inset of Figure 6.13).

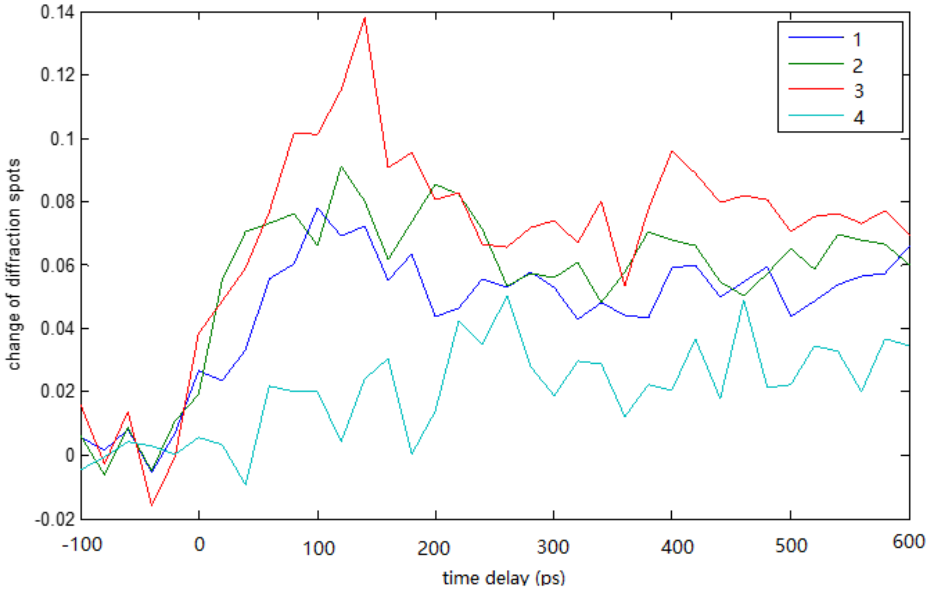

Figure 7.2: Preliminary long-time relative change in the intensity of select Bragg spots from t = -100 ps to 600 ps

One challenge of this FED study is that the structure of $[Fe(bpy)_3](PF_6)_2$ at the HS state can not be obtained by thermal SCO, so unlike the FED study of single crystal $Fe(PM–AzA)_2](NCS)_2$ the relative changes in intensity of Bragg peaks of single crystal $[Fe(bpy)_3](PF_6)_2$ cannot be simulated to compare the observations in the FED experiment. Based on the preliminary FED results, the observation of relative slower changes in intensity of Bragg peaks observed in the FED study does not support the ultrafast structural changes reported by XANES and optical pump-probe experiment on aqueous $[Fe(bpy)_3](PF_6)_2$.[15,16]. Therefore, the structural changes of single crystal $[Fe(bpy)_3](PF_6)_2$ during the SCO transitions may be different, compared to the observation in the liquid. Another possible reason is that the changes in intensity of Bragg peaks introduced by ultrafast structural changes during photoinduced SCO is too small to be noticed, based on the signal-to-noise ratio of our FED system. In Figure 7.1a, all bright Bragg peaks are low order Bragg peaks which have smaller change in intensity during the SCO, according to the FED study of single crystal $Fe(PM–AzA)_2](NCS)_2$. In the future, if diffraction intensity of high order Bragg peaks can be increased by preparing single crystal with better quality and improving the orientation of the crystal, it will be possible to observe ultrafast structural changes. Further FED experiments will focus on better signal-to-noise ratio and quality of the single crystal.

Bibliography

1. R.J.D. Miller. Femtosecond crystallography with ultrabright electrons and X-rays: Capturing chemistry in action. *Science*, 343:1108–1116 (2014).
2. A.H. Zewail. Femtochemistry: atomic-scale dynamics of the chemical bond. *The Journal of Physical Chemistry A***,** 104(24):5660–5694 (2000).
3. M. Chergui and A.H. Zewail. Electron and x-ray methods of ultrafast structural dynamics: advances and applications. *ChemPhysChem*, 10(1):28–43 (2009).
4. G. Sciaini and R.J.D. Miller. Femtosecond electron diffraction: heralding the era of atomically resolved dynamics. *Reports on Progress in Physics*, 74(9):096101 (2011).
5. A. Bousseksou, G. Molnar, L. Salmon, and W. Nicolazzi. Molecular spin crossover phenomenon: recent achievements and prospects. *Chem. Soc. Rev.*, 40, 3313–3335 (2011).
6. A. Hauser, in *Spin Crossover in Transmission Metal Compounds II* (eds Gütlich, P. & Goodwin, H. A.) 155–198 (Topics in Current Chemistry 234, Springer, 2004).
7. L. Cambi and L. Szegö. Über die magnetische susceptibilität der komplexen verbindungen. *Ber. Dtsch. Chem. Ges.*, 10:2591–2598 (1931).
8. M.A. Halcrow. The spin-states and spin-transitions of mononuclear iron(II) complexes of nitrogen-donor ligands. *Polyhedron*. 26, 3523–3576 (2007).
9. C. Brady, J. J. McGarvey, J. K. McCusker, H. Toftlund, & D. N. Hendrickson. in *Spin Crossover in Transmission Metal Compounds III* (eds Gütlich, P. & Goodwin, H. A.) 1–22(Topics in Current Chemistry 235, Springer, 2004).
10. P. Gütlich, H.A. Goodwin. Spin Crossover in Transition Metal Compounds I. Springer Berlin (2004).
11. G. Auböck and M. Chergui. Sub-50-fs photoinduced spin crossover in $[Fe(bpy)_3]^{2+}$. *Nat. Chem.*, 7:629–633 (2015).
12. G. Auböck, C. Consani, R. Monni, A. Cannizzo, F. van Mourik, and M. Chergui. Femtosecond pump/supercontinuum-probe setup with 20 khz repetition rate. *Rev. Sci. Instrum.*, 83(093105):1–5 (2012).

13. C. de Graff and C. Sousa. On the role of the metal-to-ligand charge transfer states in the light-induced spin crossover in $Fe^{II}(bpy)_3$. *Int. J. Quantum Chem.*, 111:3385– 3393 (2011).

14. C. Sousa, C. de Graaf, A. Rudavskyi, R. Broer, J. Tatchen, M. Etinski, and C. M. Marian. Ultrafast deactivation mechanism of the excited singlet in the light-induced spin crossover of $[Fe(2,2'\text{-bipyridine})_3]^{2+}$. *Chem. Eur. J.*, 19:17541–17551 (2013).

15. W. Gawelda, A. Cannizzo, V. Pham, F. van Mourik, C. Bressler, and M. Chergui. Ultrafast nonadiabatic dynamics of $[Fe^{II}(bpy)_3]^{2+}$ in solution. *J. Am. Chem. Soc.*, 129:8199–8206 (2007).

16. C. Consaini, M. Pr´ emont-Schwarz, A. ElNahhas, C. Bressler, F. van Mourik, A. Cannizzo, and M. Chergui. Vibrational coherences and relaxation in the high- spin state of aqueous $[Fe^{II}(bpy)_3]^{2+}$. *Angew. Chem.*, 121:7320–7323 (2009).

17. A. Cannizzo, C. J. Milne, W. Gawelda, C. Bressler, F. van Mourik, and M. Cher- gui. Light-induced spin crossover in Fe(II)-based complexes: The full photocy- cle unraveled by ultrafast optical and X-ray spectroscopies. *Coord. Chem. Rev.*, 254:2677–2686 (2010).

18. R. L. Field, L. C. Liu, W. Gawelda, C. Lu, and R. J. D. Miller. Spectral signatures of ultrafast spin crossover in single crystal $[Fe_{II}(bpy)_3](PF_6)_2$. *Chem. Eur. J.*, 22(15):5118–5122 (2016).

19. A. Marino, M. Servol, R. Bertoni, M. Lorenc, C. Mauriac, J. Létard, E. Collet. Femtosecond optical pump-probe reflectivity studies of spin-state photo-switching in the spincrossover molecular crystals $[Fe(PM\text{–}AzA)_2(NCS)_2]$. *Polyhedron*. 66, 123–128 (2013).

20. M. Cammarata, R. Bertoni, M. Lorenc, H. Cailleau, S. Di Matteo, C. Mauriac, S. F. Matar, H. Lemke, M. Chollet, S. Ravy, C. Laulhé, J. F. Létard, and E. Collet. Sequential activation of molecular breathing and bending during spin-crossover photoswitching revealed by femtosecond optical and X-ray absorption spectroscopy. *Phys. Rev. Lett.*, 113:227402 (2014).

21. A.Marino, M. Cammarata, S.F. Matar, J.F. Letard, G. Chastanet, M. Chollet, J.M. Glownia, H.T. Lemke and E. Collet. Activation of coherent lattice phonon following

ultrafast molecular spin-state photo-switching: A molecule-to-lattice energy transfer. *Struct. Dyn.* 3, 023605 (2016).

22. K. Haldrup, W. Gawelda, R. Abela, R. Alonso-Mori, U. Bergmann, A. Bordage, M. Cammarata, S.E. Canton, A.O. Dohn, T.B. van Driel, D.M. Fritz, A. Galler, P. Glatzel, T. Harlang, K.S. Kjaer, H.T. Lemke, K.B. Muller, Z. Nemeth, M. Papai, N. Sas, J. Uhlig, D. Zhu, G. Vanko, V. Sunstrom, M.M.Nielsen, C. Bressler. Observing Solvation Dynamics with Simultaneous Femtosecond X-ray Emission Spectroscopy and X-ray Scattering. *J. Phys. Chem. B.* 120, 1158–1168 (2016).
23. C. Consaini, M. Pr´ emont-Schwarz, A. ElNahhas, C. Bressler, F. van Mourik, A. Cannizzo, and M. Chergui. Vibrational coherences and relaxation in the high- spin state of aqueous [FeII(bpy)$_3$]$^{2+}$. *Angew. Chem*., 121:7320–7323 (2009).
24. C. Bressler, C. Milne, V. Pham, A. ElNahhas, R. M. van der Veen, W. Gawelda, S. Johnson, P. Beaud, D. Grolimund, M. Kaiser, C. N. Borca, G. Ingold, R Abela, and M. Chergui. Femtosecond XANES study of the light-induced spin crossover dynamics in an iron(II) complex. *Science*, 323:489–491 (2009).
25. W. Zhang, R. Alsono-Mori, U. Bergmann, C. Bressler, M. Chollet, A. Galler, W. Gawelda, R. G. Hadt, R. W. Hartsock, T. Kroll, K. S. Kjær, K. Kubicek, H. T. Lemke, H. W. Liang, D. A. Meyer, M. M. Nielsen, C. Purser, J. S. Robinson, E. I. Solomon, Z. Sun, D. Sokaras, T. B. van Driel, G. Vanko, T.Weng, D. Zhu, and K. J. Gaffney. Tracking excited-state charge and spin dynamics in iron coordination complexes. *Nature*, 509:345–348 (2014).
26. H. T. Lemke, C. Bressler, L. X. Chen, D. M. Fritz, K. J. Gaffney, A. Galler, W. Gawelda, K. Haldrup, R. W. Hartsock, H. Ihee, J. Kim, K. H. Kim, J. H. Lee, M. M. Nielsen, A. B. Stickrath, W. Zhang, D. Zhu, and M. Cammarata. Femtosecond X-ray absorption spectroscopy at a hard X-ray free electron laser: Application to spin crossover dynamics. *J. Phys. Chem. A.*, 117:735–740 (2013).
27. C. Sousa, C. de Graaf, A. Rudavskyi, R. Broer, J. Tatchen, M. Etinski, and C. M. Marian. Ultrafast deactivation mechanismof the excited singlet in the light-induced spin crossover of [Fe(2,2’-bipyridine)$_3$]$^{2+}$. *Chem. Eur. J.*, 19:17541–17551 (2013).
28. C. de Graff and C. Sousa. Study of the light-induced spin crossover process of [Fe^{II}(bpy)$_3$]$^{2+}$ complex. *Chem. Eur. J.* 19, 4550-4556 (2010).

29. T. H. Maiman. Stimulated optical radiation in ruby. *Nature*, 187, 493-494 (1960).
30. F. J. McClung, R.W. Hellwarth. Giant optical pulsation from ruby. *Journal of Applied Physics*., 33(3), 828-829 (1962).
31. Hans.W. Mocker, R. J. Collins. Mode competition and self locking effects in a &-switched ruby laser. *Appl.Phys.Lett.* 7(10),270-273 (1965).
32. D.E. Spence, P.N.Kean, W. Sibbett. 60-fsec pulse generation from a self-mode-locked Ti:sapphire laser. *Opt. Lett*. 16(1),42-44 (1991).
33. Strickland, D., Mourou, G. Compression of amplified chirped optical pulses. *Opt. Commun.,* 55(6),447-449 (1985).
34. H. Ahmed. Zewail. Femtochemistry: Ultrafast Dynamics of the Chemical Bond. World Scientific Publishing Co. Pte.Ltd. (1994).
35. R. J. D. Miller, R. Ernstorfer, M. Harb, M. Gao, C. T. Hebeisen, H. Jean-Ruel, C. Lu, G. Moriena, and G. Sciaini. Making the molecular movie: first frames. *Acta Crystallographica Section A* 66, 135–156 (2010).
36. X. Zou, S. Hovmoller, and P. Oleynikov, Electron Crystallograhy Electron Microscopy and Electron Diffraction. IUCr Texts on Crystallography. Oxford University Press (2011).
37. B. J. Siwick, J. R. Dwyer, R. E. Jordan, and R. J. D. Miller. Ultrafast electron optics: Propagation dynamics of femtosecond electron packets. *J. Appl. Phys.*, 92, 1643–1648 (2002).
38. A. H. Zewail, J. M. Thomas. 4D electron microscopy: imaging in space and time, Imperial College Press (2010).
39. M. Aidelsburger, F. O. Kirchner, F. Krausz, and P. Baum. Single-electron pulses for ultrafast diffraction. *Proc. Natl. Acad. Sci.* 107, 19714–19719 (2010).
40. C.-Y. Ruan, Y. Murooka, R. K. Raman, and R. A. Murdick. Dynamics of Size-Selected Gold Nanoparticles Studied by Ultrafast Electron Nanocrystallography. *Nano Letters,* 7, 1290–1296 (2007).
41. S. Nie, X. Wang, H. Park, R. Clinite, and J. Cao. Measurement of the Electronic Gruneisen Constant Using Femtosecond Electron Diffraction. *Phys. Rev. Lett*., 96, 025901 (2006).

42. P. Musumeci, J. T. Moody, R. J. England, J. B. Rosenzweig, and T. Tran. Experimental Gen- eration and Characterization of Uniformly Filled Ellipsoidal Electron-Beam Distributions. *Phys. Rev. Lett.,* 100, 244801 (2008).
43. J. B. Hastings, F. M. Rudakov, D. H. Dowell, J. F. Schmerge, J. D. Cardoza, J. M. Castro, S. M. Gierman, H. Loos, and P. M. Weber. Ultrafast time-resolved electron diffraction with megavolt electron beams. *Appl. Phys. Lett.,* 89, 184109 (2006).
44. R. Li, C. Tang, Y. Du, W. Huang, Q. Du, J. Shi, L. Yan, and X. Wang. Experimental demonstration of high quality MeV ultrafast electron diffraction. *Rev. Sci. Instrum.*, 80, 083303 (2009).
45. Y. Murooka, N. Naruse, S. Sakakihara, M. Ishimaru, J. Yang, and K. Tanimura. Transmission electron diffraction by MeV electron pulses. *Appl. Phys. Lett.,* 98, 251903 (2011).
46. B. Siwick, J. Dwyer, R. Jordan, and R. Miller. An Atomic-Level View of Melting Using Femtosecond Electron Diffraction. *Science*, 302, 1382 – 1385 (2003).
47. C. T. Hebeisen. Generation, Characterization and Applications of Femtosecond Electron Pulses. Ph.D. thesis, University of Toronto (2009).
48. T. van. Oudheusden, E. F. de. Jong, S. B. van der Geer, W. P. E. M. Op ’t. Root, O. J. Luiten, and B. J. Siwick. Electron source concept for single-shot sub-100 fs electron diffraction in the 100 keV range. *J. Appl. Phys.*, 102, 093501 (2007).
49. M. Gao, H. Jean-Ruel, R. R. Cooney, J. Stampe, M. de Jong, M. Harb, G. Sciaini, G. Moriena, and R. J. Dwayne Miller. Full characterization of RF compressed femtosecond electron pulses using ponderomotive scattering. *Opt. Express,* 20, 12048–12058 (2012).
50. M. Gao, C. Lu, H. Jean-Ruel, L. C. Liu, A. Marx, K. Onda, S.-y. Koshihara, Y. Nakano, X. Shao, T. Hiramatsu, G. Saito, H. Yamochi, R. R. Cooney, G. Moriena, G. Sciaini, and R. J. D. Miller. Mapping molecular motions leading to charge delocalization with ultrabright electrons. *Nature,* 496, 343–346 (2013).
51. H. Jean-Ruel, M. Gao, M. Kochman, C. Lu, L. C. Liu, R. Cooney, C. Morrison, and R. D. Miller. Ring-Closing Reaction in Diarylethene Captured by Femtosecond Electron Crystallography. *J. Phys. Chem. B.*, 116, 15894–15902 (2013).

52. M. Gao. Mapping organic molecular motions with RF compressed femtosecond electron diffraction. Ph.D. thesis, University of Toronto (2014).
53. H. Jean-Ruel. Femtosecond electron diffraction and spectroscopies studies of a solid state organic chemical reaction. Ph.D. thesis, University of Toronto (2014).
54. Y. Jiang. The studies on high brightness ultrafast electron generation and diffraction. master dissertation, East China Normal University (2012).
55. P. A. Anderson. Work Function of Gold. *Phys. Rev.*, 115, 553–554 (1959).
56. A. Janzen, B. Krenzer, O. Heinz, P. Zhou, D. Thien, A. Hanisch, F.-J. M. z. Heringdorf, D. v. d. Linde, and M. H. v. Hoegen. A pulsed electron gun for ultrafast electron diffraction at surfaces. *Rev. Sci. Instrum.*, 78, 013906 (2007).
57. General Particle Tracer. "http://www.pulsar.nl/gpt/" (2013).
58. M. Gao, Y. Jiang, G. H. Kassier, and R. J. D. Miller. Single shot time stamping of ultrabright radio frequency compressed electron pulses. *Appl. Phys. Lett.*, 103, 033503 (2013).
59. F. B. Kiewiet, A. H. Kemper, O. J. Luiten, G. J. H. Brussaard, and M. J. van der Wiel. Fem- tosecond synchronization of a 3 GHz RF oscillator to a mode-locked Ti: sapphire laser. *Nuc. Inst. Methods Phys. Res. A*, 484, 619–624 (2002).
60. C. T. Hebeisen, R. Ernstorfer, M. Harb, T. Dartigalongue, R. E. Jordan, and R. J. D. Miller. Femtosecond electron pulse characterization using laser ponderomotive scattering. *Opt. Lett.*, 31, 3517–3519 (2006).
61. C. T. Hebeisen, G. Sciaini, M. Harb, R. Ernstorfer, T. Dartigalongue, S. G. Kruglik, and R. J. D. Miller. Grating enhanced ponderomotive scattering for visualization and full characterization of femtosecond electron pulses. *Opt. Express*, 16, 3334 (2008).
62. M. Harb, W. Peng, G. Sciaini, C.T. Hebeisen, R. Ernstorfer, M.A. Eriksson, M.G. Lagally, S.G. Kruglik, and R.J.D. Miller. Excitation of longitudinal and transverse coherent acous- tic phonons in nanometer free-standing films of (001) Si. *Physical Review B*, 79(9):094301 (2009).
63. G. H. Kassier, K. Haupt, N. Erasmus, E. G. Rohwer, H. M. v. Bergmann, H. Schwoerer, S. M. M. Coelho, and F. D. Auret. A compact streak camera for 150 fs time resolved measurement of bright pulses in ultrafast electron diffraction. *Rev. Sci. Instrum.*, 81, 105103 (2010).

64. X. Wang, S. Nie, H. Park, J. Li, R. Clinite, R. Li, X. Wang. J. Cao. Measurement of femtosecond electron pulse length and the temporal broadening due to space charge. *Rev. Sci. Instrum.*, 90, 013902 (2009).
65. M. Gao, Y. Jiang, G. H. Kassier, and R. J. D. Miller. Single shot time stamping of ultrabright radio frequency compressed electron pulses. *Appl. Phys. Lett.*, 103, 033503 (2013).
66. L. Pao-Lo, K. J. Williams, M. Y. Frankel, and R. D. Esman. Saturation characteristics of fast photodetectors. *Microwave Theory and Techniques, IEEE Transactions*, 47, 1297–1303 (1999).
67. K. J. Williams, R. D. Esman, and M. Dagenais. Effects of High Space-Charge Fields on the Response of Microwave Photodetectors. *IEEE Photonics Technology Letters*, 6, 639–641 (1994).
68. E. N. Ivanov, S. A. Diddams, and L. Hollberg. Analysis of Noise Mechanisms Limiting the Frequency Stability of Microwave Signals Generated With a Femtosecond Laser. *IEEE Journal of Quantum Electronics*, 9, 1059–1065 (2003).
69. E. N. Ivanov, S. A. Diddams, and L. Hollberg. Study of the excess noise associated with demodulation of ultra-short infrared pulses. *Ultrasonics, Ferroelectrics and Frequency Control, IEEE Transactions*, 52, 1068–1074 (2005).
70. J. Kim, and F. X. Kartner. Attosecond-precision ultrafast photonics. *Laser and Photon Rev.*, 4, 432–456 (2010).
71. Harbour Industries. “http://www.harbourind.com/technical-information/products,” (2013).
72. H. Bethe. Ann Physik 3:133 (1929).
73. J. H. Van Vleck. Theory of electric and magnetic susceptibilities. Oxford University Press, New York (1932).
74. A. H. Ewald, R.L. Martin, A.H. White. *Proc Roy Soc A*, 280:235 (1964).
75. F. Palacio, E. Coronado, P. Delhaes, D. Gatteschi, J. S. Miller (eds.). Localized and itinerant molecular magnetism. From molecular assemblies to the devices. Kluwer Academic, NATOASI Series C 321 (1996).
76. O. Kahn. Molecular magnetism. VCH, New York Heidelberg (1993)

77. H. Dau, P. Liebisch, M. Haumann. X-ray absorption spectroscopy to analyze nuclear geometry and electronic structure of biological metal centers – potential and questions examined with special focus on the tetra-nuclear manganese complex of oxygenic photosynthesis. *Anal. Bioanal. Chem.*, 376, 562–583 (2003).
78. F. A. Lima. Investigation of Physiological Solutions of Metalloproteins in a High-Repetition Rate Picosecond X-ray Absorption Experiment. PhD thesis, Ecole Poly-technique Federale de Lausanne (2011).
79. E. Collet, N. Moisan, C. Balde, R. Bertoni, E. Trzop, C. Laulhe, M. Lorenc, M. Servol, H. Cailleau, A. Tissot, M. Boillot, T. Graber, R. Henning, P. Coppens, M.B. Cointe. *Ultrafast spin-state photoswitching in a crystal and slower consecutive processes investigated by femtosecond optical spectroscopy and picosecond X-ray diffraction.* Phys. *Chem. Chem. Phys.,*14, 6192–6199 (2012).
80. E. Collet, M. Lorenc, M. Cammarata, G. Laurent, M. Servol, A.Tissot, M.-L. Boillot, H. Cailleau, and M. B.-Le Cointe. 100 Picosecond Diffraction Catches Structural Transients of Laser-Pulse Triggered Switching in a Spin-crossover Crystal. Chem. Eur. J., 18, 2051-2055 (2012).
81. V. Briois, C. C. dit Moulin, P. Sainctavit, Ch. Brouder, and A.-M. Flank. Full Multiple Scattering and Crystal Field Multiplet Calculations Performed on the Spin Transition FeII(phen)2(NCS)2 Complex at the Iron K and L2,3 X-ray Absorption Edges. J. Am. Chem. Soc., 117, 1019-1026 (1995).
82. A. L. Smeigh, M. Creelman, R. A. Mathies, and J. K. McCusker. Femtosecond time-resolved optical and Raman spectroscopy of photoinduced spin crossover: temporal resolution of low-to-high spin optical switching. J. Am. Chem. Soc., 130, 14105-14107 (2008).
83. S. Schenkl, F. Van Mourik, N. Friedman, M. Sheves, R. Schlesinger, S. Haacke , and M. Chergui. Insights into excited-state and isomerization dynamics of bacteriorhodopsin from ultrafast transient UV absorption. Proc. Natl Acad. Sci. USA, 103, 4101-4106 (2006).
84. J. F. Létard, L. Capes, G. Chastanet, N. Moliner, L. Sylvie, R. José-Antonio, and K. Olivier. Critical temperature of the LIESST effect in iron(II) spin crossover compounds. Chem. Phys. Lett., 313, 115-120 (1999).

85. P. Guionneau, J. F. Létard, D. S. Yufit, C. Daniel, B. Georges, E. G. Andrés, A. K. H. Judith, and K. Olivier. Structural approach of the features of the spin crossover transition in iron(II) compounds. J. Mater. Chem., 9, 985-994 (1999).
86. B. K. Yoo, Z. Su, J. M. Thomas, and H. Z. Ahmed. On the dynamical nature of the active center in a single-site photocatalyst visualized by 4D ultrafast electron microscopy. PNAS, 113, 503-508 (2016).
87. P. Baum, D.-S. Yang, and A. H. Zewail. 4D Visualization of Transitional Structures in Phase Transformations by Electron Diffraction. Science, 318, 788-792 (2007).
88. L.-M. Peng, G. Ren, S. L. Dudarev, and M. J. Whelan. Robust parameterization of elastic and absorptive electron atomic scattering factors. Acta. Cryst. A, 52, 257-276, (1996).
89. M. Harb, W. Peng, G. Sciaini, C. T. Hebeisen, R. Ernstorfer, A. E. Mark, G. L. Max, G. K. Sergei, and R. J. D. Miller. Excitation of longitudinal and transverse coherent acoustic phonons in nanometer free-standing films of (001) Si. Phys. Rev. B., 79, 094301 (2009).
90. N. Huse, H. Cho, K. Hong, L. Jamula, M. F. de G. Frank, K. K. Tae, K. M. C. James, and W. S. Robert. Femtosecond soft X-ray spectroscopy of solvated transition-metal complexes: deciphering the interplay of electronic and structural dynamics. J. Phys. Chem. Lett., 2, 880-884 (2011).
91. R. Bertoni, R. Bertoni, M. Lorenc, H. Cailleau, A. Tissot, J. Laisney, B. Marie-Laure, S. Laurentiu, S. Alexandru, E. Cristian, and C. Eric. Elastically driven cooperative response of a molecular material impacted by a laser pulse. Nat. Mater., 15, 606-610 (2016).
92. B. Ordejón, B. Ordejón, C. de Graaf, and C. Sousa. Light-Induced Excited-State Spin Trapping in Tetrazole-Based Spin Crossover Systems. J. AM. Chem. Soc., 130, 13961-13968 (2008).

List of hazardous substances used during the doctoral project

No hazardous substances were used during the doctoral project.

Appendix

In this thesis, photoinduced SCO dynamics of single crystal Fe(PM-AzA)$_2$](NCS)$_2$ is studied by DC-RF hybrid femtosecond electron diffraction system (FED). The temporal characteristics of the high brightness electron pulses is characterized by a photo-triggered streak camera. The results of the FED experiment show that the structural changes of the metal and ligand and electronic state changes in the metal atom are concomitant but not simultaneous. The metal-ligand bond elongation, compared to other nuclear motions in the photoinduced SCO, is not a conclusive signature of the photoinduced SCO, and it is coupled to the other nuclear motions in phase transition. The metal-ligand bond elongation (and other nuclear motions) is significantly delayed with respect to the electronic SCO transitions.

In dieser Arbeit wird photoinduzierte SCO-Dynamik von Monokristall Fe(PM-AzA)$_2$](NCS)$_2$) durch die DC-RF-Hybrid-FED untersucht . Die zeitlichen Eigenschaften der Elektronenpulse mit hohen Helligkeit wird von einem photoinduzierten Streak-Kamera gemessen. Die Ergebnisse des FED-Experiments zeigen, dass die Strukturänderungen des Metalls und Ligands und die elektronische Zustandsänderungen in dem Metallatom sind begleitend, aber nicht gleichzeitig. Die Dehnung einer Metall-Ligand-Bindung, im Vergleich zu anderen Kernbewegungen in der photoinduzierten SCO, ist kein ausschlaggebender Faktor des photoinduziertes SCO. Sie wird mit den anderen Kernbewegungen in Phasenübergang kombiniert. Die Dehnung einer Metall-Ligand-Bindung (und andere Kernbewegungen) ist, im Vergleich zu SCO-Dynamiken, signifikant verzögert.

List of earlier publications derived from the dissertation

M. Gao, Y. Jiang, G. Kassier, R. J. D. Miller, Single shot time stamping of ultrabright radio frequency compressed electron pulses. *Applied Physics Letters* 103 (3) (2013).

Y. Jiang, L.C. Liu, H.M. Müller-Werkmeister, M. Gao, C. Lu, D. Zhang, E. Collet, R.J.D. Miller. Femtosecond Electron Diffraction Study of the Spin Crossover Dynamics of Single Crystal $[Fe(PM\text{-}AzA)_2](NCS)_2$. 19th International Conference on Ultrafast Phenomena, Okinawa Convention Center, Okinawa, Japan, July 07, 2014 - July 11, 2014. *Springer Proceedings in Physics* 162, pp. 283-286 (2015).

R.L. Field, L.C. Liu, C. Lu, Y. Jiang, W. Gawelda, R.J.D Miller. Ultrafast Dynamics Related to Spin Crossover Processes in Single Crystal $[Fe^{II}(bpy)_3](PF_6)_2$. 19th International Conference on Ultrafast Phenomena, Okinawa Convention Center, Okinawa, Japan, July 07, 2014 - July 11, 2014. *Springer Proceedings in Physics* 162, pp. 279-282 (2015).

Eidesstattliche Versicherung

Declaration on oath

Hiermit erkläre ich an Eides statt, dass ich die vorliegende Dissertationsschrift selbst verfasst und keine anderen als die angegebenen Quellen und Hilfsmittel benutzt habe.

I hereby declare, on oath, that I have written the present dissertation by my own and have not used other than the acknowledged resources and aids.

Hamburg, den city and date Unterschrift signature